# Model Predictive Control for Future Interconnected and Green Vehicles

**Hao Sun**

Principal Supervisor: Dr. Boli Chen
Subsidiary Supervisor: Prof. Sarah Spurgeon

A dissertation submitted in partial fulfillment
of the requirements for the degree of
**Doctor of Philosophy**
of
Department of Electronic and Electrical Engineering
**University College London**

January 11, 2025

I, Hao Sun, confirm that the work presented in this thesis is my own. Where information has been derived from other sources, I confirm that this has been indicated in the work.

# Nomenclature

## Abbreviation

ACC Adaptive Cruise Control

ARIMA Auto Regressive Integrated Moving Average Model

AT-DMPC Adaptive Tube-based Distributed Model Predictive Control

BPNN Back Propagation Neural Network

CACC Cooperative Adaptive Cruise Control

CAV Connected and Autonomous Vehicle

CNN Convolutional Neural Network

DMPC Distributed Model Predictive Control

EV Electric Vehicle

GCN Graph Convolutional Network

HDV Human Driven Vehicle

HIL Hardware-in-the-Loop

IDM Intelligent Driver Model

ISMC Integral Sliding Mode Control

ISS Input-to-State Stability

LEC Learning-based Ecological Car-following strategy

LSTM Long Short-Term Memory

MAH Multi-Head Attention Mechanism

MFST Macro-micro Fused Spatial-temporal Transformer

MPC Model Predictive Control

OCP Optimization Control Problem

PF Predecessor-Follower

PLF Predecessor-Leader Following

PMSM Permanent Magnet Synchronous Motor

RBF-NN Radial Basis Function Neural Network

SMC Sliding Mode Control

STT Spatial-Temporal Transformer

TPLF Two Predecessor-Leader Following

# Notation

$C_d$, $C_f$ Air drag and rolling resistance coefficients

$d$, $w$ Modeling uncertainty and measurement noise

$E$, $\Delta t$ Kinetic energy and time headway of vehicle

$g$ Gravity constant

$m$ Vehicle mass

$P$ Vehicle power

$p$, $v$ Position and velocity of vehicle

| | |
|---|---|
| $r$ | Tire radius |
| $T$, $\xi$ | Input torque and virtual input |
| $x$, $u$, $y$ | Actual state, input and output |
| $x^a$, $u^a$ | Assumed state and input |
| $\hat{x}$, $\hat{y}$ | Estimated state and output |
| $\bar{x}$, $\bar{u}$ | Nominal state and input |
| $x^*$, $u^*$ | Optimal state and input |
| $\Delta T$ | Discrete input torque change rate |
| $\Delta s$ | Sampling distance interval |
| $\eta_m$ | Motor efficiency |
| $\eta_t$ | Transmission efficiency of the powertrain |
| $\theta$ | Road slope angle |
| $\mathscr{E}$, $\delta$ | Normalized kinetic energy and time headway of vehicle |
| $\mathscr{T}$, $\zeta$ | Normalized input torque and virtual input |
| $\omega$ | Motor angular velocity |
| $\mathbb{R}$, $\mathbb{R}_{\geq 0}$ | The real and the non-negative real sets of numbers |
| $\mid a \mid$ | The absolute value of the number $a \in \mathbb{R}$ |
| $\mid\mid x \mid\mid_2$ | The Euclidian norm of the vector $x \in \mathbb{R}^n$ |
| $\mid\mid x \mid\mid_\infty$ | The infinity norm of the vector $x \in \mathbb{R}^n$ |
| $A_{[i,j]}$ | The $(i, j)$th entry of the matrix $A \in \mathbb{R}^{n \times n}$ |
| $\max(x)$ | The maximum entry of the vector $x \in \mathbb{R}^n$ |

$\min(x)$ The minimum entry of the vector $x \in \mathbb{R}^n$

$\oplus$ The Minkowski sum of sets $\mathbb{W} \oplus \mathbb{V} = \{x + y \mid x \in \mathbb{W}, y \in \mathbb{V}\}$

$\ominus$ The Minkowski difference of sets $\mathbb{W} \ominus \mathbb{V} = \{x \mid x \oplus \mathbb{V} \subseteq \mathbb{W}\}$

# Abstract

Urbanization and the steady increase in vehicle numbers are pushing transportation to its limits, resulting in congestion, higher emissions and energy consumption, and safety issues. These have promoted legislation and technologies for cleaner, safer and more efficient transport. Connected and autonomous vehicle (CAV) technology is set to play a major role in the ongoing transport revolution. This thesis focuses on the control design for various CAV control problems with a particular emphasis on model predictive control (MPC). MPC is notable for its ability to effectively handle strict constraints on controls and states, such as powertrain limits, collision avoidance constraints and traffic regulation constraints while achieving near-optimal performance according to an objective function specified by the designer.

The first part of this thesis focuses on developing a robust car-following strategy for a single CAV, which achieves the best trade-off between performance optimality and computational efficiency through a novel MPC design. Next, the problem is extended to a platooning problem which involves multiple CAVs in the one-dimensional space. A distributed robust MPC algorithm is designed for platoon formation control. The final part of the thesis focuses on the coordination of multiple vehicles within a two-dimensional space. A hierarchical planning and control framework is developed to solve this, where the motion planner is based on the artificial potential field method, and the control layer employs distributed MPC. Numerical results of all proposed methods are given with comprehensive comparisons with state-of-the-art methods.

# Impact Statement

In recent years, the number of global vehicles has been growing rapidly, which expands at a rate around 10% per annum according to the data reported by authoritative organizations [1,2]. This increase has significant implications for road safety, as well as growing energy consumption and contributing to higher emissions. To address the aforementioned problems, the 'Electric' and 'Autonomous' developing trend proposed by automotive industry leaders such as Waymo, Tesla, Argo AI, Cruise, Baidu, Uber, and others [3–6] represents a reasonable and forward-thinking solution.

With the continuous advancements in technologies such as data collection and fusion, localization and navigation, decision-making and control, and environmental perception, electric connected and autonomous vehicles are anticipated to become available to humans in the near future [7–9]. To accelerate the implementation of autonomous driving, this thesis focuses on the properties required for practical applications, such as real-time computation capability, robustness against uncertainties, controller optimality and feasibility, and so on. Moreover, the hardware-in-the-loop and the vehicle on-road experiments are designed and conducted to validate the practical applicability.

# Acknowledgements

This thesis is the result of research work conducted at the Department of Electronic and Electrical Engineering, University College London (UCL). Undertaking the Doctor of Philosophy (Ph.D.) has been a memorable experience and it would not have been possible without the support of many people.

First and foremost, I would like to express my gratitude to my supervisors, Dr. Boli Chen and Prof. Sarah Spurgeon, for providing me with this opportunity to pursue academic dreams, and particularly a remote working condition during the Covid pandemic period to avoid study interruption. This allowed me the maximum freedom to pursue my research interests and will continue to benefit me for the rest of my life. Without your persistent guidance and care, this thesis would not have been completed.

I would like to thank my co-authors, including Dr. Bingbing Li, Dr. Hao Zhang, Dr. Giuseppe Fedele, Dr. Weichao Zhuang, Dr. Junyan Hu, Dr. Shuang Li, Prof. Li Dai and Prof. Guodong Yin, for their valuable and insightful contributions in the publications we worked together. In particular, I would like to give my special thanks to Dr. Bingbing Li and Dr. Hao Zhang, who gave me unstinting support during my most challenging times.

Moreover, I am also thankful to my friends and colleagues, including but not limited to: Dr. Hao Xu, Mr. Mingyang Chen, Dr. Zhongze Bai, Dr. Ruitian He, Mr. Sheng Yu, Mr. Shaowei Yuan, Miss. Boyi Tang, Mr. Zhuo Zhi, Dr. Kaitao Meng, Mr. Kaipeng Xu, Mr. Yuxuan Sun, Mr. Keyue Jiang, Dr. Vittorio Casagrande, Dr. Francesca Boem, Dr. Maria Novitasari and Dr. Martin Ferianc.

Finally, I owe my deepest gratitude towards my parents, who always love me

unconditionally. I am profoundly grateful for their encouragement, support and belief in me to pursue my Ph.D. at UCL.

# Contents

# List of Figures

# List of Tables

# Chapter 1

# Introduction

## 1.1 Background

With the accelerated pace of urban development in recent years, the number of on-road vehicles has been continuously increasing, reaching approximately 1.446 billion in 2024 [2]. This trend results in severe congestion, energy consumption, and road hazards. To tackle these issues, the concept of 'Connected and Autonomous Vehicle' (CAV) has been proposed and promoted by research organizations and automobile industries, which has the potential to alleviate the underlying problems.

The development about CAV related technologies can be dated back to the Program on Advanced Technology for the Highway [11] at the University of California, Berkeley in the 1990s. With the continuous advancement of technologies [12, 13], various strategies for CAV have been explored, which include optimal control [14–17], learning-based method [18–21], model predictive control (MPC) [22–24] and heuristic algorithm [25, 26]. Different algorithms brings distinct advantages, and in particular, MPC-based schemes turn out to be one of the most preferable control solutions [27] for their capability of handling the control and state constraints, which are ubiquitous in the autonomous driving, such as powertrain limits, collision avoidance constraints and traffic regulation constraints.

In the context of environmental pollution, powertrain electrification is widely recognized as a beneficial solution, as it reduces emissions resulting from fuel combustion. Based on the UK government roadmap [28], electric vehicles are con-

sidered as one of the final goals in transport electrification and decarbonisation by 2050. From a report of Goldman Sachs in 2022 [29], the proportion of the electrified vehicles of the whole global automobile market will rise from 3% in 2020 to 15% in 2025 and then 32% and 58% in 2030 and 2040, respectively.

## 1.2 Challenges and Contributions

According to the literature in CAV control (a detailed review is given in Chapter 2), to solve a series of issues resulting from urbanization and the rising number of vehicles (as illustrated in Fig. 1.1), MPC-based strategies for CAVs are designed and proposed in this study. To be specified, three different scenarios are considered, including ecological car-following, heterogeneous CAV platooning and multi-CAV coordination in two-dimensional scenario.

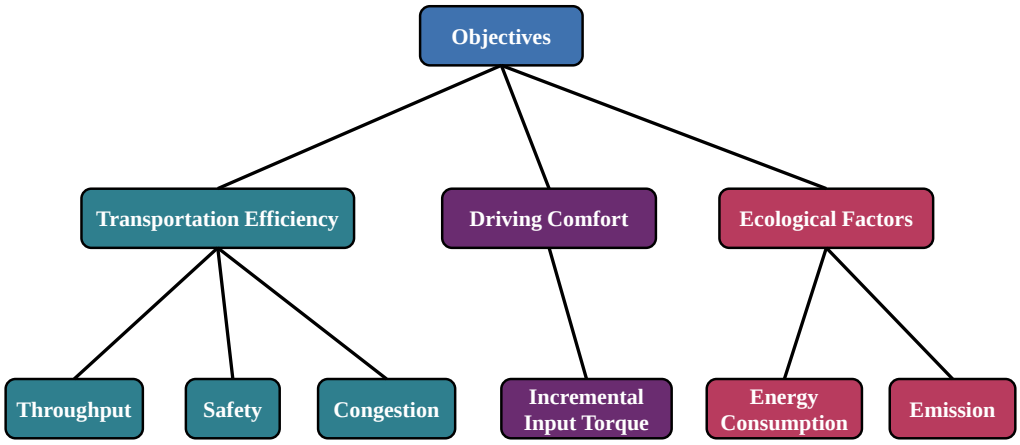


Figure 1.1: Objectives achieved in this thesis.

### 1.2.1 Research Challenges

In recent decades, the development and deployment of CAV technologies have been accompanied by many challenges. Some current approaches are not based on optimization, relying instead on methods such as PID [30, 31], sliding mode control [32,33] and heuristic algorithms [34,35]. However, most optimal control-based methods require nonlinear optimization [36,37], which demands substantial computational resources and is therefore impractical for real-time applications. In complex

transportation scenarios, certain unrealistic assumptions are made, such as using the IDM [38, 39] to simulate the car-following behavior of HDVs. Furthermore, many studies only focus on road safety [40,41] while neglecting vehicle energy consumption. This oversight is critical as people are facing the problem of increasing energy consumption due to the rising vehicle number [42, 43]. Additionally, some works remain purely theoretical and do not incorporate the design of corresponding HIL or vehicle on-road experiments for validation.

### 1.2.2 Aims and Contributions

In order to address the aforementioned research challenges, the aims of the proposed thesis are introduced in this subsection. Firstly, a novel distributed MPC algorithm is developed, ensuring theoretical guarantees such as recursive feasibility and Lyapunov stability. To ensure the practical capability of the CAV controller, the original nonlinear problem has been reformulated into a lossless convex form based on fairly accurate vehicle and powertrain models. Additionally, a learning-in-the-loop speed forecasting approach is employed, which accounts for the impact of traffic conditions on CAV control. Considering road safety, an improved APF planning strategy is developed and integrated with an MPC controller that incorporates safety constraints, enabling collision avoidance in unknown environments. Finally, the hardware-in-the-loop experiment and the on-road vehicle experiment are designed in order to verify the practical applicability of the proposed methods in different scenarios.

## 1.3 Thesis Outline

The remainder of this paper is structured as follows. In Chapter 2, the fundamental concepts about MPC and the related works concerning the MPC-based CAV control are introduced to facilitate a comprehensive understanding. Chapter 3 proposes a spatial-temporal transformer-based car-following strategy. Through a spatial domain modeling approach, the original nonlinear problem is reformulated into a lossless convex form, enabling real-time computation of the developed controller. The validity of this reformation is guaranteed by a parameter tuning guide. Mean-

while, the error between the predicted trajectory and the actual trajectory is handled by the robust MPC in the control layer. In Chapter 4, the single car-following problem is extended to a CAV platooning problems where considering heterogeneity. Theoretical analysis of recursive feasibility and Lyapunov asymptotic stability are demonstrated. Moreover, hardware-in-the-loop experiment results are presented. A planning-and-tracking framework is developed in Chapter 5 in order to achieve collision avoidance and reconfiguration for CAVs in unknown environments. The upper layer motion planning is based on an improved artificial potential field method, which can ensure the boundedness of the resulting speed profile. In the control layer, obstacle avoidance is guaranteed by incorporating safety constraints into the MPC controller. Additionally, the strategy is highlighted for its advantages in comparison with another state-of-the-art algorithm. Finally, Chapter 6 concludes this study and further discusses the future works.

## 1.4 Publication List

During the period of pursuing the degree of Doctor of Philosophy, the publications of the author are listed as follows:

**Journal Papers:**

1. **Sun, H.**, Li, B., Zhang, H., Dai, L., Fedele, G., Zhuang, W. and Chen, B., 2024. Ecological Electric Vehicle Platooning: An Adaptive Tube-based Distributed Model Predictive Control Approach. *IEEE Transactions on Transportation Electrification.* **(Accept)**

2. **Sun, H.**, Dai, L., Fedele, G. and Chen, B., 2024. A Convex and Robust Distributed Model Predictive Control for Heterogeneous Vehicle Platoons. *European Journal of Control.* **(Accept)**

3. Li, B., Zhuang, W., Zhang, H., **Sun, H.**, Liu, H., Zhang, J., Yin, G. and Chen, B., 2023. Traffic-aware Ecological Cruising Control for Connected Electric Vehicle. *IEEE Transactions on Transportation Electrification.* **(Accept)**

4. **Sun, H.**, Li, S., Li, B., Chen, M., Zhang, S., Zhuang, W., Yin, G. and Chen,

B., 2024. Spatial-Temporal Transformer-based Ecological Car-Following Strategy for Connected Electric Vehicles in Dynamic Environment. *Energy.* **(Under Review)**

**Conference Papers:**

1. **Sun, H.**, Hu, J., Dai, L. and Chen, B., 2024. A Multi-Agent Path Planning Strategy with Reconfigurable Topology in Unknown Environments. In *2024 IEEE 20th International Conference on Automation Science and Engineering (CASE)*. IEEE. **(Accept)**

2. **Sun, H.**, Dai, L. and Chen, B., 2022. Tube-based distributed model predictive control for heterogeneous vehicle platoons via convex optimization. In *2022 IEEE 25th International Conference on Intelligent Transportation Systems (ITSC)*. IEEE. **(Accept)**

# Chapter 2

# Fundamental Concepts and Related Works

## 2.1 Motivations of MPC

The concept of Model Predictive Control (MPC) derives from optimal control theory, which employs the mathematical model of a system to forecast its future behavior. Based on these predictions, MPC optimizes control decisions to achieve predefined objectives. MPC-based strategies are widely regarded as one of the most preferable solutions for CAV control due to their ability to effectively manage both control and state constraints inherent in vehicle control, such as powertrain input, collision avoidance and traffic regulation limits.

## 2.2 Basics of MPC

The vehicle dynamic system can be modeled in the form of nonlinear difference equations as follows:

$$x(k+1) = f(x(k), u(k)) \tag{2.1}$$

where $k$ is the discrete time index. $x(k) \in \mathbb{R}^n$, $u(k) \in \mathbb{R}^m$ and $f : \mathbb{R}^n \times \mathbb{R}^m \to \mathbb{R}^n$ denotes the state, the input and the transition relationship. Constraints of the afore-

mentioned system (2.1) are defined as

$$\mathbb{X} = \{x(k) \in \mathbb{R}^n : \underline{x} \leq x(k) \leq \bar{x}\} \tag{2.2a}$$

$$\mathbb{U} = \{u(k) \in \mathbb{R}^m : \underline{u} \leq u(k) \leq \bar{u}\} \tag{2.2b}$$

where $\mathbb{X} \subset \mathbb{R}^n$ is the admissible state set and $\mathbb{U} \subset \mathbb{R}^m$ is the admissible input set, which are both compact and time-invariant. In the context of CAV control, the state $x(k)$ could partially involve the two-dimensional position vectors $p_x(k)$ and $p_y(k)$, the velocity $v(k)$ and the speed angle $\beta(k)$ depending on different scenarios. For instance, the state vector can be defined as $x(k) = [p(k), v(k)]^\top$ when considering longitudinal platoon control problem.

For such systems, the control law that exhibits the best closed-loop properties is the solution to the following finite horizon constrained optimal control problem (MPC).

**OCP 1**

$$\min_{u(k)} \; J_{N_p}(x(k), u(k)) = \sum_{j=0}^{N_p-1} l(x(j|k), u(j|k)) + V_f(x(N_p|k)) \tag{2.3a}$$

***s.t.*** *for* $j = 0, 1, 2, \ldots, N_p - 1$

$$x(j+1|k) = f(x(j|k), u(j|k)) \tag{2.3b}$$

$$x(j|k) \in \mathbb{X} \tag{2.3c}$$

$$u(j|k) \in \mathbb{U} \tag{2.3d}$$

$$x(N_p|k) \in \mathbb{X}_f \tag{2.3e}$$

$$x(0|k) = x(k) \tag{2.3f}$$

where (2.3a) is the objective function, where $l(x(j|k), u(j|k))$ denotes the stage cost and $V_f(x(N_p|k))$ denotes the terminal cost. $x(:|k)$ and $u(:|k)$ are the optimization state and input, respectively. Let $(x_{des}, u_{des})$ represent the optimal equilibrium, satisfying $f(x_{des}, u_{des}) = x_{des}$, and choose the terminal set $\mathbb{X}_f$ such that $x_{des} \in \mathbb{X}_f \subset \mathbb{X}$. Moreover, $l(x_{des}, u_{des}) = 0$ and $V_f(x) \geq 0$ are commonly assumed.

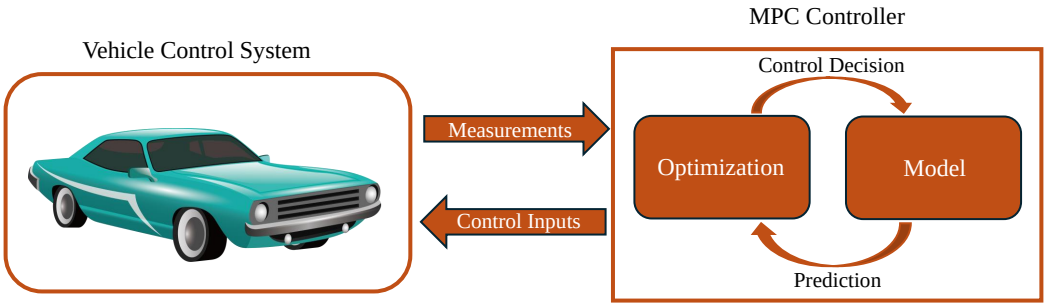


Figure 2.1: MPC application in vehicle control system.

Figure 2.1 presents the MPC application corresponding to vehicle control system. At step $k$, optimal solutions $u^*(k) = \{u^*(0|k), u^*(1|k), ..., u^*(N_p - 1|k)\}$ are obtained through solving the finite receding horizon problem 2.3, and only the initial input $u^*(0|k)$ is applied to the dynamic system (2.1). After taking the updated measurements, the MPC algorithm is operated repeatedly at step $k+1$. The described process can be illustrated in Figure 2.2

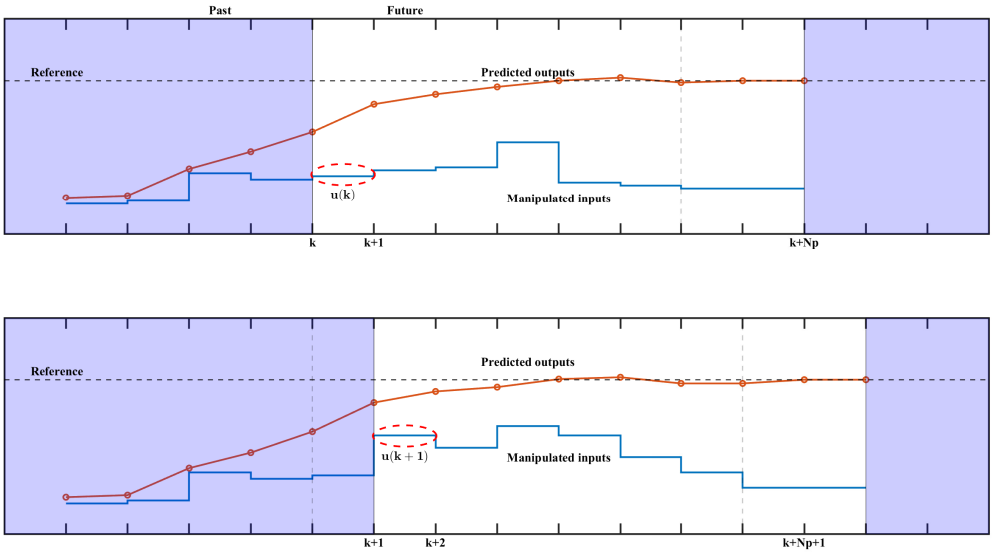


Figure 2.2: MPC application in vehicle control system.

Moreover, the application of MPC is not limited to a specific system. MPC can be implemented in any control system that permits real-time computation, typically depending on the horizon length and the complexity of the proposed problem.

The MPC setup can be adapted to a wide range of scenarios, such as the objective function, the dynamic model, the predictive horizon length, and the terminal constraint employed. The MPC-based optimization problems are normally formulated as quadratic or linear forms in order to find solutions within an interval step. In addition, for hybrid or nonlinear models, the MPC problems can be reformulated as a mixed-integer quadratic program, or as a nonlinear program.

## 2.3 Closed-loop Properties of MPC

Due to the finite predictive horizon, the recursive feasibility and stability of the MPC-based system can be guaranteed. In the following, we will discuss how terminal conditions can be employed to ensure the stability and optimality of a nominal MPC through set-valued analysis. For the purpose of further analysis, the following definitions are introduced.

**Definition 2.3.1** *(Feasible control input). The control input u is considered feasible if the resulting state x satisfies constraints* (2.3b) *to* (2.3f)*.*

$$\mathscr{U}_{N_p}(x) = \{u \mid (2.3b) - (2.3f)\ hold\} \tag{2.4}$$

**Definition 2.3.2** *($N_p$-step controllability set). The $N_p$-step controllability set $\mathbb{X}_{N_p}$ fulfills:*

$$\mathbb{X}_{N_p} = \{x \mid \mathscr{U}_{N_p}(x) \neq \emptyset\} \tag{2.5}$$

The recursive feasibility, a key porperty of MPC, is defined based on Definitions 2.3.1 and 2.3.2.

**Definition 2.3.3** *(Recursive feasibility). Give any $x(k) \in \mathbb{X}_{N_p}$, we have $x(k+1) = f(x(k), u(k))$ remains in $\mathbb{X}_{N_p}$.*

The recursive feasibility property ensures that $x(k)$ exists for every initial state $x(0|k) \in \mathbb{X}_{N_p}$, and that $x(k)$ remains within $\mathbb{X}_{N_p}$. To ensure the closed-loop stability of the MPC algorithm (2.3), we rely on the following assumption, which was established as a standard for stabilizing MPC by [44].

**Assumption 2.3.1** *A terminal control law $\kappa_f(\cdot)$: $\mathbb{X}_f \to \mathbb{U}$ exists, such that for $x \in \mathbb{X}_f$:*

*a). $\mathbb{X}_f$ is positive invariant under the terminal control law $\kappa_f(\cdot)$: $x(k+1) = f(x(k),u(k)) \in \mathbb{X}_f, \forall x(k) \in \mathbb{X}_f$.*

*b). $V_f(\cdot)$ is a local Lyapunov function with respect to the terminal state $x(N_p|k)$, which satisfies $J_{N_p}(x(k+1),u(k+1)) \leq J_{N_p}(x(k),u(k))$.*

Now, all the necessary ingredients are introduced to characterize the MPC stability as follows:

**Theorem 2.3.1** *(Asymptotic stability and positive invariance [44]). First, under Assumption 2.3.1, there exist $\mathscr{K}_\infty$ class functions $\alpha_1$, $\alpha_2$ such that $l(x(k),u(k)) \geq \alpha_1(|x(k)|)$ and $V_f(x(k)) \leq \alpha_2(|x(k)|)$ with the optimal value function $J^*_{N_p}(x(k),u(k))$. Then, the $N_p$-step controllability set $\mathbb{X}_{N_p}$ is strong positively invariant for the MPC problem* (2.3)*. Moreover, the dynamic system introduced in* (2.3b) *is asymptotic stable with the region of $\mathbb{X}_f$ centered at the desired state.*

Furthermore, we can see that increasing the predictive horizon $N_p$ will enlarge the range of invariant set $\mathbb{X}_f$ based on Definitions 2.3.1 and 2.3.2.

## 2.4 MPC with Linear System and Quadratic Cost Function

Linear dynamic models with quadratic cost function are one of the most important formulations in MPC. A finite predictive horizon MPC problem can be formulated by replacing (2.3a) and (2.3b) with a linear discrete-time prediction model

$$x(j+1|k) = Ax(j|k) + Bu(j|k) \tag{2.6}$$

and the quadratic cost function

$$l(x(j|k),u(j|k)) = x(j|k)^\top Qx(j|k) + u(j|k)^\top Ru(j|k), \tag{2.7}$$

$$V_f(x(N_p|k)) = x(N_p|k)^\top Px(N_p|k) \tag{2.8}$$

on the basis of the general MPC problem (2.3). The matrices $Q$, $R$ and $P$ are symmetric, where $Q \geq 0$ and $P \geq 0$ are $n \times n$ symmetric real matrices and $R > 0$ is an $m \times m$ symmetric real matrix. Without considering the state and the input constraints (2.3c) and (2.3d), the problem is similar to the linear quadratic regulator (LQR) but is solved over a finite horizon $N_p$ instead of an infinite horizon. Once the constraints (2.3c) and (2.3d) are taken into consideration, the unique optimal feedback control law determined by the discrete-time Algebraic Riccati equation in the context of the LQR framework no longer holds. In most on-road vehicle control cases, the speed and input torque are constrained by both traffic regulations and physical limits of the powertrain. These constraints impose upper and lower bounds. Ensuring compliance with these constraints is importance, as failure to do so could lead to severe results.

In the view of the quadratic cost function (2.6), the $j$th state in the $k$-step predictive horizon can be denoted as $x(j|k) = A^j x(k) + \sum_{n=0}^{j-1} A^n B u(j-1-n|k)$, and the MPC problem can be formulated as a QP [45] with the initial state $x(0|k) = x(k)$. Provided matrices $A$ and $B$ for the linear dynamic model (2.6) are stabilizable, and then cost function $J(x(k), u(k))$ is convex and the optimal control $u^*(k)$ is piecewise linear, with both being continuous within $\mathbb{X}_{N_p}$. As such, there is always a unique solution $u^*(k)$ to such a QP.

**Theorem 2.4.1** *(Existence of the optimal solution [45]). Based on a linear dynamic model* (2.6) *and quadratic costs* (2.7) *and* (2.8)*, $J^*_{N_p}$ is a convex, piecewise linear-quadratic function, and $u^*(k)$ is also piecewise linear. Both $J^*_{N_p}$ and $u^*(k)$ are continuous within $\mathbb{X}_{N_p}$.*

## 2.5 Robust MPC for Time-varying Additive Disturbances

A general case based on linear dynamic models with a time-varying disturbance is expressed as follows:

$$x(k+1) = Ax(k) + Bu(k) + w(k) \tag{2.9}$$

where $x(k) \in \mathbb{R}^n$ and $u(k) \in \mathbb{R}^m$ are the state and input as same in the previous subsection. $w(k) \in \mathbb{R}^n$ denotes an unknown time-varying additive disturbance. In order to design effective robust MPC algorithms, it is necessary to assume the disturbance $w(k)$ belongs to a bounded set $\mathbb{W}$.

**Definition 2.5.1** *(Robust invariant set). If for any $x(k) \in \mathbb{X}$, it holds that $x(k+1) = f(x(k), Kx(k)) + w(k) \in \mathbb{X}$ for all $w(k) \in \mathbb{W}$, where $K$ denotes a state feedback gain. In other words, $\mathbb{X}$ remains positively invariant under any disturbance $w(k) \in \mathbb{W}$.*

In this subsection, we explore a robust MPC approach based on [46], which involves optimizing feedback policies $u(j|k) = K(x(j|k) - \bar{x}(j|k)) + c(j|k)$, where $c(j|k)$ is a constant and $K$ is a fixed matrix chosen during controller design that defines stabilizing state feedback control. This feedback ensures that the actual state $x(k+j)$ remains close to the nominal prediction $\bar{x}(j|k)$ despite unknown disturbances. While literature offers methods for linear systems that optimize more complicated feedback policies [47], tube MPC is conceptually straightforward, enables online optimization comparable to linear MPC in complexity, and can be readily extended to address complexities such as parameter uncertainty and nonlinear dynamics.

Substituting the feedback policy into the dynamic model (2.9)

$$x(j+1|k) = Ax(j|k) + B(K(x(j|k) - \bar{x}(j|k)) + c(j|k)) + w(j|k). \tag{2.10}$$

Define the uncertain part $e(j|k)$ between predicted state $x(j|k)$ and the nominal state $\bar{x}(j|k)$ as $e(j|k) = x(j|k) - \bar{x}(j|k)$, then

$$\bar{x}(j+1|k) + e(j+1|k) = A\bar{x}(j|k) + Bc(j|k) + Ae(j|k) + BKe(j|k) + w(j|k). \tag{2.11}$$

Next, we decompose (2.11) into the 'known' part and 'unknown' part below

$$\bar{x}(j+1|k) = A\bar{x}(j|k) + Bc(j|k) \tag{2.12}$$

$$e(j+1|k) = Ae(j|k) + BKe(j|k) + w(j|k) \tag{2.13}$$

The nominal state $\bar{x}(j|k)$ evolves according to the undisturbed nominal system with the constant $c(j|k)$, and the unknown $e(j|k)$ evolves based on the design of the feedback control gain $K$. Considering a robust invariant set $\mathbb{S}$, if $e(0|k) \in \mathbb{S}$, then $e(j|k)$ will also belong to $\mathbb{S}$, which implies the actual state $x(j|k)$ will remain close to the nominal prediction $\bar{x}(j|k)$. Given that $e(j|k) \in \mathbb{S}$, the state and input constraints $x(j|k) \in \mathbb{X}$ and $u(j|k) \in \mathbb{U}$ will be satisfied if $\bar{x}(j|k) + e(j|k) \in \mathbb{X}$ and $c(j|k) + Ke(j|k) \in \mathbb{U}$ for all $e(j|k) \in \mathbb{S}$ or equivalently

$$\bar{x}(j|k) \in \mathbb{X} \ominus \mathbb{S}, \; c(j|k) \in \mathbb{U} \ominus K\mathbb{S} \tag{2.14}$$

where $\oplus$ and $\ominus$ represent the Minkowski sum and difference of sets respectively. The proposed robust MPC optimization problem can be resulted in:

**OCP 2**

$$\min_{c(k)} \; J_{N_p}(\bar{x}(k), c(k)) = \sum_{j=0}^{N_p-1} l(\bar{x}(j|k), c(j|k)) + V_f(\bar{x}(N_p|k)) \tag{2.15a}$$

***s.t.*** *for* $j = 0, 1, 2, \ldots, N_p - 1$

$$\bar{x}(j+1|k) = A\bar{x}(j|k) + Bc(j|k) \tag{2.15b}$$

$$\bar{x}(0|k) \in x(k) \oplus \mathbb{S} \tag{2.15c}$$

$$\bar{x}(j|k) \in \mathbb{X} \ominus \mathbb{S} \tag{2.15d}$$

$$c(j|k) \in \mathbb{U} \ominus K\mathbb{S} \tag{2.15e}$$

$$\bar{x}(N_p|k) \in \mathbb{X}_f \ominus \mathbb{S} \tag{2.15f}$$

where $\bar{x}(:|k)$ and $c(:|k)$ are the nominal state and the control sequence, respectively. It is noteworthy that the initial condition for the nominal predicted state $\bar{x}(0|k)$ must satisfy the constraint (2.15c) in order to avoid the infeasibility at the initial step. This robust MPC formulation satisfies similar recursive feasibility and closed-loop stability properties as the linear case. For a rigorous analysis, including more robust results on exponential stability, readers are referred to [46]. Next, we will provide a brief outline of the proofs for these properties.

If the OCP 2 (2.15) is feasible at step $k$, we can formulate a sub-optimal solution for the $k+1$ step, where $\hat{x}(:|k+1) = \{\bar{x}(1|k), \bar{x}(2|k), ..., \bar{x}(N_p|k), \kappa_f(\bar{x}(N_p|k)\}$ with $\kappa_f(x) = (A+BK)x$ and $\hat{c}(:|k+1) = \{c(1|k), c(2|k), ..., c(N_p-1|k), K\bar{x}(N_p|k)\}$ can also satisfy constraints (2.15b) to (2.15f). By induction method, we can infer that if it is feasible at the step $k=0$, it is also feasible for all $k$, and the resulting state and input constraints will be satisfied in closed-loop.

**Theorem 2.5.1** *(Recursive feasibility of robust MPC). For the dynamic system* (2.9) *with uncertainty $w(s)$ controlled by $u(k) = u^*(0|k)$, the OCP 2* (2.15) *can guarantee feasibility for all iteration $k = 0, 1, ..., \infty$ if it is feasible at the initial step $k = 0$, and $x(k) \in \mathbb{X}$, $u(k) \in \mathbb{U}$ in closed-loop operation.*

Based on the objective function $J_{N_p}(\bar{x}(k), c(k))$ in (2.15a), if $V_f(x)$ satisfies $l(x,u) + V_f(f(x, \kappa_f(x))) \geq V_f(x)$ then if $\bar{x}(0|k) \neq 0$ and $l(x,u)$ is positive definite, we will have

$$\begin{aligned} J_{N_p}(\bar{x}(k), c(k)) &= \sum_{j=0}^{N_p-1} l(\bar{x}(j|k), c(j|k)) + V_f(\bar{x}(N_p|k)) \\ &> \sum_{j=1}^{N_p-1} l(\bar{x}(j|k), c(j|k)) + V_f(\bar{x}(N_p|k)) \\ &\geq \sum_{j=1}^{N_p} l(\bar{x}(j|k), c(j|k)) + V_f(\bar{x}(N_p|k+1)) \\ &\geq J_{N_p}(\bar{x}(k+1), c(k+1)) \end{aligned} \tag{2.16}$$

where the first inequality holds because $l(\bar{x}(0|k), c(0|k))$ is positive, and the second inequality holds because $l(x,u) + V_f(f(x, \kappa_f(x))) \geq V_f(x)$. The third inequality is valid because the optimal solution of (2.15) will always have a lower cost than the constructed solution, which are feasible but probably sub-optimal for the same problem.

As demonstrated, if $J_{N_p}(\bar{x}(k+1), c(k+1)) \leq J_{N_p}(\bar{x}(k), c(k))$, and if this objective function is positive definite in $\bar{x}(0|k)$, then it serves as a Lyapunov function for $\bar{x}(0|k)$, ensuring asymptotic convergence to zero in closed-loop. Thus, $x(k)$ converges within the closed-loop to the set $\mathbb{S}$.

**Theorem 2.5.2** *(Asymptotic stability of the robust MPC). According to the robust MPC algorithm described in* (2.15)*, the uncertain dynamic system* (2.9) *demonstrates robust stability and asymptotically converges to the set* $\mathbb{S}$ *in closed-loop.*

## 2.6 MPC-based CAV Control

According to some literature [48–50], the study of CAV control is commonly classified into three categories: single CAV car-following scenario, multiple CAVs platooning scenario, and two-dimensional CAV coordination scenario. The primary objective in the car-following scenario is to develop a control system for the ego CAV to achieve a balance between road safety, energy consumption, and driver comfort. Building upon this, prediction and observer algorithms are typically employed to estimate the states of preceding vehicles, and robust control methods are required to address the uncertainties inherent in the ego CAV system. Moreover, real-time computation capacity is also important for practical applicability of CAVs. Regarding multiple CAVs platooning scenario, further aspects need to be considered upon the car-following problem, e.g. the heterogeneity from different types of vehicles and the influence brought from vehicle-to-vehicle (V2V) communication. 'Heterogeneity' pertains to variations in vehicle parameters, differences in powertrain deployment, and the presence of human-driven vehicles within the CAV platoon. Additionally, 'topology' and 'delay' are primary focuses in studies of platooning V2V communication. In the context of the two-dimensional multi-CAV coordination, more problems need to be taken into account. Due to a more complex scenario, such as unknown obstacles, the strategy of following the preceding vehicle may no longer be applicable. Therefore, a safety-guaranteed motion planner becomes imperative for CAVs in dynamic environments.

## 2.7 Single CAV Car-following Scenario

***CAV powertrain types*** The automotive industry has undergone significant transformations over the past century, marked by several key milestones in propulsion technology [51–53]. Initially, internal combustion engines (ICE) dominated the market, providing reliable performance through the combustion of fossil fu-

els [54–56]. These engines, although efficient for their time, were characterized by high emissions and a dependence on non-renewable energy sources [57–59].

The next evolutionary step was the introduction of hybrid vehicles, which combined the traditional internal combustion engine with an electric motor [60–62]. This innovation aimed to enhance fuel efficiency and reduce emissions by utilizing electric power during low-speed and idle conditions [63–66]. Hybrid vehicles, such as the Toyota Prius [67, 68], demonstrated the potential for greener driving without sacrificing performance, bridging the gap between ICE vehicles and fully electric cars.

As environmental concerns and technological advancements progressed, electric vehicles (EVs) gained prominence [69, 70]. These vehicles rely solely on electric power, eliminating tailpipe emissions and reducing the overall carbon footprint. Pioneered by companies like Tesla [71, 72], EVs have become increasingly popular due to their high efficiency, lower operating costs, and advancements in battery technology, which have significantly extended driving ranges. The latest innovation in this evolutionary journey is the in-wheel motor electric vehicle [73–75]. Unlike traditional EVs that utilize a central motor, in-wheel motor vehicles incorporate electric motors directly within the wheels. This design offers numerous advantages, including improved efficiency, better handling, and increased interior space. By placing the motors in the wheels, these vehicles can achieve more precise control of each wheel independently, enhancing traction and stability [76–78].

In conclusion, the evolution from internal combustion engines to hybrid and fully electric vehicles, and now to in-wheel motor electric vehicles, reflects the industry's ongoing commitment to improving efficiency, reducing environmental impact, and enhancing driving experiences. Each step in this journey represents a significant leap towards a more sustainable and technologically advanced automotive future.

***Preceding vehicle state prediction*** Vehicle state prediction has been extensively studied over a long period. Various statistical models have been applied for practical applications, such as Auto Regressive Integrated Moving Aver-

age (ARIMA) [79, 80] and Markov Chain models [81, 82]. However, these models are unable to account for the non-linear and long temporal dependencies of traffic conditions. Neural networks have exhibited better performance in prediction for vehicle energy management than Markov Chain [83]. Therefore, various networks, such as Radial basis function neural networks (RBF-NN) [83–85], Back propagation neural networks (BPNN) [86, 87], have been applied to improve the accuracy of vehicle speed prediction. The deep learning technologies further enhanced the vehicle speed prediction performance [88]. To capture the time dependence while avoiding the gradient explosion problem, the Long Short-term Memory (LSTM) network has been widely used to predict the speed of electric vehicles [89, 90]. Convolutional Neural Network (CNN) has also been combined with bidirectional LSTM to capture local temporal features to improve the accuracy of vehicle speed prediction [91]. As Transformer shows outstanding ability for long temporal sequence, [92] proposes an Informer-based speed predictor for the preceding vehicle while planning the speed of connected vehicles. Although previous studies have proposed various efficient predictors, their models only focused on the self-temporal sequence, neglecting the importance of spatial features. As vehicle speed is significantly affected by the surrounding environment, the macro traffic flow of the road networks is vital for speed prediction [93]. This type of information not only offers a more comprehensive understanding of traffic conditions but also captures the spatial correlations between each road segment. Such correlations are invaluable for enhancing prediction accuracy but seldom be considered in speed predictor design.

***Ego CAV robust control*** In any autonomous system, various system errors, such as modeling uncertainties and measurement noise, are unavoidable. To handle these errors, $\mathscr{H}$-infinity control [94, 95] and sliding mode control [96, 97] are the most widely adopted robust control methods. Meanwhile, with the capability to directly incorporate hard constraints, many studies have increasingly focused on employing robust MPC strategies. [98] introduces a learning-based MPC, integrating the Gaussian process model to handle the state estimation errors. Recently, an ecological and robust control strategy [99] has been proposed for plug-in hybrid

electric vehicles. This strategy incorporates a deep learning module with advanced feature fusion technologies to enhance speed prediction. Additionally, a tube-based value function is integrated into the robust MPC-based control layer, aiming to further alleviate system uncertainties.

## 2.8 Heterogeneous CAVs Platooning Problem

***V2V communication topology*** The inter-vehicle communication graph plays an important role in the Distributed Model Predictive Control (DMPC) design. A common assumption invoked to ensure the internal stability properties of a DMPC is the existence of a spanning tree within the platoon communication graph. Under such an assumption, a typical class of DMPC algorithm is proposed in [10], which discusses the conditions ensuring asymptotic stability of vehicle platooning with respect to several common communication topologies, such as predecessor-following (PF) [100–103], predecessor-leader following (PLF) [104, 105] and K-predecessor-leader following [106–109], either directed or undirected. An alternative DMPC algorithm is introduced in [110], where a bidirectional PF communication mechanism is utilized to enhance the feasibility as compared to unidirectional PF during the initial phase when the target of the leader is not known to all followers. On the other hand, delay represent another communication issue as data transmission inevitably introduces time delays under practical conditions due to insufficient bandwidths, over-length platoons, radio interference, etc. In this regard, a robust DMPC approach using min-max optimization is designed in [111], which is proven to be robust against communication delays.

***Practical capability for CAV platooning*** Due to the advancement in sensing and communication technologies and global positioning system (GPS), DMPC solutions are receiving considerable research interest. They permit each controller to be deployed locally on each vehicle so that the computational efficiency and overall system resilience can be significantly improved as compared to centralized approaches [10, 112–115]. However, existing CAVs still face challenges in handling nonlinear programming due to the limited onboard computa-

tional resources, especially when energy consumption model is considered. Some early works [116, 117] only consider highly simplified second-order linear models, which reduce the computational complexity. Nevertheless, due to the use of the over-simplified vehicle model, the control solution may not be sufficiently accurate. Recent research in [118] introduces a feedback linearization method. This approach compensates for system nonlinearities to align with the characteristics of the original system and is applicable for linear DMPC. Nevertheless, the feedback linearization scheme is not robust due to the presence of modeling uncertainties. Current studies about this topic remain limited and warrant further exploration. Therefore, there is a keen interest in developing robust and real-time implementable algorithms for platooning.

***Complex tasks*** Existing platooning studies are not only limited to longitudinal formation control, numerous algorithms are developed to address more practical scenarios. Some researchers focus on lateral motion in overtaking [119–122] and curving [123–126] problems. A decision-making and control framework for platoon overtaking maneuvers is proposed in [119]. Using a centralized decision-making strategy based on game theory, the optimal overtaking timing for the platoon can be determined. In the control layer, a distributed lateral motion controller is designed for each CAV to avoid collisions. In [120], a hybrid platoon controller is developed using a three-dimensional coupled model based on sliding mode control. The finite-step convergence of the proposed controller is also guaranteed with Lyapunov stability theory. [123] proposes a robust platoon control on curved roads with consideration of road slopes, external disturbances and communication delays. The platoon inner stability and string stability can be guaranteed by a Lyapunov-Krasovskii functional $\mathscr{H}_\infty$ controller.

There are some platoon related works that also consider vehicle-to-infrastructure (V2I), such as signal light [127–129] and cloud platform with edge devices [18, 130, 131]. With the purpose of passing the intersection without stopping, [128] proposes an energy-saving predictive cruise control method based on neural networking. The employed energy-consumption are trained considering the

signal phasing and timing (SPaT) data. In [129], a signal-vehicle coupled optimal control approach is developed, where the human driven vehicles (HDVs) in mixed platoon are taken into account. Through this scheme, the energy consumption and traffic throughput improve progressively with the increase in the number of CAVs. [130] proposes a mobile edge platoon cloud framework to calculate available communication bandwidth allocation for CAVs in a platoon, with consideration of a Stackelberg game theory. Moreover, the consortium blockchain technology is introduced to ensure the data transaction security.

## 2.9 Two-dimensional CAV Coordination

***Motion planning*** Motion/path planning (also known as navigation problem) represents one of the most typical multi-agent system problems, and it appears in a variety of modern engineering applications including connected and autonomous vehicles [132–137]. In addition to the traditional methods such as probabilistic roadmap [135], A* [136], and Dijkstra [137], which are mainly used for single agent path planning in a globally known environment. Numerous algorithms [134, 138–144] have been recently proposed for CAVs including the artificial potential field (APF) [134, 138–140], model predictive control [141, 142], and reinforcement learning [143, 144]. It is noteworthy that due to the limited onboard computation power, communication and sensing range, and potential transmission delay [145], most of the available research focuses on distributed or decentralized coordination schemes, whereas centralized methods are used only in case there exists an agent or a central coordinator features sufficient communication and computation resources [146–148].

***Collision avoidance in unknown environment*** Multi-agent collision avoidance is a research hotspot in CAV control area. Some of them are based on leader-follower [149–151] approach or swarm intelligence [152, 153]. For example, in [150], a nonlinear consensus control algorithm is developed which can guarantee the longitudinal string stability of platooning. Additionally, an artificial function-based lateral motion algorithm is also designed. In [153], an adaptive robust for-

mation control method is developed for CAV swarm in the two-dimensional environment, where the collision avoidance can be ensured through a diffeomorphism transformation approach. However, these algorithms are limited to the only leading CAV. In the presence of unknown distributed obstacles, the flexibility of the platoons or swarms may be sacrificed by yielding more conservative paths.

Recently, some researchers try to solve CAV coordination in dynamic environments with unknown obstacles through the planning-and-control framework [134, 154–156]. [155] presents a coordination scheme for CAVs under the satisfaction of collision avoidance constraints. Each swarm has a unique leader capable of identifying unknown obstacles and establishing a safe tube centered around the state trajectory. The recursive feasibility and stability of the proposed scheme are guaranteed. In [154], an integrated controller combining APF and DMPC is introduced for synchronous path planning and motion control. Additionally, to adapt to complex transportation scenarios, a cooperative switching strategy for CAVs is proposed, incorporating merge-and-split maneuvers. However, trajectories generated in real-time based on learning and APF often fail to satisfy the dynamic model characteristics of CAVs. A multi-agent coordination control law subject to motion constraints is designed in [157, 158], which defends the practical usefulness of motion planning algorithms based on single-integrator models.

# Chapter 3

# Ecological Car-following Strategy for A Single CAV

## 3.1 Introduction

A Learning-based Ecological Car-following strategy (LEC) for electric CAVs is presented in this chapter. The speed of the preceding vehicle is predicted through a Macro-micro Fused Spatial-temporal Transformer (MFST), while any discrepancies between the actual and predicted states can be addressed in the control layer. Specific contributions are summarized as follows:

- A spatial-temporal transformer model is proposed in this study. The micro and macro traffic information are fused by tailored modules for preceding vehicle speed prediction, and we obtained the best prediction performance compared to the baseline methods.

- Following the last point, the proposed LEC strategy can handle the discrepancies between the predicted state and the actual state of the preceding vehicle. Compared to the conventional robust approach [159], our method can yield less conservative solutions while maintaining robust/safe behavior. Additionally, the dynamic system is reformulated in the spatial domain to achieve real-time computation. Moreover, the validity of the reformation is investigated to provide parameter tuning guides.

- Through comparison with state-of-the-art algorithms, the advantages of the LEC strategy are highlighted in terms of computational efficiency and energy savings. Furthermore, an on-road vehicle experiment is conducted at Southeast University, China, to validate the practical applicability of the proposed method.

The rest of this chapter is organized as follows. Section 3.2 describes the car-following strategy and specifies the system models. In Section 3.3, the methodology of the proposed LEC strategy is introduced. Numerical simulation results are presented in Section 3.4 and the on-road vehicle experiment is demonstrated in Section 3.5. Finally, the conclusion and the future work are given in Section 3.6.

## 3.2 Problem Statement

This paper considers an ecological car-following strategy for electric vehicles, incorporating speed profile forecasting and tracking. The velocity of the preceding vehicle can be forecasted using the MFST, and a robust learning-in-the-loop MPC algorithm within the control layer can achieve car-following behavior and address the discrepancies between the predicted state and the actual state. Furthermore, the proposed strategy is capable of real-time computation based on a spatial domain modeling approach. For more details, the vehicle dynamic model and the power consumption model of the in-wheel motor are introduced, along with reformulation into convex form in the spatial domain, which is presented as follows:

### 3.2.1 In-wheel Electric Motor Model

The CAV is driven by two PD18 in-wheel motors, whose power consumption models can be characterized as follows:

$$P(t) = \begin{cases} \frac{T(t)\omega(t)}{\eta_m\left(T(t),\omega(t)\right)}, & T(t) \geq 0 \\ T(t)\omega(t)\eta_m\left(T(t),\omega(t)\right), & T(t) < 0 \end{cases} \tag{3.1a}$$

$$T(t) = \frac{F(t)r}{\eta_t}, \tag{3.1b}$$

$$\omega(t) = \frac{v(t)\eta_t}{r} \tag{3.1c}$$

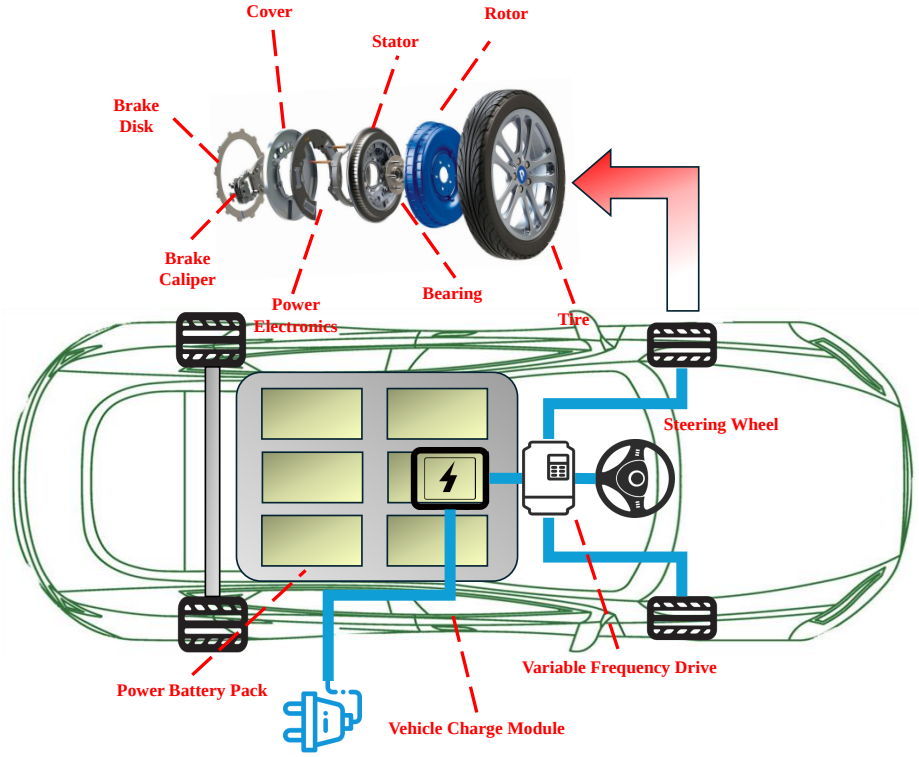


Figure 3.1: The configuration of the CAV being driven by two PD18.

where $\eta_m\big(T(t),\omega(t)\big)$ represents the motor efficiency which depends on the angular velocity $\omega(t)$ and the input torque $T(t)$. $F(t)$ is the propulsive force supplied by the motor, $\eta_t$ denotes the transmission efficiency and $r$ is the radius of the wheel. Moreover, $T(t) \geq 0$ and $T(t) < 0$ represent the traction and braking processes, respectively. Based on the experimental data of PD18 provided by Protean Electric Inc, the efficiency map of the employed motor is established as a look-up table as shown in Fig. 3.2.

In order to improve computational efficiency and enable real-time computation of the proposed algorithm, we replace the method of obtaining power $P(t)$ through table lookup with a fitted model for the in-wheel motor. We approximate $P(t)$ in Fig. 3.2 by a regression technique, and a quadratic fitted model of $T(t)$ and $v(t)$

depicted in Fig. 3.2 can be written as follows:

$$P(t) = aT^2(t)v(t) + bT(t)v(t) + cv(t) \tag{3.2}$$

where $a$, $b$, $c$ are fitting parameters obtained through the nonlinear least squares method. As a result, the coefficient of determination $R^2$ exceeds 0.99. Upon transformation from the time domain to the spatial domain, the resultant expression becomes:

$$\int P(t)dt = \int \frac{P(s)}{v(s)}ds = \int \Big(aT^2(s) + bT(s) + c\Big)ds \tag{3.3}$$

which follows a quadratic form.

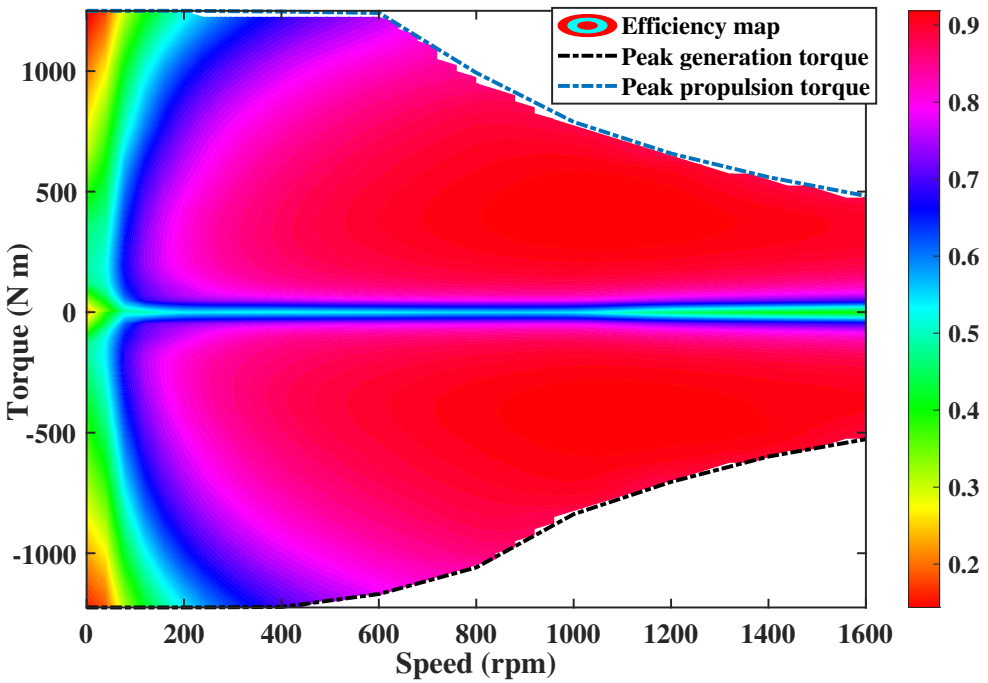


Figure 3.2: Power fitting map of the in-wheel motor.

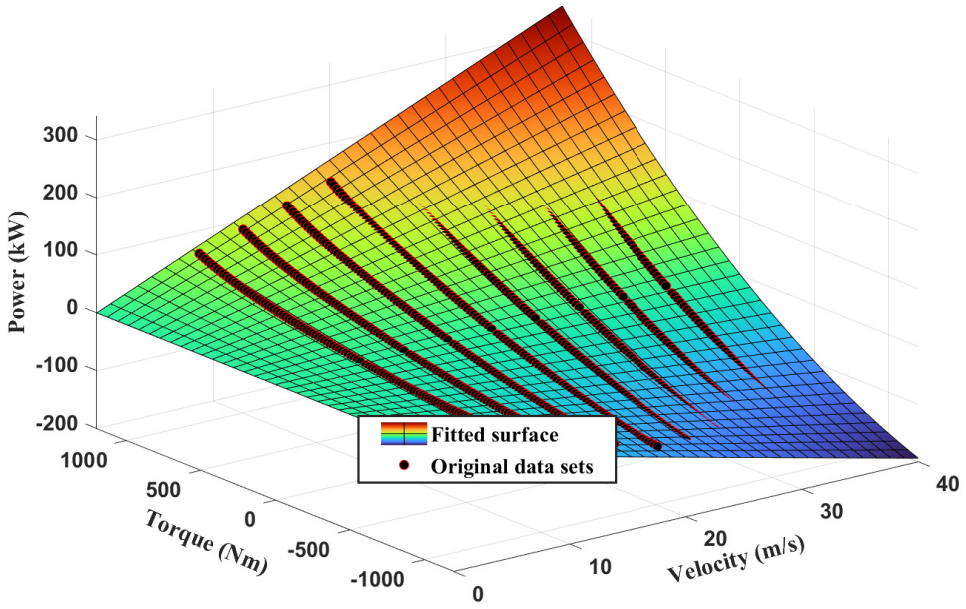


Figure 3.3: Power fitting map of the in-wheel motor.

### 3.2.2 Dynamic Modeling in Spatial Domain

First, we briefly review the time-domain dynamic models as follows:

$$\dot{p}(t) = v(t), \tag{3.4a}$$

$$\dot{v}(t) = \frac{1}{m}\left(2\frac{\eta_t}{r}T(t) - C_d v^2(t) - mg\sin\theta(t) - mgC_f\cos\theta(t)\right) \tag{3.4b}$$

where $p$, $v$ and $T$ denote the position, velocity, and torque of the CAV, respectively. $m$ is the vehicle mass and $g$ is the gravity constant. $\frac{\eta_t}{r}T$ represents the driving/braking force on tires where $\eta_t$ is the transmission efficiency of the powertrain and $r$ is the tire radius. $C_d v^2$ is the air-drag force and $C_d$ is the aerodynamic drag coefficient. $\theta$ is the road slope, leading to gradient force $mg\sin\theta(t)$. $C_f$ is the rolling resistance coefficient, and $mgC_f\cos\theta_i$ represents the tire friction.

Next, to incorporate accurate space-dependent coefficients (such as rolling resistance, road slopes, etc.), time-domain models (3.4) are reformulated into a convex

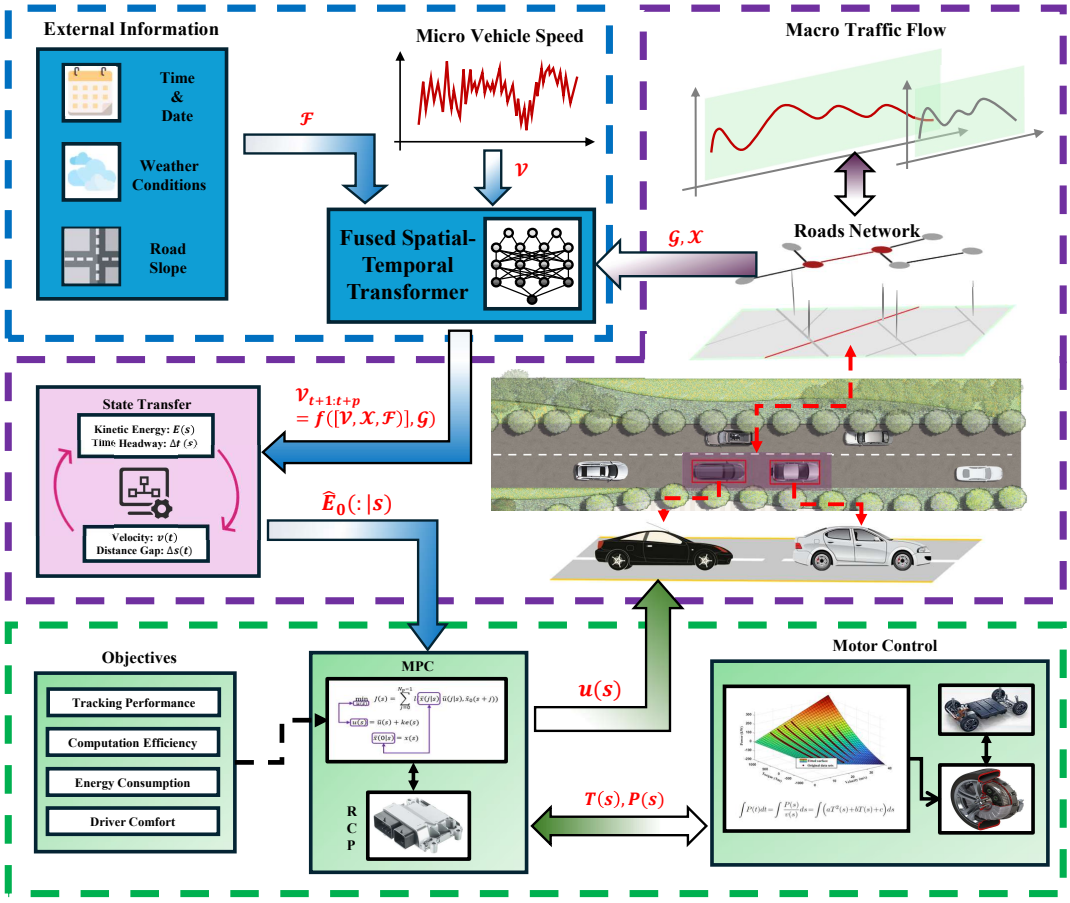


Figure 3.4: Schematic framework of the proposed LEC approach.

structure in the spatial domain via

$$\frac{d}{ds} = \frac{1}{v}\frac{d}{dt} \tag{3.5}$$

Herein, the independent variable is transformed from time $t$ to traveled distance $s$,

$$\frac{d}{ds}\Delta t(s) = \frac{1}{\sqrt{2E(s)/m}} - \frac{1}{\sqrt{2E_0(s)/m_0}}, \tag{3.6a}$$

$$\frac{d}{ds}E(s) = 2\frac{\eta_t}{r}T(s) - 2\frac{C_d}{m}E(s) - mg\sin\theta(s) - mgC_f\cos\theta(s) \tag{3.6b}$$

where $\Delta t = t(s) - t_0(s)$ and $E(s) = \frac{1}{2}mv^2(s)$ denote the time headway and kinetic energy, respectively. $t_0$ and $E_0$ are the corresponding states of the preceding vehicle. Furthermore, it is noted that $E(s) > 0, \forall s$ to avoid the singularity.

In order to improve the computation efficiency, vehicle dynamic models (3.6)

are reformulated into a convex form:

$$\frac{d}{ds}\Delta t(s) = \xi(s) - \frac{1}{v_0(s)}, \tag{3.7a}$$

$$\frac{d}{ds}E(s) = 2\frac{\eta_t}{r}T(s) - 2\frac{C_d}{m}E(s) - mg\sin\theta(s) - mgC_f\cos\theta(s), \tag{3.7b}$$

$$\xi(s) \geq \frac{1}{\sqrt{2E(s)/m}} \tag{3.7c}$$

where $v_0$ is the velocity of the preceding vehicle, and $\xi(s)$ is a fictitious control input that is designed for system convexification.

## 3.3 Learning-based Ecological Car-following Control Framework

In this section, we introduce the car-following strategy framework illustrated in Fig. 3.4. Multi-source traffic-related data, including micro vehicle speed, external information, and macro traffic flow, are collected and preprocessed to train the proposed MFST, which is mainly composed of an ensemble of diverse Transformer variants. At each sampling interval, the forecasted speed profile of the preceding vehicle can be derived based on the measured state and the well-trained MFST. This resultant profile $\hat{E}_0(:|s)$ is then integrated into a robust learning-in-the-loop MPC, which handles the discrepancies between the actual state and the predicted state. The proposed strategy is capable of offering real-time solutions while considering a trade-off among tracking performance, energy consumption, computation efficiency and driver comfort. Further details can be found in the subsequent subsections.

### 3.3.1 Macro-micro Fused Spatial-temporal Transformer

The micro speed of CAV is significantly affected by the macro traffic flow, which exhibits complex temporal and spatial dependencies. To improve the accuracy of traffic speed prediction, the speed of the preceding vehicle and three other types of data are included, namely the topological structure of the road network, macro traffic conditions, and time-related weather factors. To ensure clarity, we can divide long roads, such as expressways, into equal sections. This allows for consid-

eration of traffic conditions at each location. The connections between each section are then treated as nodes. Let $\mathscr{G} = (\mathscr{S}, \mathscr{E}, \mathscr{A})$ denotes the graph, where $\mathscr{S} \in \mathbb{R}^N$ is the set of nodes, and $N$ is the number of nodes; $\mathscr{E}$ is the edge set; $\mathscr{A} \in \mathbb{R}^{N \times N}$ is the adjacent matrix of the road network. The macro traffic conditions are denoted as $\mathscr{X} \in \mathbb{R}^{L \times N \times D}$, where L is the length of historical time steps and D is the number of traffic attribute features, such as average speed, volume, and density. It should be noted that even though the adjacent matrix is symmetric, the traffic conditions have direction, therefore, we use the entry $a_{i,j}$ in $\mathscr{A}$ to denote the direction from node $i$ to node $j$. The external factors, such as road slope, date, weather, etc., are defined as $\mathscr{F} \in \mathbb{R}^{L \times M}$, where $M$ is the number of external factors.

The main goal is to find a function $f(\cdot)$ that predicts the preceding vehicle speed $\mathscr{V}_{t+1:t+p} = [v_{t+1}, v_{t+2}, \ldots, v_{t+p}]$ since $t$-th time step based on historical $h$ time steps, where $p$ denotes the future time steps. Thus, the speed forecasting task can be formulated as follows:

$$\mathscr{V}_{t+1:t+p} = f([\mathscr{V}, \mathscr{X}, \mathscr{F}]_{t-h+1:t}, \mathscr{G}) \tag{3.8}$$

In this study, a spatial-temporal deep learning model MFST is developed to predict the speed of the preceding vehicle based on micro and macro traffic data. The micro-data includes the historical speed of the preceding vehicle and external factors, and the macro-data includes traffic flow conditions and road network graph data. We consider the external factors as micro-data because they include the road number (i.e. the edge number in the graph) on which the preceding vehicle was traveling. To address the long-range temporal correlations, a Transformer is introduced, as it has demonstrated superior performance in predicting sequential data. Additionally, recognizing the significance of node information and topological structure, we employ Graph Convolutional Networks (GCN) to capture spatial relationships [160]. As illustrated in Figure 3.5, the proposed MFST comprises four modules: the Input module, Temporal Transformer (TT), Spatial Transformer (ST), and Spatial-Temporal Transformer (STT).

(1) The function of the input module is to receive and pre-process data. The

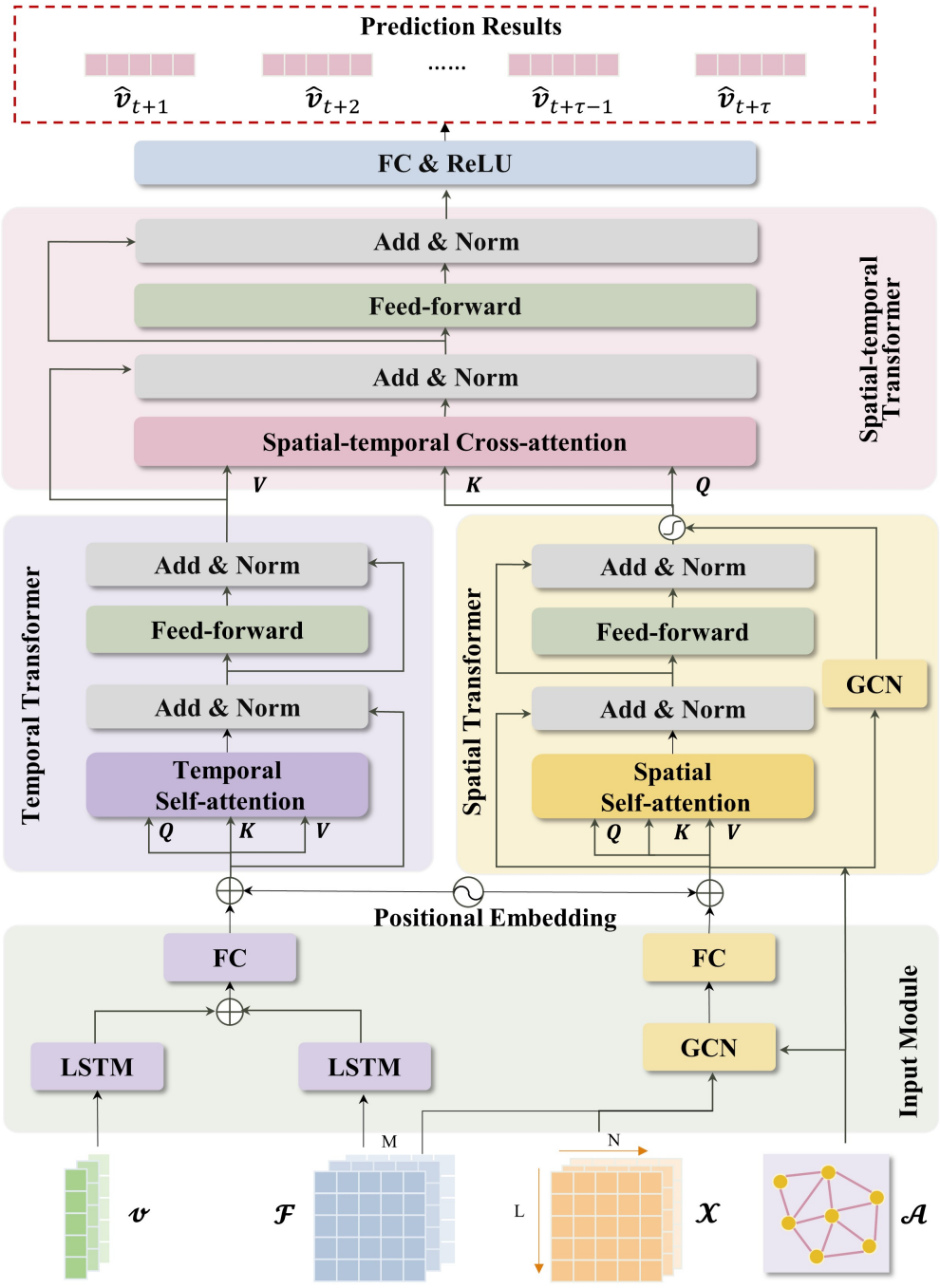


Figure 3.5: Framework for prediction model.

historical preceding vehicle speed and external factors are fed into a Long Short-term Memory (LSTM) model, which is then embedded by a fully connected layer. The external factors include the number of road segments where the preceding vehicle was traveling. Simultaneously, the macro traffic conditions are input into a GCN layer along with the adjacency matrix, followed by a fully connected layer.

Through this module, the temporal and spatial features are preliminary embedded, which can be formulated as follows:

$$\mathbf{H}^{temp} = Linear(Concat(LSTM(\mathscr{F}), LSTM(v))) \tag{3.9}$$

$$\mathbf{H}^{spat} = Linear(GCN(\mathscr{X}, \mathscr{A})) \tag{3.10}$$

where $\mathbf{H}^{temp}$ and $\mathbf{H}^{spat}$ are pre-processed temporal and spatial hidden states, respectively.

(2) TT and ST are designed to capture temporal and spatial correlations, respectively. Before being input into the transformer modules, the temporal and spatial hidden states are processed by Positional Encoding to capture the sequence information. Then, both modules apply a multi-head attention mechanism (MAH), feed-forward layer (FF), and Add & Norm layer.

The attention mechanism consists of multiple parallel scaled dot-product attention heads. For each head, a linear layer is applied to produce a 3-tuple of keys $\mathbf{K}$, queries $\mathbf{Q}$, and values $\mathbf{V}$ for inputs. Then the attention scores can be calculated as (3.11a). In the transformer, Multi-Head Attention (MHA) enables the model to capture different aspects of the input sequence simultaneously, enhancing its ability to learn complex patterns and dependencies.

$$Atten = softmax(\frac{\mathbf{Q}\mathbf{K}^{\top}}{\sqrt{d_{\mathbf{K}}}})\mathbf{V} \tag{3.11a}$$

$$MHA(Q,K,V) = Concat(Atten_1, \ldots, Atten_i)W^O \tag{3.11b}$$

Where $d_{\mathbf{K}}$ is the dimension of the key, $Atten_i$ is the *i-th* attention mechanism in MHA, and $W^O$ is the learnable parameter for the output layer.

The FF layer consists of two fully connected linear layers with a ReLU activation in between. Add & Norm (AN) layer functions as the connection, which applies Layer normalization and residual connections. Therefore, the procedure can

be formulated as follows:

$$FFN(\mathbf{H}_i) = ReLU(Linear(\mathbf{H}_i)W^F + bi^F \tag{3.12a}$$

$$AN(\mathbf{H}_i) = LayerNorm(\mathbf{H}_i + Sublayer(\mathbf{H}_i)) \tag{3.12b}$$

Where $\mathbf{H}_i$ is the output of a certain hidden layer, weights $W^F$ and biases $bi^F$ are learnable parameters, $LayerNorm(\cdot)$ denotes the layer normalization procedure, and $Sublayer(\cdot)$ denotes the attention mechanism or FF layer.

Therefore, the procedure of Transformer in TT and ST can be formulated as follows:

$$\mathbf{H}_{in} = PE(\mathbf{H}) \tag{3.13a}$$

$$\mathbf{H}_{mid} = AN(MHA(\mathbf{H}_{in}, \mathbf{H}_{in}, \mathbf{H}_{in})) \tag{3.13b}$$

$$\mathbf{H}_{out} = AN(FFN(\mathbf{H}_{mid})) \tag{3.13c}$$

To balance the spatial features learned by the transformer and the GCN, an additional gate mechanism proposed by [161] is applied in ST before output, which can be formulated as follows:

$$\rho = sigmoid\,(Linear\,(\mathbf{H}_{out}) + Linear(GCN\,(\mathbf{H}_{in}, \mathscr{A})) \tag{3.14a}$$

$$\mathbf{H}_{out} = \rho\mathbf{H}_{out} + (1-\rho)GCN(\mathbf{H}_{in}) \tag{3.14b}$$

(3) STT is designed to merge spatial and temporal characteristics. The structure of STT is similar to TT except that the self-attention mechanism is substituted by the cross-attention mechanism. Since the dimension of spatial hidden states is different from that of temporal hidden states, we first extract the target macro states from the spatial hidden states according to the road number. Specifically, for the road segment $q$ from node $i$ and $j$, we select the $i$-th row and $j$-th column of hidden states and add them together, then input them with temporal hidden states into the

cross-attention mechanism. The formulations are shown as follows:

$$\mathbf{H}_q^{spat} = Reshape(\mathbf{H}[i]^{spat} + \mathbf{H}[j]^{spat\top}) \tag{3.15a}$$

$$\mathbf{H}_{mid}^{fuse} = AN(MHA(\mathbf{H}^{temp}, \mathbf{H}_q^{spat}, \mathbf{H}_q^{spat}))) \tag{3.15b}$$

Where $\mathbf{H}_r^{spat}$ denotes the spatial hidden states for road $q$, $\mathbf{H}^{temp}$ denotes the hidden states generated by TT, respectively. $Reshape(\cdot)$ denotes the function to rearrange the dimension to be the same as $\mathbf{H}^{temp}$.

Finally, the hidden states generated by STT are input to the output layer, which consists of fully connected layers with ReLu activation functions, then we can obtain the multiple-step predicted speed for preceding vehicles.

### 3.3.2 Robust Learning-in-the-loop MPC

We first discretize and reformulate the dynamics (3.7), taking into account system disturbance $d(s) \in \mathbb{D}$ for further introduction of the robust MPC as follows:

$$x(s+1) = Ax(s) + Bu(s) + \Upsilon(s) + d(s) \tag{3.16}$$

$$A = \begin{bmatrix} 1 & 0 \\ 0 & 1 - \frac{2C_d}{m}\Delta s \end{bmatrix}, B = \begin{bmatrix} \Delta s & 0 \\ 0 & 2\frac{\eta_t}{r}\Delta s \end{bmatrix},$$
$$\Upsilon(s) = \begin{bmatrix} -1/\left(\sqrt{2\hat{E}_0(s)/m_0}\right)\Delta s \\ -mg\Big(\sin\theta(s) + C_f\cos\theta(s)\Big)\Delta s \end{bmatrix}.$$

The state vector $x(s)$ is determined as $x(s) = [\Delta t(s)\ E(s)]^\top$, and $x(s) \in \mathbb{X}$ represents the state constraint as:

$$\mathbb{X} = \left\{ x(s) \mid \Delta t_{\min} \le \Delta t(s) \le \Delta t_{\max},\ \frac{1}{2}mV_{\min}^2 \le E(s) \le \frac{1}{2}mV_{\max}^2 \right\}$$

where $\{V_{\min}, V_{\max}\}$ are the speed limit of CAV. Next, the system disturbance $d(s)$ is specified, where $d_{[1,1]}(s)$ denotes the mismatch between $1/\left(\sqrt{2E_0(s)/m_0}\right)\Delta s$ and $1/\left(\sqrt{2\hat{E}_0(s)/m_0}\right)\Delta s$, and $d_{[2,1]}(s)$ accounts for the modeling uncertainties caused

by parameter induction (e.g. $C_d$, $C_f$, etc.). Following this, $\mathbb{D}$ is defined as $\mathbb{D} = \{d(s) \in \mathbb{R}^2 \mid ||d(s)||_\infty \leq \overline{d} \in \mathbb{R}_{>0}\}$, which is a compact convex set.

Next, the nominal system corresponding to the actual dynamics (3.16) is presented as follows:

$$\bar{x}(s+1) = A\bar{x}(s) + B\bar{u}(s) + \Upsilon(s) \tag{3.17}$$

where $\bar{x}(s) = [\Delta\bar{t}(s)\ \bar{E}(s)]^\top$ denotes the nominal state and $\bar{u}(s) = [\bar{\xi}(s)\ \bar{T}(s)]^\top$ denotes the nominal control input, respectively. Herein, we define the discrepancy $e(s)$ between the actual state $x(s)$ and the nominal state $\bar{x}(s)$ as

$$e(s) = x(s) - \bar{x}(s), \tag{3.18}$$

and the control law can be constructed by

$$u(s) = \bar{u}(s) + Ke(s). \tag{3.19}$$

Based on (3.16), (3.17), (3.18) and (3.19), the dynamics of $e(s)$ can be governed by:

$$e(s+1) = (A + BK)e(s) + d(s). \tag{3.20}$$

Then, $\mathbb{E}$ accounts for the robust invariant set of $e(s)$, which can be obtained by:

$$\mathbb{E} = \oplus_{s=0}^{\infty}(A + BK)^s\mathbb{D} \tag{3.21}$$

Therefore, if the nominal state $\bar{x}(s)$ and the nominal input $\bar{u}(s)$ satisfy

$$\bar{x}(s) \in \mathbb{X} \ominus \mathbb{E},\ \bar{u}(s) \in \mathbb{U} \ominus K\mathbb{E}, \tag{3.22}$$

the satisfaction of $x(s) \in \mathbb{X}$ and $u(s) \in \mathbb{U}$ can be guaranteed. Additionally, the tube size is designed according to the varying forecasted speed of the preceding vehicle, aiming to achieve less conservative results. Before introducing the design process, we first present the concept of the reachable range of the state $E_0(s) \in \{\underline{E}\big(\hat{E}_0(s)\big), \bar{E}\big(\hat{E}_0(s)\big)\}$ over $N_p$ steps, where $N_p$ is the length of the predic-

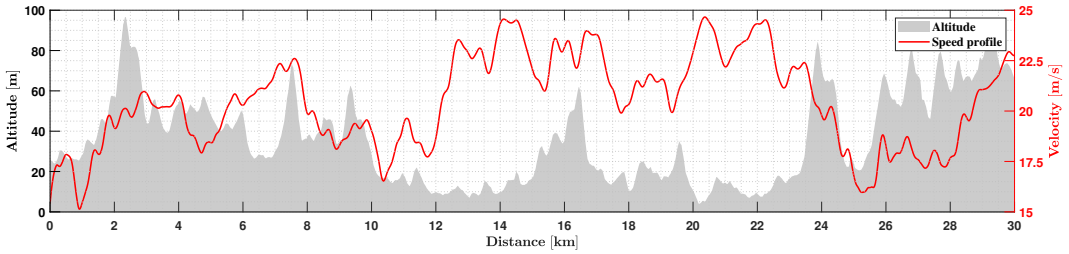


Figure 3.6: Velocity profile and road slope angle.

tive horizon. These ranges can be determined by applying minimum and maximum input torque to the system dynamic (3.16) over the prediction horizon, as shown below:

$$\underline{E}\big(\hat{E}_0(s)\big) = (1-\frac{2C_{d,0}}{m_0}\Delta s)^{N_p-1}\hat{E}_0(s) + \sum_{j=0}^{N_p-2}(1-\frac{2C_{d,0}}{m_0})^j \Big(2\frac{\eta_{t,0}}{r_0}T_{0,\min} - m_0 g\big(\sin\theta(s+j) + C_f\cos\theta(s+j)\big)\Big)\Delta s$$

and

$$\bar{E}\big(\hat{E}_0(s)\big) = (1-\frac{2C_{d,0}}{m_0}\Delta s)^{N_p-1}\hat{E}_0(s) + \sum_{j=0}^{N_p-2}(1-\frac{2C_{d,0}}{m_0})^j \Big(2\frac{\eta_{t,0}}{r_0}T_{0,\max} - m_0 g\big(\sin\theta(s+j) + C_f\cos\theta(s+j)\big)\Big)\Delta s.$$

Following this, the tube size can be precomputed offline as follows:

**Algorithm 1** Offline design of the tube size

1: Divide $\{E_{0,\min}, E_{0,\max}\}$ into $n$ parts and define $\delta = \frac{E_{0,\max}-E_{0,\min}}{n}$;
2: Each subset of $\{E_{0,\min}, E_{0,\max}\}$ can be represented by $\{\underline{E}(E_{0,\min} + k\delta), \bar{E}(E_{0,\min} + k\delta)\}, k \in \{0,1,2,...,n-1\}$;
3: Calculate $\bar{\mathbb{X}}(k) = \mathbb{X}(k) \ominus \mathbb{E}$ for each subset through (3.16) to (3.22);

For the sake of the brevity, the tightened sets are rewritten into

$$\bar{x}(s) \in \bar{\mathbb{X}}(k), \ \bar{u}(s) \in \bar{\mathbb{U}} \tag{3.23}$$

In summary, the local MPC problem $\mathscr{P}(s)$ at step $s$ is formulated as follows:

$$\mathscr{P}(s):$$

$$\min_{\bar{u}} \; J(s) = \sum_{j=0}^{N_p-1} l\left(\bar{x}(j|s), \bar{u}(j|s), \hat{x}_0(s+j)\right) \tag{3.24a}$$

**s.t.**

$$\bar{x}(j+1|s) = A\bar{x}(j|s) + B\bar{u}(j|s) + \Upsilon(j|s) \tag{3.24b}$$

$$\bar{x}(j|s) \in \bar{\mathbb{X}}(k) \tag{3.24c}$$

$$\bar{u}(j|s) \in \bar{\mathbb{U}} \tag{3.24d}$$

$$(\bar{x}(j|s), \bar{u}(j|s)) \in \bar{\mathbb{X}}(k) \times \bar{\mathbb{U}} \tag{3.24e}$$

$$\bar{x}(0|s) = x(s) \tag{3.24f}$$

where the stage cost function $l\left(\bar{x}(j|s), \bar{u}(j|s), \hat{x}_0(s+j)\right)$ in (3.24a) can be specified:

$$\begin{aligned} l = W_1|\Delta\bar{t}(j|s) - \Delta| + W_2|\bar{E}(j|s) - \frac{m}{m_0}\hat{E}_0(s+j)| \\ + W_3|T(j|s) - h(j|s)| + W_4 P(j|s) + W_5\xi(j|s). \end{aligned} \tag{3.25}$$

$W_1|\Delta\bar{t}(j|s) - \Delta|$ and $W_2|\bar{E}(j|s) - \frac{m}{m_0}\hat{E}_0(j|s)|$ are configured to preserve the car-following performance; $W_3|T(j|s) - h(j|s)|$ is set to improve passenger comfort, where $h(j|s)$ denotes the equilibrium input torque as

$$h(j|s) = \frac{r}{\eta_t}\Big(\frac{2C_d}{m}\hat{E}_0(j|s) + mg\big(\sin\theta(s+j) + C_f\cos\theta(s+j)\big)\Big) \tag{3.26}$$

$W_4 P(j|s)$ penalizes energy consumption, where $P(j|s)$ represents the power of in-wheel motor based on (3.2); The final term $W_5\xi(j|s)$ ensures the validity of the control solution.

Dynamic equation (3.24b) represents the nominal system introduced in (3.17); Constraints (3.24c) and (3.24d) are robust state and input constraints, corresponding to the tube size design; (3.24e) denotes a coupled constraint which enforces system

convexity as follows:

$$\bar{\mathbb{X}}(k) \times \bar{\mathbb{U}} = \left\{ (\bar{E}(j|s), \bar{\xi}(j|s)) \mid \bar{\xi}(j|s) \geq \frac{1}{\sqrt{2\hat{E}(s+j)/m}} \right\} \tag{3.27}$$

The initial condition of the MPC is specified by (3.24f) which employs the actual state. Overall, the proposed robust control approach is summarized in Algorithm 2.

**Algorithm 2** The robust learning-in-the-loop MPC approach for ego vehicle

**Offline:**

a) Find the control gain $K$ via pole-placement method;
b) Select suitable weighting parameters $W_1, W_2, W_3, W_4, W_5$ and the prediction horizon $N_p$ for the OCP $\mathscr{P}$;
c) Calculate $\bar{\mathbb{X}}(k), k \in \{0, 1, 2..., n-1\}$ via Algorithm 1;

**Online:**

**while** $0 \leq s < \bar{s}$ **do**
  Measure current states $x_0(s)$ and $x(s)$;
  Receive $\hat{x}_0(:|s)$ from the preceding vehicle;
  Check to which subset $\{\underline{E}(E_{0,\min} + k\delta), \bar{E}(E_{0,\min} + k\delta)\}$ $\hat{E}_0(s)$ belongs;
  Invoke corresponding $\bar{\mathbb{X}}(k)$;
  Set the initial condition (3.24f) of the MPC problem $\mathscr{P}(s)$ based on the measured values $x_0(s)$ and $x(s)$;
  Generate $\hat{x}(:|s)$ through the speed predictor;
  Solve OCP $\mathscr{P}(s)$ and obtain $\bar{u}(:|s)$ and $\bar{x}(:|s)$;
  Apply the control action $u(s) = \bar{u}(0|s) + Ke(s)$ with $e(s) = x(s) - \bar{x}(0|s)$ to the actual system (3.16);
  $s \rightarrow s+1$;
**end while**

## 3.4 Simulation

In this section, we showcase the performance of the LEC strategy, focusing on key aspects such as prediction accuracy, energy consumption, and computational efficiency. Numerical simulations are conducted to highlight the advantages of the proposed strategy compared to several state-of-the-art algorithms, which are introduced in Subsection 3.4.1. Relevant parameters for simulations and the on-road experiment are summarized in Table 3.1.

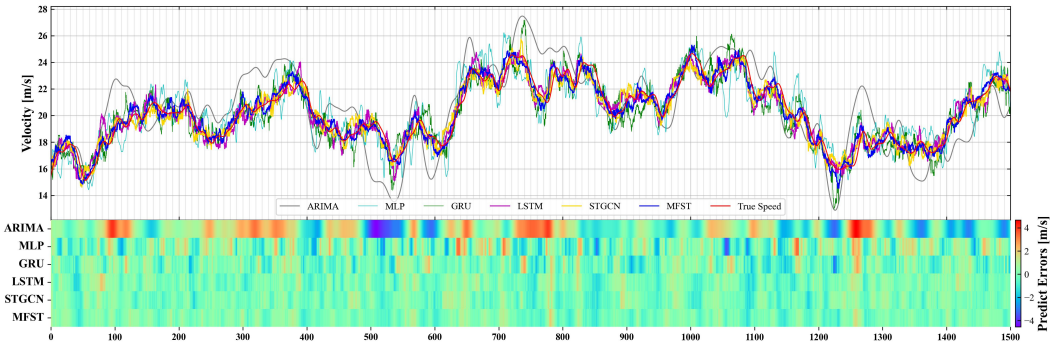


Figure 3.7: Prediction results and predicted errors.

Table 3.1: Simulation parameters

| Description | Symbols | Values |
|---|---|---|
| Ego vehicle mass | $m$ | 2000 kg |
| Motor transmission efficiency | $\eta_t$ | 0.95 |
| Tire radius | $r$ | 0.36 m |
| Air-drag coefficient | $C_d$ | 0.28 |
| Tyre rolling resistance coefficient | $C_f$ | 0.015 |
| Gravity constant | g | 9.8 N/kg |
| Motor fitting parameters | $a; b; c$ | 0.01078; 22.23; 67.63 |
| Maximum Torque | $T_{\max}$ | 1225 Nm |
| Minimal Torque | $T_{\min}$ | $-1225$ Nm |
| Predictive Horizon Length | $N_p$ | 10 |
| Sampling distance interval | $\Delta s$ | 2 m |
| Desired time headway | $\Delta$ | 1 s |
| Minimum time headway | $\Delta t_{\min}$ | 0.5 s |
| Maximum time headway | $\Delta t_{\max}$ | 1.5 s |

### 3.4.1 Benchmarks

Comparisons with corresponding algorithms are in terms of prediction accuracy, computation efficiency, and energy consumption, which are introduced as follows: Regarding prediction accuracy, we apply several baseline models for comparison, including ARIMA, MLP, LSTM [162], GRU [163], and STGCN [164]. Considering the computation time of the LEC strategy, we first set a nonlinear car-following approach [165] as a benchmark and extend the comparison with a state-of-the-art real-time algorithm [166]. Concerning energy consumption, the proposed LEC algorithm initially compares with an Eco-driving benchmark [167] with a feedback mechanism and further compares with an IDM-based method [168].

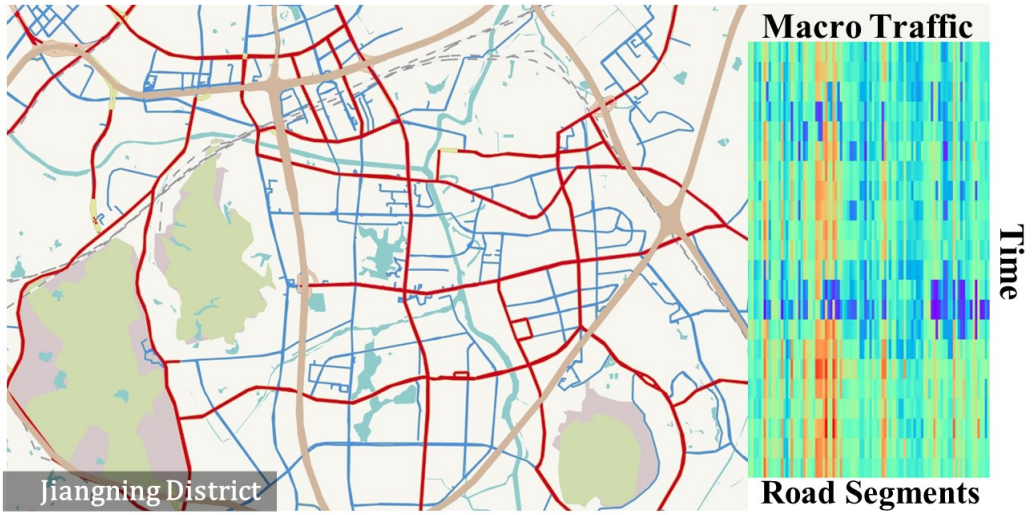


Figure 3.8: Map of the study area and macro traffic speed data. The data was collected every second from 150 road segments over one month. The subplot on the right illustrates the spatiotemporal distribution of traffic speed, with the horizontal axis representing individual road segments, the vertical axis representing time, and the color gradient from blue to red indicating an increase in speed from low to high.

### 3.4.2 Prediction Accuracy

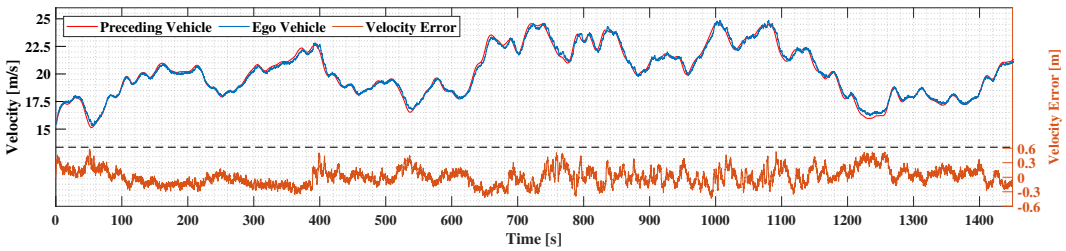


Figure 3.9: Velocity and velocity error.

The data for this study was collected from the road network in Jiangning District, Nanjing, China, during the period of June 2020, as shown in Fig. 3.8. The macro traffic data are collected by vehicle monitoring and tracking systems, which are counted as 1-second granularity and interpolated at 0.5 km intervals. The adjacent matrix is generated according to the road network within the study area. The micro-level vehicle speed data was obtained from multiple instances of vehicle-following recordings. Weather data collected from Weather Underground is also processed to match the dimensions of the micro and macro traffic data.

In this study, each time step represents 1 second, and 10-second speed data are input as historical information to predict the future two-step speed. We divided the dataset into training and test sets in a ratio of 8 to 2 and used it for model training. To validate the advantage of MFST, the prediction performance is compared based on various error metrics, including Mean Squared Error (MSE), Root Mean Squared Error (RMSE), Mean Absolute Error (MAE), and R-square ($R^2$). The results are summarized in Table 3.2. It can be seen that our proposed method obtains the best prediction performance.

As car-following control requires finer time granularity, 0.1 seconds in this study, we applied linear interpolation and sliding median method to process the predicted speed. To further validate our predictor, we predict the preceding vehicle speed recorded from a 30 km trip, and the raw speed data and road slope are shown in Fig. 3.6. The predicted results are shown in Fig. 3.7, in which the lines illustrate the predicted results of the proposed model along with that of the baseline models and ground truth, and the heatmap represents the predicted errors (i.e. the difference between predicted and true values). It is observed that our model presents a better temporal pattern and fewer errors among all selected models.

Table 3.2: Results of prediction performance

| | MSE | MAE | RMSE | R2 |
|---|---|---|---|---|
| ARIMA | 74.96 | 8.03 | 8.66 | 0.06 |
| MLP | 30.26 | 4.79 | 5.50 | 0.15 |
| GRU | 22.85 | 4.04 | 4.78 | 0.17 |
| LSTM | 10.41 | 2.73 | 3.23 | 0.34 |
| STGCN | 7.84 | 2.38 | 2.80 | 0.40 |
| MFST | **4.98** | **1.89** | **2.23** | **0.51** |

### 3.4.3 Car-following Performance

The car-following performance of the proposed strategy is investigated in this subsection, and the results are demonstrated in Fig. 3.9. Specifically, the red line denotes the speed profile of the preceding vehicle (The same as depicted in Fig. 3.6), while the blue line illustrates the tracking performance of the ego vehicle. Considering the data provided above, the tracking error, indicated in orange, does not

exceed $\pm 0.6$ m/s at its maximum. Additionally, the input torque and corresponding acceleration of the ego vehicle are presented in Fig. 3.10. By employing the control objective $W_3|T(j|s) - h(j|s)|$, the acceleration remains within $\pm 0.31$ m/s$^2$, aligning with the 'excellent acceleration' criterion outlined in [169].

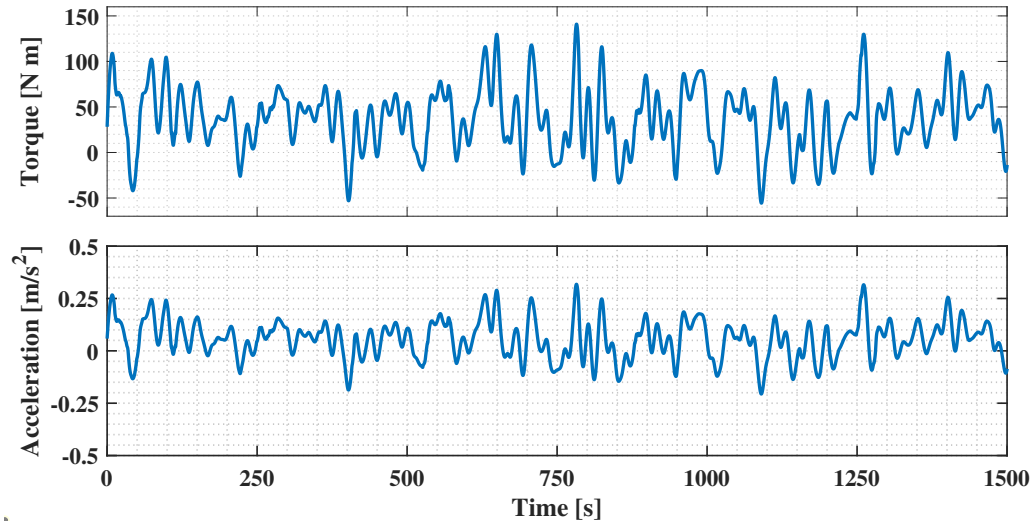


Figure 3.10: Input torque and acceleration.

Additionally, the effectiveness of robust control is also studied. In Fig. 3.11, it can be observed that if a nominal MPC without the tightened constraint (3.24c) is taken into account, the safety constraint is violated at the position 576 m, which could cause a collision with its preceding vehicle. Note that the scope of safety constraint is changing because we present the distance headway instead of the constant time headway here.

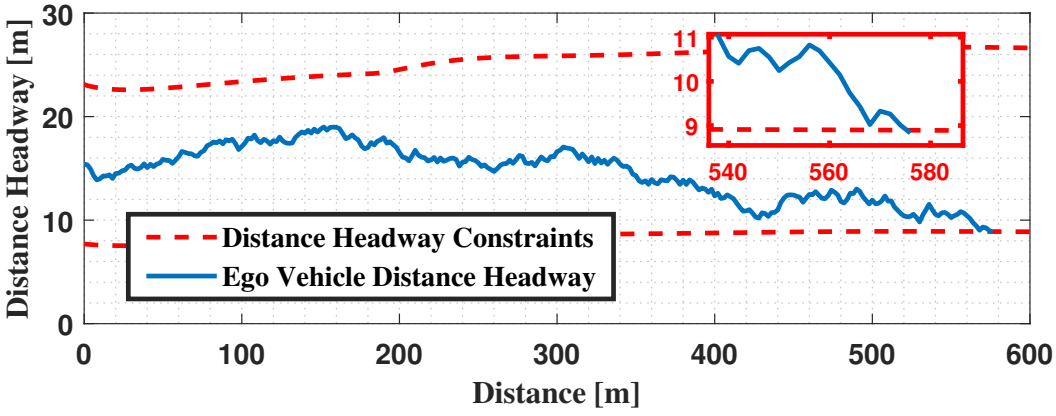


Figure 3.11: Car-following performance without robust control.

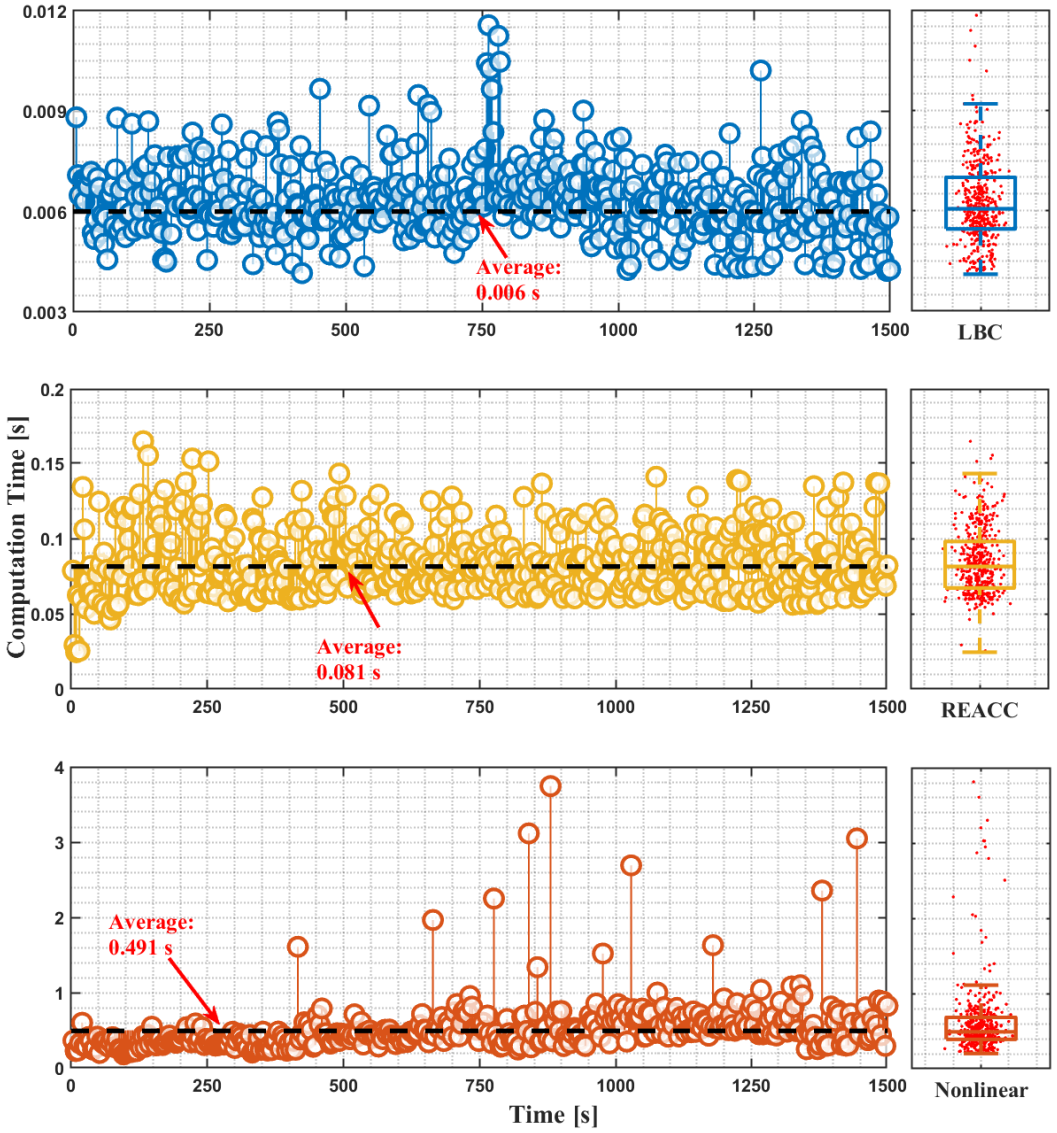


Figure 3.12: Computation load of different methods: Top-LEC Strategy; Middle-REACC Algorithm; Bottom-Nonlinear Benchmark.

### 3.4.4 Computation Efficiency

This subsection investigates the real-time computation capabilities of the proposed strategy. To underscore the computational efficiency of the LEC algorithm, a nonlinear benchmark [165] and a recently published real-time ecological ACC (REACC) algorithm [166] are set for comparison. Numerical simulation results are illustrated in Fig. 3.12, where LEC is in blue, the nonlinear benchmark is in yellow and REACC is in orange. Specifically, the average computation time of the

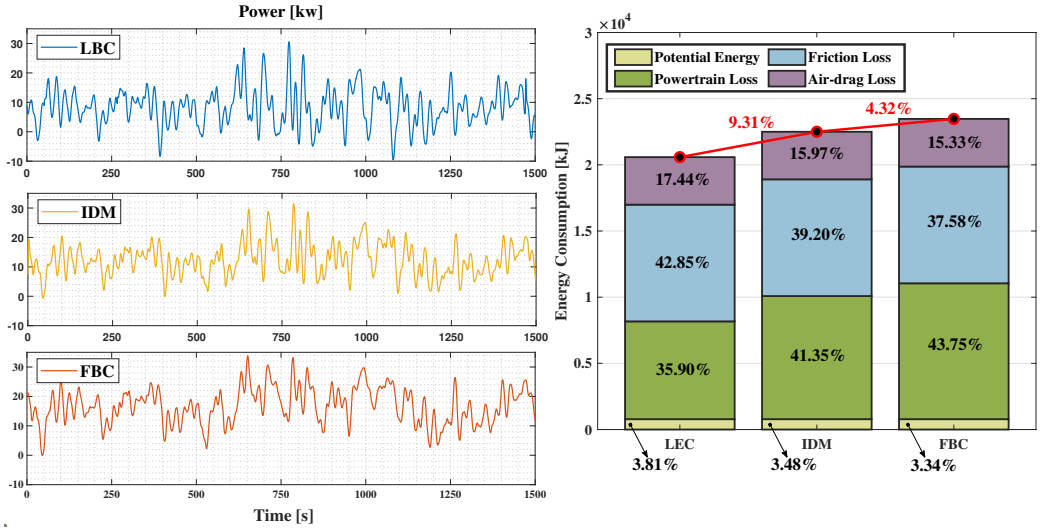


Figure 3.13: Power and energy consumption.

proposed strategy is 0.006 s per step, with a maximum value of 0.01 s. Taking into account the length of the spatial sampling interval $\Delta s = 2$ m and $V_{\max} = 40$ m/s, the time required for traversing this distance is 0.05 s, meeting the real-time requirement. In comparison, the average time cost of the nonlinear benchmark is 0.491 s and the average computation time of the REACC is 0.081 s. The proposed LEC strategy achieves a computation speed 10 times faster than that of REACC, showcasing significantly enhanced real-time computational capabilities.

### 3.4.5 Energy Consumption

The energy consumption of the proposed strategy is studied in this subsection, and its advantages are further emphasized through a comparison with two additional methods. Simulation results are shown in Fig. 3.13, which employs a feedback control mechanism [167] in orange and another IDM-based strategy [168] in yellow. In detail, owing to the feedback mechanism, the benchmark method places a higher emphasis on car-following performance, thereby at the expense of energy consumption. On the other hand, the IDM strategy is based on imitating the behavior of human drivers, favoring gentle speed changes. Compared to the benchmark, it exhibits greater energy efficiency; however, it is still inferior to the proposed LEC strategy. This is attributed to maximizing the penalty weight assigned to energy consumption in the optimization objective of the proposed method while satisfying

all constraints. Furthermore, the total energy consumption among the three strategies is summarized, where the LEC strategy saves 9.31 % of energy in comparison to the IDM strategy, and a 13.63% energy savings to the feedback control strategy (FBC). In detail, energy consumption can be categorized into four types: powertrain loss, tyre friction loss, air-drag loss, and potential energy loss. The proposed strategy primarily saves energy in powertrain loss by reducing braking and keeping input torque and vehicle speed in the high-efficiency range.

## 3.5 On-road Vehicle Experiment

In order to highlight the practical applicability of the proposed strategy, the on-road experiment is conducted. Due to traffic regulations, the ego vehicle only tracks the preceding vehicle for a distance of 3.5 km (Speed profile of the preceding vehicle is introduced in Section 3.4).

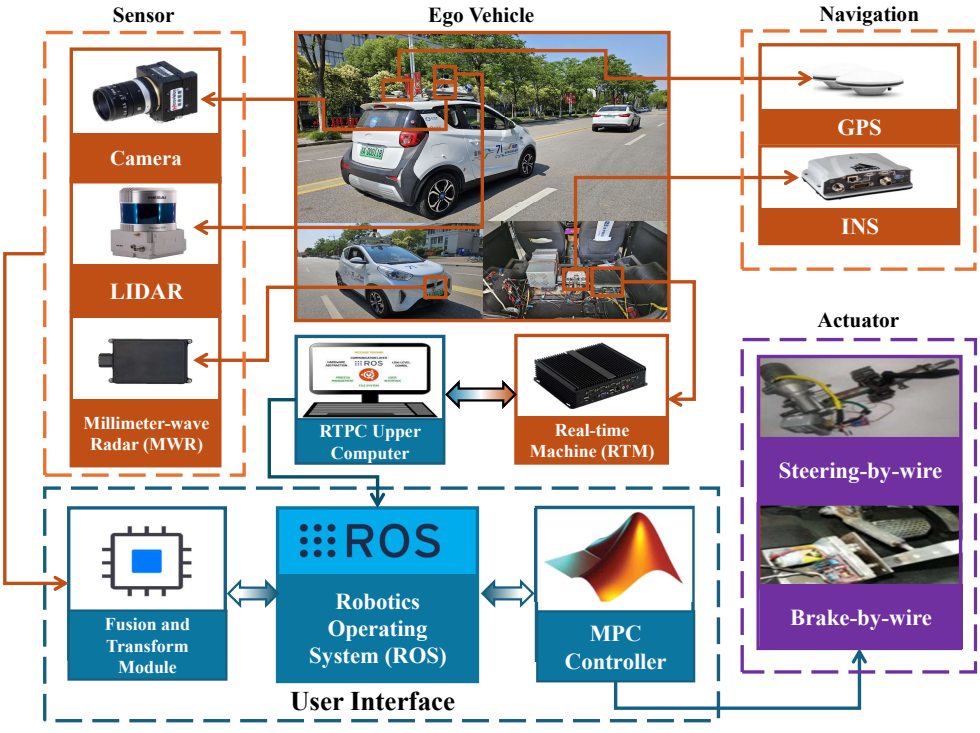


Figure 3.14: On-road vehicle experiment.

As shown in Fig. 3.14, a modified CAV based on a Chery BEV eQ1 [170] is employed for this experiment. Through integrating the equipped LIDAR, cam-

era, and Millimeter-wave Radar (MWR), the surrounding environmental data can be fused and then transformed into the spatial domain. Further combined with the navigation module consisting of Global Positioning System (GPS) and Inertial Navigation System (INS), the reference trajectory and motion constraints are generated and applied to the proposed MPC-based controller. Subsequently, the input commands calculated by the built-in LEC algorithm are transmitted to the actuators of the tested CAV, including brake-by-wire and steering-by-wire (enclosed by the purple box in Fig. 3.14). The aforementioned experimental modules are built and connected together based on the Robotics Operating System (ROS), which is operating on Ubuntu 16.04 LTS.

The experimental results are presented in Fig 3.15, recording the velocity changes, velocity error and spacing distance of the test vehicles. It is noted that the spacing distance (from the rear of the preceding vehicle to the front of the ego vehicle) increases gradually due to our control target of maintaining a constant time headway rather than a constant spacing distance. As the preceding vehicle accelerates, this spacing distance also increases.

## 3.6 Conclusion

This chapter addresses a car-following problem for connected and autonomous electric vehicles. Through a spatial-temporal transformer, micro and macro traffic information are fused for preceding vehicle speed prediction. Resulting errors are handled by a robust learning-in-the-loop MPC method in the control layer. Meanwhile, the receding horizon optimization problem is reformulated into a convex form, transforming from the time domain to the spatial domain, which improves the computation efficiency and enables real-time implementation. The advantages of the LEC strategy are highlighted in comparison with several state-of-the-art algorithms in terms of prediction accuracy, energy consumption, and computational efficiency. Moreover, an on-road vehicle experiment is conducted to confirm that the proposed strategy has the capability for practical applications.

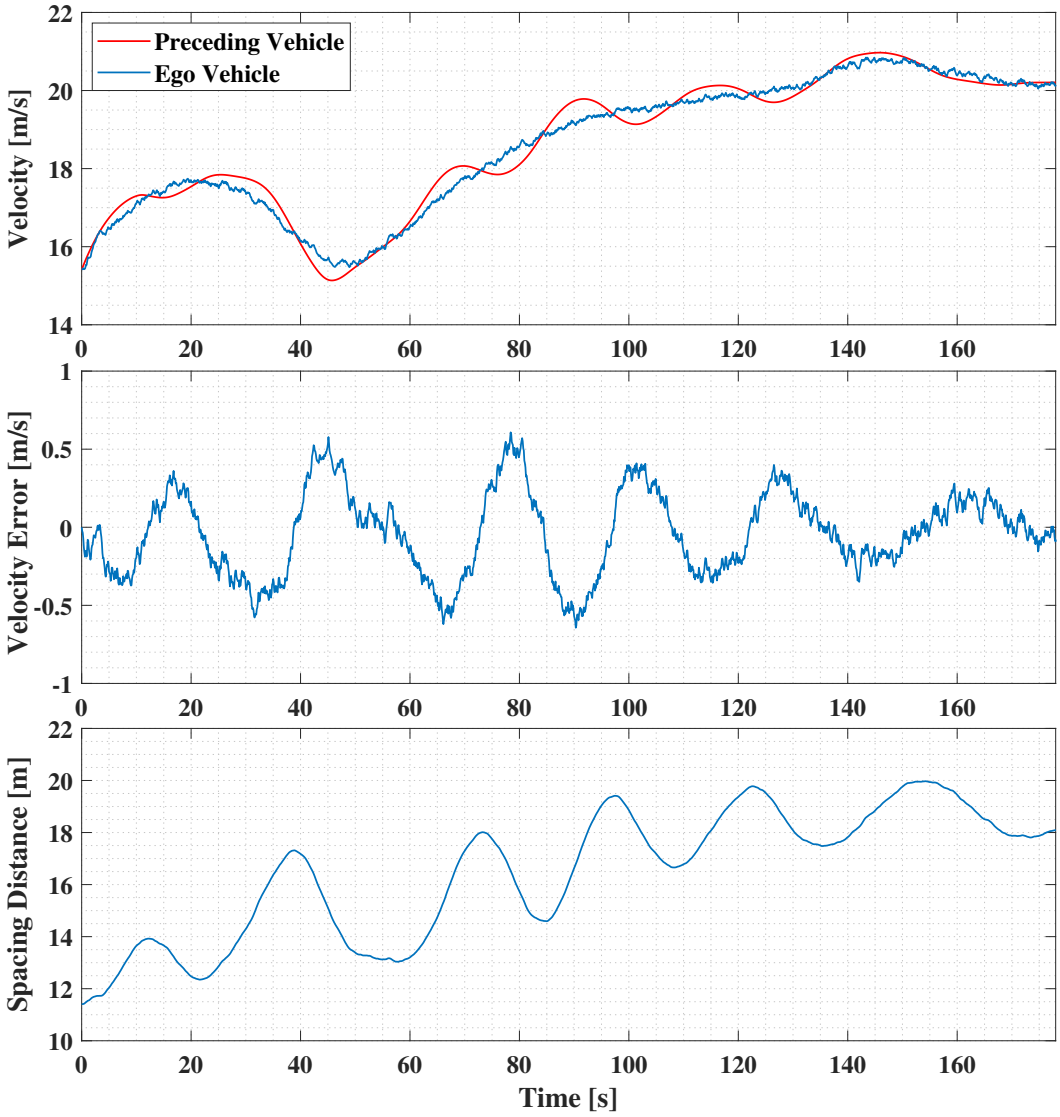


Figure 3.15: The results of the VIL experiment: Top-Velocity changes; Middle-Velocity error; Bottom-Spacing distance.

# Chapter 4

# Heterogeneous CAVs Platooning Problem

## 4.1 Introduction

In this chapter, a convex and robust DMPC algorithm is proposed to achieve a heterogeneous vehicle platoon in the longitudinal direction by considering a time-varying leader speed with superior optimization efficiency and certified theoretical properties. The proposed distributed control scheme is based on the PF communication protocol, which does not impose significant communication demand as compared to PLF in [171] and the bidirectional topology in [110]. Both process and measurement disturbances are considered to capture more realistic uncertainties in practice. The effectiveness of the proposed method and its advantages over the existing approaches are demonstrated by numerical simulations and comparisons. The contributions are summarized as follows:

- The traditional nonlinear vehicle platooning problem is reformulated by a spatial domain modeling approach with respect to vehicle kinetic energy and the time gap between adjacent vehicles. In this context, coupled state constraints for collision avoidance and platoon formation can be decoupled, such that feasibility and stability guarantees can be justified in a more handy way. Moreover, space-dependent coefficients, such as the rolling resistance and road slopes, can be accurately modeled.

- Following the last point, a convex optimization-based control framework is developed so that the optimal solution can be efficiently obtained at each step. Quantitative analysis in terms of computational efficiency is performed in the simulation section by numerical comparison with a traditional nonlinear DMPC approach. Moreover, the validity of the convex reformulation is rigorously analyzed.

- In contrast to the existing works that consider only partial disturbances in the platoon system, both unmodeled motion dynamics, and sensor measurement disturbances of the position and velocity are considered and addressed in this chapter by a tube-based DMPC approach. The theoretical analysis reveals the DMPC parameter tuning criteria by which recursive feasibility and input-to-state stability (ISS) of the proposed algorithm can be guaranteed when the velocity of the leader vehicle reaches a steady state.

The remainder of this chapter is organized as follows. The modeling framework and the communication topology are introduced in Section 4.2. In Section 4.3, the methodology of this distributed robust platoon control problem is proposed. In Section 4.4, theoretical analysis of recursive feasibility, Lyapunov asymptotic stability and auxiliary variable validation are demonstrated. Simulation results are presented in Section 4.5. Finally, Section 4.7 concludes this work.

## 4.2 Problem Statement

As shown in Fig. 4.1, this paper considers a vehicle platoon of $N+1$ heterogeneous CAVs. Without loss of generality, the leading CAV is indexed by 0 and the followers are index by $i \in \mathscr{N}$ with $\mathscr{N} = \{1, 2, \cdots, N\}$.Vehicle-to-vehicle (V2V) communication is enabled in the platoon and follows a unidirectional PF information flow topology by which each vehicle only receives information from the one immediately ahead. This communication protocol is commonly used in vehicle platooning due to its relatively lower data exchange demand compared to other topologies.

Next, we will first briefly review the nominal time-domain modeling frame-

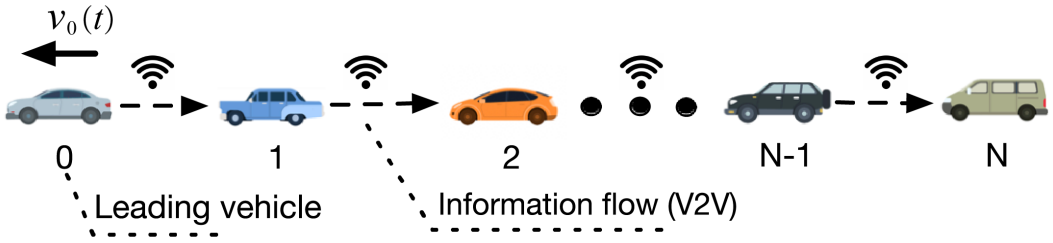


Figure 4.1: A heterogeneous vehicle platoon with the PF communication protocol.

work of the platooning problem, and then a convex reformulation of the problem in the space domain will be introduced.

### 4.2.1 The Nominal Modeling Framework in Time domain

The longitudinal dynamics of each following vehicle are described as:

$$\dot{s}_i(t) = v_i(t), \tag{4.1a}$$

$$\dot{v}_i(t) = \frac{1}{m_i}\left(\frac{\eta_{t,i}}{r_i}T_i(t) - C_{d,i}v_i^2(t) - m_i g C_{s,i}(t)\right), i \in \mathcal{N} \tag{4.1b}$$

where $s_i(t)$ is the position of vehicle $i$, $v_i(t)$ is the velocity, vehicle mass is denoted by $m_i$, $g$ is the gravity constant, $\eta_{t,i}$ is the final drive ratio, $r_i$ is the tire radius, $C_{d,i}$ is the aerodynamic drag coefficient, and $T_i(t)$ is the driving/braking torque, acting as the control input of the follower. Moreover, $C_{s,i}(t)$ is the synthetic coefficient of the tire friction and gradient forces

$$C_{s,i}(t) = C_{f_i}\cos\theta_i(t) + \sin\theta_i(t), i \in \mathcal{N} \tag{4.2}$$

with $C_{f_i}$ the rolling resistance coefficient and $\theta_i(t)$ the road slope angle.

The common objective of platoon control in the noise-free scenario requires all following vehicles to move at the same speed as the leading vehicle while following the constant time-headway policy between adjacent vehicles [172, 173]:

$$\lim_{t\to\infty} ||v_i(t) - v_0(t)|| = 0, \tag{4.3a}$$

$$\lim_{t\to\infty} ||s_i(t) - s_{i-1}(t) - h(t)|| = 0, \forall i \in \mathcal{N} \tag{4.3b}$$

where $v_0(t) \in [v_{\min}, v_{\max}]$ is the target speed of the leading vehicle, $h(t)$ is the desired spacing, proportional to speed $v_0(t)$. To complete the framework, the following constraints are also required for safety purposes and for the fulfillment of control limits

$$v_{\min} \leq v_i(t) \leq v_{\max}, \tag{4.4a}$$

$$h_{\min} \leq s_i(t) - s_{i-1}(t) \leq h_{\max}, \tag{4.4b}$$

$$T_{i,\min} \leq T_i(t) \leq T_{i,\max}, \forall i \in \mathscr{N} \tag{4.4c}$$

in which $\{v_{\min}, v_{\max}\}$, $\{h_{\min}, h_{\max}\}$ (proportional to $v_{\min}$ and $v_{\max}$ subject to a constant time headway) and $\{T_{i,\min}, T_{i,\max}\}$ represent minimum and maximum limits for the driving speed, headway distance, and individual torque, respectively. As it can be noticed, the speed and headway distance limits are subject to driving conditions (e.g., highway, rural, etc.), thus identical for all vehicles.

### 4.2.2 A Convex Modeling Approach

Instead of the commonly used time-domain modeling approach with respect to the position and velocity of individual vehicles, as given in (4.1)-(4.4), this paper proposes to use a novel space domain modeling approach with state transformation to reformulate the platooning system, which 1) permits the control problem to be formulated as a convex optimization problem for rapid solution search, and 2) facilitates the design of the DMPC algorithm, as will be elaborated later.

Consider $s$ the independent variable of traveled space (waypoint on the line of travel). The transformation from time to space domain is accomplished by replacing the independent variable $t$ with $s$ via $\frac{d}{ds} = \frac{1}{v}\frac{d}{dt}$. Let $E_i(s) = \frac{1}{2}m_i v_i^2(s)$ and $\Delta t_i(s) = t_i(s) - t_{i-1}(s), \forall i \in \mathscr{N}$ denote the kinetic energy of vehicle $i$ and its time headway with respect to the preceding $(i-1)$-th vehicle, respectively. In view of (4.1), the dynamics of both variables in the space domain are governed by the fol-

lowing differential equations:

$$\frac{d}{ds}\Delta t_i(s) = \frac{1}{\sqrt{2E_i(s)/m_i}} - \frac{1}{\sqrt{2E_{i-1}(s)/m_{i-1}}}, \tag{4.5a}$$

$$\frac{d}{ds}E_i(s) = \frac{\eta_{t,i}}{r_i}T_i(s) - 2\frac{C_{d,i}}{m_i}E_i(s) - m_i g C_{s,i}(s). \tag{4.5b}$$

where $E_i(s) > 0, \forall s$ to avoid the singularity and it can be enforced by (4.7a) with $v_{\min} > 0$. As a consequence, the nominal objectives (4.3) and the constraints (4.4) can be replaced by:

$$\lim_{s\to\infty} ||E_i(s) - \frac{1}{2}m_i v_0^2(s)|| = 0 \tag{4.6a}$$

$$\lim_{s\to\infty} ||\Delta t_i(s) - \Delta_0|| = 0, \forall i \in \mathcal{N} \tag{4.6b}$$

and

$$E_{i,\min} \leq E_i(s) \leq E_{i,\max}, \tag{4.7a}$$

$$\Delta t_{\min} \leq \Delta t_i(s) \leq \Delta t_{\max}, \tag{4.7b}$$

$$T_{i,\min} \leq T_i(s) \leq T_{i,\max}, \forall i \in \mathcal{N} \tag{4.7c}$$

where $E_{i,\min} = \frac{1}{2}m_i v_{\min}^2$ and $E_{i,\max} = \frac{1}{2}m_i v_{\max}^2$, $\Delta_0$ is the desired time headway between consecutive vehicles. Note that $v_{\min}$ in the space domain formulation can only be set to a non-zero constant to prevent singularity issues in (4.5a). [1] Being $E_i(s) > 0$, (4.6a) is equivalent to (4.3a). The time headway target (4.6b) and the constraint (4.7b) are surrogates of the headway distance objective and constraint given in (4.3b) and (4.4b) with $\Delta t_{\min}$ and $\Delta t_{\max}$ the minimum and maximum time headway, respectively. By substituting the coupled state constraints (4.4b) with the state constraint (4.7b), the uncertainties involved in the information received from the preceding vehicle can be immediately taken into consideration as the modeling error in (4.5a).

Now, we have all ingredients to formulate the distributed control problem for

[1] In the low driving speed scenario (e.g, urban driving), $v_{\min}$ can be set to a sufficiently small positive constant to avoid sacrificing the generality of the formulation.

CAV $i$ in the space domain.

**OCP 3**

$$\min_{T_i} \quad J_i(\Delta t_i, E_i, T_i) \tag{4.8a}$$

$$\textbf{\textit{s.t.}} : (4.5), (4.7) \tag{4.8b}$$

where the cost function $J_i(\Delta t_i, E_i, T_i)$ related to the quadratic control objectives (4.6), will be designed later in 4.3.2. It is noteworthy that OCP 3 is a non-convex programming problem because of the nonlinear dynamics in (4.5a). In order to improve the computational efficiency, a convex reformulation of (4.5a) is utilized:

$$\frac{d}{ds}\Delta t_i(s) = \xi_i(s) - \frac{1}{v_{i-1}(s)} \tag{4.9a}$$

$$\xi_i(s) \geq \frac{1}{\sqrt{2E_i(s)/m_i}}, i \in \mathscr{N} \tag{4.9b}$$

where $\xi_i(s)$ is a fictitious control input. As it can be seen, the nonlinear differential equation (4.5a) is relaxed by a combination of linear differential equations and a convex constraint. Consequently, OCP 3 can be convexified, leading to

**OCP 4**

$$\min_{T_i, \xi_i} \quad J_i(\Delta t_i, E_i, T_i) \tag{4.10a}$$

$$\textbf{\textit{s.t.}} : (4.5b), (4.7), (4.9) \tag{4.10b}$$

It is worth noting that the validity of the solution of OCP 4 relies on the tightness of (4.9b), which is addressed later by Proposition 1 in Section 4.4.

## 4.3 Tube-based Distributed Model Predictive Control

The main algorithm is introduced in this section. In the first place, the reformatted system equations are introduced. Based on that, the tube-based MPC

algorithm is given inherited from the theoretical framework proposed in [159], then the local MPC problem is formulated for each following vehicle under a distributed control mechanism.

### 4.3.1 Tube-based MPC

For sake of introducing the MPC-based algorithm and taking into account system uncertainties, such as modeling error and measurement noise, in a unified framework, the system differential equations (4.5b) and (4.9a) are discretized and rewritten in a normalized form as follows:

$$\begin{aligned} x_i(k+1) &= A_i x_i(k) + B_i u_i(k) + \gamma_i(k) + d_i(k) \\ y_i(k) &= C x_i(k) + w_i(k), i \in \mathcal{N} \end{aligned} \tag{4.11}$$

$$A_i = \begin{bmatrix} 1 & 0 \\ 0 & 1 - \frac{2C_{d,i}}{m_i}\Delta s \end{bmatrix}, B_i = \begin{bmatrix} \Delta s & 0 \\ 0 & \frac{\eta_{t,i}}{r_i}\Delta s \end{bmatrix}, C = \begin{bmatrix} 1 & 0 \\ 0 & 1 \end{bmatrix},$$
$$\gamma_i(k) = \begin{bmatrix} -f_i\big(\hat{\mathscr{E}}_{i-1}(k)\big)\Delta s \\ -\frac{m_i g C_{s,i}(k)}{E_{\max}}\Delta s \end{bmatrix}$$

where $k = 0, 1, \ldots, \bar{k}$, $\Delta s \in \mathbb{R}_{>0}$ denotes the sampling distance interval and $\bar{k}\Delta s$ is the total length of the mission. The normalized state vector of $\Delta t_i$ and $E_i$ is defined as $x_i(k) \triangleq [\delta_i(k)\ \mathscr{E}_i(k)]^\top \in \mathbb{X}_i$ with $\delta_i(k) \triangleq \frac{\Delta t_i(k)}{\Delta t_{\max}}, \mathscr{E}_i(k) \triangleq \frac{E_i(k)}{E_{\max}}$ and $E_{\max} \triangleq \frac{1}{2}\bar{m}v_{\max}^2$, in which $\bar{m} \geq \max_{i\in\mathcal{N}} m_i$. Note that $\bar{m}$ can be conservatively designed without the global information about all vehicles' mass. Then, it holds that

$$\mathbb{X}_i \triangleq \left\{ x_i \mid \frac{\Delta t_{\min}}{\Delta t_{\max}} \leq \delta_i(k) \leq 1, \frac{E_{i,\min}}{E_{\max}} \leq \mathscr{E}_i(k) \leq 1 \right\}.$$

Similarly, the normalized input is denoted by $u_i \triangleq [\zeta_i(k)\ \mathscr{T}_i(k)]^\top \in \mathbb{U}_i$, where $\zeta_i(k) \triangleq \frac{\xi_i(k)}{\Delta t_{\max}}$, $\mathscr{T}_i(k) \triangleq \frac{T_i(k)}{E_{\max}}$ and $\mathbb{U}_i \triangleq \{u_i \mid \frac{T_{i,\min}}{E_{\max}} \leq \mathscr{T}_i(k) \leq \frac{T_{i,\max}}{E_{\max}}\}$. After the normalization, $\mathbb{X}_i \times \mathbb{U}_i$ involving (4.9b) becomes $\zeta_i(k) \geq f_i(\mathscr{E}_i(k))$, where the function

$f_i(\cdot) : \mathbb{R}_{>0} \to \mathbb{R}_{>0}$ is defined as:

$$f_i(\mathscr{E}_i) \triangleq 1/(\Delta t_{\max}\sqrt{2E_{\max}\mathscr{E}_i/m_i}). \tag{4.12}$$

The normalized measurement $y_i$ of $\delta_i$ and $\mathscr{E}_i$ obtained by the $i$th vehicle's onboard sensors (eg, front radar and speedometer). $\gamma_i(k)_{[1,1]}$ represents external information of the preceding vehicle $i-1$. In particular, $\hat{\mathscr{E}}_{i-1}(k)$ is an estimate of $\mathscr{E}_{i-1}(k)$ obtained and shared by the preceding vehicle $i-1$ at step $k-1$, which will be defined later on in Section 4.3.2.

On the other hand, $\gamma_i(k)_{[2,1]}$ embodies the impact of the drag caused by road slope. Owing to the space domain model, space varying coefficient $C_{s,i}(k)$ can be easily incorporated to capture different road conditions, therefore enabling a less conservative disturbance bound in the robust control framework compared to the traditional time-domain scheme. Next, the system uncertainties are defined, $d_i(k) \in \mathbb{D}_i$ is the normalized modeling uncertainty and $w_i(k) \in \mathbb{W}_i$ represents the normalized measurement noise. Herein, $\mathbb{D}_i$ and $\mathbb{W}_i$ are two compact convex sets defined by $\mathbb{D}_i = \{d_i(k) \in \mathbb{R}^2 \,|\, ||d_i(k)||_\infty \leq \overline{d}_i \in \mathbb{R}_{>0}\}$ and $\mathbb{W}_i = \{w_i(k) \in \mathbb{R}^2 \,|\, ||w_i(k)||_\infty \leq \overline{w}_i \in \mathbb{R}_{>0}\}$. As it can be noticed, $d_i(k)$ accounts for the mismatch between the estimate $f_i\big(\hat{\mathscr{E}}_{i-1}(k)\big)\Delta s$ and $f_i\big(\mathscr{E}_{i-1}(k)\big)\Delta s$ that is constructed by the accurate information from the preceding vehicle (the only source of the disturbance appears in the dynamic equation of $\delta_i$) as well as the unmodeled nonlinearities (e.g. headway-dependent air drag coefficients), while sensor measurement noises of the time headway and velocities are taken into account by $w_i$. Consider $\delta_0 \triangleq \Delta_0/\Delta t_{\max}$ the target gap and $\overline{m}_{i,0}\mathscr{E}_0(k)$ the target kinetic energy of vehicle $i$ with $\overline{m}_{i,j} \triangleq m_i/m_j, j \neq i$. The control objective in the presence of uncertainties is defined by

$$\lim_{k\to\infty} ||x_i(k) - x^*_{i,des}(k)|| = \sigma_i \tag{4.13}$$

where $x^*_{i,des}(k) \triangleq [\delta_0 \;\; \overline{m}_{i,0}\mathscr{E}_0(k)]^\top$, and $\sigma_i$ is an invariant set with respect to the system uncertainties.

The following assumption will be used throughout the paper.

**Assumption 4.3.1** *$f_i(\cdot), \forall i \in \mathscr{N}$ in the system equation* (4.11) *is Lipschitz in $\mathbb{X}_i$ with a constant $\kappa_i$.*

Next, we define the nominal unperturbed system of (4.11), which will be instrumental for the tube-MPC design, introduced later on in this Section

$$\bar{x}_i(k+1) = A_i\bar{x}_i(k) + B_i\bar{u}_i(k) + \gamma_i(k) \tag{4.14a}$$

$$\bar{y}_i(k) = C\bar{x}_i(k) \tag{4.14b}$$

where $\bar{x}_i(k) \triangleq [\bar{\delta}_i(k)\ \bar{\mathscr{E}}_i(k)]^\top$ is the nominal state, $\bar{u}_i(k) \triangleq [\bar{\zeta}_i(k)\ \bar{\mathscr{T}}_i(k)]^\top$ is the nominal control input and $\bar{y}_i(k)$ is the nominal output.

By applying the Luenberger observer, the state of the actual system (4.11) can be estimated by:

$$\begin{aligned} \hat{x}_i(k+1) &= A_i\hat{x}_i(k) + B_iu_i(k) + \gamma_i(k) + L_i(y_i(k) - \hat{y}_i(k)) \\ \hat{y}_i(k) &= C\hat{x}_i(k) \end{aligned} \tag{4.15}$$

where $L_i$ is the observer gain, designed individually for each vehicle, such that $A_i - L_iC$ is stable. Considering the state estimation error $\tilde{x}_i = x_i - \hat{x}_i$, its dynamics are governed by:

$$\tilde{x}_i(k+1) = (A_i - L_iC)\tilde{x}_i(k) + (d_i(k) - L_iw_i(k)) \tag{4.16}$$

In addition, the term $d_i(k) - L_iw_i(k)$ is bounded by a set $\tilde{\Omega}_i$, expressed as

$$\tilde{\Omega}_i \triangleq \mathbb{D}_i \oplus (-L_i\mathbb{W}_i) \tag{4.17}$$

Furthermore, the robust invariant set $\tilde{\mathbb{S}}_i$ of $\tilde{x}$ with respect to the process and measurement disturbances can be obtained by

$$\tilde{\mathbb{S}}_i = \oplus_{k=0}^{\infty}(A_i - L_iC)^k\tilde{\Omega}_i\,. \tag{4.18}$$

Consider $e_i(k) = \hat{x}_i(k) - \bar{x}_i(k)$ the mismatch between the observer state and the

nominal system. Then the control law is constructed by

$$u_i(k) = \bar{u}_i(k) + K_i e_i(k) \tag{4.19}$$

where $\bar{u}_i(k)$ is determined by solving a nominal MPC problem subject to (4.14) and tightened state and input constraints, defined later on in (4.21), and $K_i$ is the prespecified feedback control gain, which stabilize $A_i + B_i K_i$. By applying (4.19) to (4.15), we obtain

$$\hat{x}_i(k+1) = A\hat{x}_i(k) + B_i\bar{u}_i(k) + B_i K_i e_i(k) + \gamma_i(k) + L_i C\tilde{x}_i(k) + L_i w_i(k)$$

In virtue of the nominal system (4.14), the dynamics of the tracking error $e_i(k)$ is given by

$$e_i(k+1) = (A_i + B_i K_i)e_i(k) + (L_i C\tilde{x}_i(k) + L_i w_i(k))$$

where the uncertainties term $L_i C\tilde{x}_i(k) + L_i w_i(k)$ is confined by

$$\overline{\Omega}_i \triangleq L_i C\tilde{\mathbb{S}}_i \oplus L_i \mathbb{W}_i \,.$$

Similar to (4.18), the robust invariant set $\tilde{\mathbb{S}}_i$ of $e_i$ follows

$$\overline{\mathbb{S}}_i = \oplus_{k=0}^{\infty} (A_i + B_i K_i)^k \overline{\Omega}_i \tag{4.20}$$

According to [159, 174], to ensure the satisfaction of the original state and control constraints, $x_i(k) \in \mathbb{X}_i$ and $u_i(k) \in \mathbb{U}_i$, in the presence of the perturbations, tightened state and input constraints

$$\bar{x}_i \in \mathbb{X}_i \ominus (\tilde{\mathbb{S}}_i \oplus \overline{\mathbb{S}}_i), \qquad \bar{u}_i \in \mathbb{U}_i \ominus K_i \overline{\mathbb{S}}_i. \tag{4.21}$$

are enforced in place of the originals when solving the MPC problem (see (4.26) that will be introduced later in 4.3.2) In the following, for the sake of the brevity,

we let

$$\bar{\mathbb{X}}_i \triangleq \mathbb{X}_i \ominus (\tilde{\mathbb{S}}_i \oplus \overline{\mathbb{S}}_i), \qquad \bar{\mathbb{U}}_i \triangleq \mathbb{U}_i \ominus K_i \overline{\mathbb{S}}_i \tag{4.22}$$

### 4.3.2 Distributed Platoon Control Framework

Consider $N_p$ the prediction horizon for each local MPC. To introduce the DMPC framework, let us define $x_i^*(j|k) \triangleq [\delta_i^*(j|k)\ \mathscr{E}_i^*(j|k)]^\top$ and $u_i^*(j|k) \triangleq [\zeta_i^*(j|k)\ \mathscr{T}_i^*(j|k)]^\top$ the optimal state and input trajectory, respectively. The optimal trajectories are obtained by iteratively solving each local MPC problem (see $\mathscr{P}_i(k)$ defined in (4.26)). In addition, define $x_i^a(j|k) \triangleq [\delta_i^a(j|k)\ \mathscr{E}_i^a(j|k)]^\top$ and $u_i^a(j|k) \triangleq [\zeta_i^a(j|k)\ \mathscr{T}_i^a(j|k)]^\top$ respectively the assumed state and control trajectory, which are shared with the neighboring vehicle by the PF communication. Finally, consider $x_{i,des}(j|k) \triangleq [\delta_0\ \mathscr{E}_{i,des}(j|k)]^\top$ the desired state trajectory. Specifically, $\mathscr{E}_{i,des}(j|k)$ is set to as $\mathscr{E}_{i,des}(j|k) = \overline{m}_{i,i-1}\mathscr{E}_{i-1}^a(j|k)$. The $k$th step assumed trajectories $(x_i^a(:|k), u_i^a(:|k))$ are constructed by using the $(k-1)$th step optimal solution as follows:

$$u_i^a(j|k) = u_i^*(j+1|k-1),\ \forall j \in \{0,1,...,N_p-2\} \tag{4.23}$$

which yields

$$x_i^a(j|k) = x_i^*(j+1|k-1),\ \forall j \in \{0,1,...,N_p-1\} \tag{4.24}$$

Moreover, $u_i^a(N_p-1|k)$ is designed to render

$$x_i^a(N_p|k) = A_i x_i^a(N_p-1|k) + B_i u_i^a(N_p-1|k) + \gamma_i(N_p-1|k) = x_{i,des}(N_p|k). \tag{4.25}$$

The existence of such a feasible $u_i^a(N_p-1|k)$ is characterized by Assumption 4.4.2 given in Section 4.4.1.

Considering the control objectives defined in (4.13), we formulate the local

MPC problem $\mathscr{P}_i(k)$ for each vehicle $i \in \mathscr{N}$, at step $k$, as

$$\mathscr{P}_i(k):$$

$$\min_{\bar{u}_i} \; J_i(\bar{x}_i(:|k), \bar{u}_i(:|k), x_i^a(:|k), x_{i,des}(:|k))$$
$$= \sum_{j=0}^{N_p-1} l_i(\bar{x}_i(j|k), \bar{u}_i(j|k), x_i^a(j|k), x_{i,des}(j|k)) + \sum_{j=0}^{N_p-2} W_{i,5} |\bar{\zeta}_i(j|k) - f_i(\bar{\mathscr{E}}_i(j|k))| \tag{4.26a}$$

**s.t.** for $j = 0, 1, 2, \ldots, N_p - 1$

$$\bar{x}_i(j+1|k) = A_i \bar{x}_i(j|k) + B_i \bar{u}_i(j|k) + \gamma_i(j|k) \tag{4.26b}$$

$$\bar{x}_i(j|k) \in \breve{\mathbb{X}}_i(k) \tag{4.26c}$$

$$\bar{u}_i(j|k) \in \bar{\mathbb{U}}_i \tag{4.26d}$$

$$(\bar{x}_i(j|k), \bar{u}_i(j|k)) \in \breve{\mathbb{X}}_i(k) \times \bar{\mathbb{U}}_i \tag{4.26e}$$

$$\bar{x}_i(0|k) = y_i(k) \tag{4.26f}$$

$$\bar{x}_i(N_p|k) \in \mathbb{X}_{f,i} \tag{4.26g}$$

where (4.26a) is the cost function that will be specified later in (4.31). (4.26b) represents the nominal system introduced in (4.14), where the estimate $\hat{\bar{\mathscr{E}}}_{i-1}(j|k)$ in $\gamma_i(j|k)$ is defined by

$$\hat{\bar{\mathscr{E}}}_{i-1}(j|k) = \begin{cases} \mathscr{E}_{i-1}^a(N_p|k), & \text{if } x_{i-1}^a(N_p|k) = x_{i-1}^a(N_p|k-1), \\ \mathscr{E}_{i-1}^a(j|k), & \text{if } x_{i-1}^a(N_p|k) \neq x_{i-1}^a(N_p|k-1), \end{cases}$$
$$\forall j \in \{0, 1, ..., N_p\}. \tag{4.27}$$

As it can be noticed, $\hat{\bar{\mathscr{E}}}_{i-1}(j|k)$ is frozen at $\mathscr{E}_{i-1}^a(N_p|k)$ if the terminal step of the preceding vehicle's assumed trajectory (i.e., desired trajectory owing to (4.25)) remains the same for two consecutive steps, which usually happens when the leader vehicle reaches a steady state speed. Conversely, if $x_{i-1}^a(N_p|k) \neq x_{i-1}^a(N_p|k-1)$ (which implies $i-1$th vehicle's desired speed is time-varying), time-varying estimate $\hat{\bar{\mathscr{E}}}_{i-1}(j|k)$ is employed to enable the $i$th vehicle to keep up with the preceding vehicle.

The state and input constraints are taken into account by (4.26c), (4.26d) and (4.26e). Specifically, $\check{\mathbb{X}}_i(k)$ in (4.26c) is defined by $\check{\mathbb{X}}_i(k) = \bar{\mathbb{X}}_i \ominus \mathbb{H}_i(k)$, where $\mathbb{H}_i(k)$ is a set to further shrink the feasible set of the state to cope with the disturbances introduced at the initialization phase. It is designed as

$$\mathbb{H}_i(k) = (\bar{k} - k)\bar{\mathbb{H}}_i \tag{4.28}$$

where $\bar{\mathbb{H}}_i \triangleq \{(\varepsilon_1, \varepsilon_2) \in \mathbb{R}^2 \mid \varepsilon_1 \leq \bar{w}_i + \bar{d}_i,\ \varepsilon_2 \leq \bar{\varepsilon}\}$ with $\bar{\varepsilon} \triangleq (\bar{w}_i + \bar{d}_i) + N_p \kappa_i (\bar{w}_i + \bar{d}_i)\Delta s$. Moreover, $\bar{k}$ represents the total number of steps in the mission, where $\bar{k}\Delta s$ corresponds to the total travel distance. The feasible set of the control input, $\bar{\mathbb{U}}_i$, in (4.26d) is given in (4.22). In view of (4.9b), the coupled constraint (4.26e) represents

$$\check{\mathbb{X}}_i(k) \times \bar{\mathbb{U}}_i \triangleq \{(\bar{\mathscr{E}}, \bar{\zeta}_i) \mid \bar{\zeta}_i(j|k) \geq f_i(\bar{\mathscr{E}}_i(j|k))\} \tag{4.29}$$

The initial and terminal constraints of the MPC are specified by (4.26f) and (4.26g), respectively. In particular, the terminal set $\mathbb{X}_{f,i}$ is defined as

$$\begin{aligned}\mathbb{X}_{f,i} \triangleq \{\bar{x}_i(N_p|k) \,|\, &|\bar{\mathscr{E}}_i(N_p|k) - \overline{m}_{i,i-1}\mathscr{E}^a_{i-1}(N_p|k)| \leq \bar{w}_i + \bar{d}_i, \\ &|\bar{\delta}_i(N_p|k) - \delta_0| \leq \bar{\varepsilon}\}\end{aligned} \tag{4.30}$$

which ensures the state trajectory enters a terminal set and $x_{i,des}(N_p|k) \in \mathbb{X}_{f,i} \subseteq \bar{\mathbb{X}}_i \ominus \mathbb{H}_i$. The design of $\mathbb{H}_i(k)$ and $\mathbb{X}_{f,i}$ will be elaborated in Section 4.4.1. Finally, the stage cost function $l_i(\bar{x}_i(j|k), \bar{u}_i(j|k), x^a_i(j|k), x_{i,des}(j|k))$ is defined by

$$\begin{aligned}l_i \triangleq\ & W_{i,1}|\bar{\delta}_i(j|k) - \delta^a_i(j|k)| + W_{i,2}|\bar{\mathscr{E}}_i(j|k) - \mathscr{E}^a_i(j|k)| \\ & + W_{i,3}|\bar{\delta}_i(j|k) - \delta_0| + W_{i,4}|\bar{\mathscr{E}}_i(j|k)_i - \overline{m}_{i,i-1}\mathscr{E}^a_{i-1}(j|k)|\end{aligned} \tag{4.31}$$

where $W_{i,1}, W_{i,2} \in \mathbb{R}_{>0}$ penalize the differences between the optimal and assumed states and $W_{i,3}, W_{i,4} \in \mathbb{R}_{>0}$ are utilized to penalize the deviation of the optimal states from their desired trajectories. In addition, $W_{i,5} \in \mathbb{R}_{>0}$ in (4.26a) is used to ensure the tightness of the inequality condition in (4.29), thus the validity of the control solution, as will be discussed in Proposition 1.

Overall, the proposed convex and tube-based DMPC algorithm is summarized in Algorithm 3.

**Algorithm 3** The local convex and tube-based DMPC algorithm for vehicle $i \in \mathcal{N}$

**Offline:**

a) Find the observer and control gains $L_i$ and $K_i$;
b) Determine the tightened constraints (4.26c) and (4.26d), which are introduced in Section 4.3.1;
c) Select suitable weighting parameters $W_{i,1}, W_{i,2}, W_{i,3}, W_{i,4}, W_{i,5}$ and the prediction horizon $N_p$ for the $\mathscr{P}_i$ in line with (4.36) and (4.43);
e) Find an initial feasible assumed trajectory $x_i^a(:|0)$.

**Online:**

**while** $0 \leq k < \bar{k}$ **do**
  Measure the current state $y_i(k)$;
  Obtain the state estimate $\hat{x}_i(k)$ by (4.15);
  Set the initial condition (4.26f) of the MPC problem $\mathscr{P}_i(k)$ based on the measured values;
  Receive $x_{i-1}^a(:|k)$ and $u_{i-1}^a(:|k)$ from the preceding vehicle $i-1$;
  **if** $x_{i-1}^a(N_p|k) = x_{i-1}^a(N_p|k-1)$ **then**
    Solve $\mathscr{P}_i(k)$ with $\hat{\mathscr{E}}_{i-1}(:|k) = \mathscr{E}_{i-1}^a(N_p|k)$
  **else if** $x_{i-1}^a(N_p|k) \neq x_{i-1}^a(N_p|k-1)$ **then**
    Solve $\mathscr{P}_i(k)$ with $\hat{\mathscr{E}}_{i-1}(:|k) = \mathscr{E}_{i-1}^a(:|k)$
  **end if**
  Obtain $u_i^*(:|k)$ and $x_i^*(:|k)$;
  Construct $x_i^a(:|k)$ and $u_i^a(:|k)$ by (4.23)-(4.25) and send the assumed trajectories to vehicle $i+1$;
  Apply the control action $u_i(k) = u_i^*(0|k) + K_i e_i(k)$ with $e_i(k) = \hat{x}_i(k) - x_i^*(0|k)$ to the actual system (4.11);
  $k \leftarrow k+1$;
**end while**

**Remark 4.3.1** *From* (4.27)*, the construction of* $\hat{\mathscr{E}}_{i-1}$ *influences* $\bar{d}_i$ *(via* $\bar{d}_{2[1,1]}(k)$*) and therefore the design of the tube-based MPC. In particular,* $\bar{d}_{i[1,1]}(k)$ *denotes the maximum discrepancy between* $f_i\big(\mathscr{E}_{i-1}(k)\big)\Delta s$ *and* $f_i\big(\hat{\mathscr{E}}_{i-1}(k)\big)\Delta s$*, which is* $(\frac{1}{v_{\min}} - \frac{1}{v_{\max}})\frac{\Delta s}{\Delta t_{\max}}$*. For instance, considering the parameter choices given in Case study 1 of Simulation Section (see Table 4.1 and Table 4.2), the resulting upper bound of* $|d_{i[1,1]}(k)|$ *after normalization is 0.033.*

## 4.4 Theoretical Analysis

In this section, recursive feasibility and Lyapunov stability of Algorithm 3 are discussed, and rigorously proved under the case that the leading vehicle is driven at a constant speed $v_0(k) = \bar{v}_0, \forall k \geq k_1$.

### 4.4.1 Recursive Feasibility and Legitimate of Solutions

According to the PF communication graph, it can be shown that $x_{i,des}(N_p|k) = x^*_{i,des}$, $\forall k \geq k_1 + N$, and therefore only the first condition of (4.27) is employed. Note that the dependence of $x^*_{i,des}(k)$ on $k$ is dropped for clarity since $x^*_{i,des}(k)$ is constant for all $k \geq k_1 + N$. Following assumptions are needed to proceed with the analysis.

**Assumption 4.4.1** *All local MPC problems $\mathscr{P}_i(k), \forall i \in \mathscr{N}$ are feasible for $k \leq k_1 + N$.*

**Assumption 4.4.2** *The condition $\mathbb{X}_{f,i} \subseteq \Xi_i$ holds for all $k \geq k_1 + N$ with $\Xi_i$ the one-step predecessor state set, which can be steered to $x_{i,des}(N_p|k)$ by a feasible control action $u^a_i(N_p - 1|k)$ under* (4.26b)*:*

$$\Xi_i \triangleq \{\bar{x}(N_p - 1|k) \,|\, \exists \bar{u}_i(N_p - 1|k) \textit{ fulfills } (4.26\text{d}) \textit{ and } (4.26\text{e}) : \bar{x}(N_p|k) = x_{i,des}(N_p|k)\}.$$

As it can be noticed, the initial feasible assumption in Assumption 4.4.1 is commonly used in DMPC framework with unidirectional topologies [10, 105]. This can be addressed by a centralized optimization method or by a trial-and-error approach [175] in the distributed fashion, which have been extensively discussed in the literature. Furthermore, Assumption 4.4.2 characterizes the size of $\bar{\mathbb{U}}_i$ (in terms of the disturbance $\bar{d}_i, \bar{w}_i$) required to ensures that there exists a feasible $u^a_i(N_p - 1|k)$ so that (4.25) can be achieved. Since $\bar{d}_i$ is a $\mathscr{K}$ function with respect to the radius of the admissible velocity set $\mathscr{V}_{i-1}$ of $v_{i-1}$ (see 4.3.1), Assumption 4.4.2 can be validated for a given platoon system by gradually tightening the admissible velocity set $\mathscr{V}_i$ ($v_i \in \mathscr{V}_i, \forall i \in \{0\} \cup \mathscr{N}$) as $i \to 0$. In other words, ensuring that $\mathscr{V}_{i-1} \subset \mathscr{V}_i, \forall i \in \mathscr{N}$ leads to gradually enlarged admissible control (torque) sets as $i \to N$.

**Theorem 4.4.1** *Under Assumptions 4.3.1, 4.4.1 and 4.4.2, Algorithm 3 is recursively feasible for all followers.*

**Proof:** Suppose at any step $k > k_1 + N$, there is a solution $(x_i^*(:|k), u_i^*(:|k))$ for $\mathscr{P}_i(k)$ satisfying all constraints (4.26b)-(4.26g). In the following, to deal with the coupled state-control constraint (4.26e), the two control $\bar{u}_i(:|k+1) = [\bar{\zeta}_i(:|k+1)\ \bar{\mathscr{T}}_i(:|k+1)]^\top$ and two state $\bar{x}_i(:|k+1) = [\bar{\delta}_i(:|k+1)\ \bar{\mathscr{E}}_i(:|k+1)]^\top$ sequences will be analyzed separately. Consider a candidate torque sequence constructed by $\bar{\mathscr{T}}_i(:|k+1) = \mathscr{T}_i^a(:|k+1)$ for $\mathscr{P}_i(k+1)$. It is immediate to show that $\mathscr{T}_i^a(0:N_p-2|k+1)$ satisfies the constraint (4.26d), and according to Assumption 4.4.2, $\mathscr{T}_i^a(N_p-1|k+1)$ is also feasible. Due to the impact of the disturbances $w_i(k+1)$ and $d_i(k+1)$ introduced when $\bar{\mathscr{E}}_i(0|k+1)$ is initialized (see (4.26f)), the predicted state trajectory $\bar{\mathscr{E}}_i(:|k+1)$ produced by $\mathscr{T}_i^a(:|k+1)$ is different from the assumed state trajectory $\mathscr{E}_i^a(:|k+1)$. Let

$$\varepsilon_1(:|k+1) \triangleq \bar{\mathscr{E}}_i(:|k+1) - \mathscr{E}_i^a(:|k+1).$$

It is clear that

$$\varepsilon_1(j+1|k+1) = a_{i,2}\varepsilon_1(j|k+1), \forall j \in \{0,1,...,N_p-1\}$$

with $a_{i,2} = A_{i\,[2,2]}$, which in turn implies

$$\varepsilon_1(j+1|k+1) = a_{i,2}^{j+1}\varepsilon_1(0|k+1),\ j \in \{0,1,...,N_p-1\}$$

with $\varepsilon_1(0|k+1) = a_{i,2}w_i(k+1) + d_i(k+1)$. Due to the fact that $|a_{i,2}| < 1$, we have

$$\begin{aligned}|\varepsilon_1(j|k+1)| \le |\varepsilon_1(0|k+1)| &= |a_{i,2}w_i(k+1) + d_i(k+1)| \\ &\le \bar{w}_i + \bar{d}_i, \forall j \in \{0,1,...,N_p\}. \quad (4.32)\end{aligned}$$

Now, we construct

$$\bar{\zeta}_i(j|k+1) = f_i(\bar{\mathscr{O}}_i(j|k+1)), \forall j \in \{0,1,...,N_p-2\}$$

that follows the equality of (4.29) to ensure the legitimate of the candidate solution.

Thanks to Assumption 4.3.1, we have

$$\begin{aligned}|\bar{\zeta}_i(j|k+1) - \zeta_i^a(j|k+1)| &= |f_i(\bar{\mathscr{O}}_i(j|k+1)) - f_i(\mathscr{O}_i^a(j|k+1))| \\ &\leq \kappa_i|\bar{\mathscr{O}}_i(j|k+1) - \mathscr{O}_i^a(j|k+1))| \leq \kappa_i(\bar{w}_i + \bar{d}_i).\end{aligned}$$

Therefore, the equality condition in (4.29) holds for $\bar{\zeta}_i(0:N_p-2|k+1)$, while the feasibility of $\zeta_i^a(N_p-1|k+1)$ in terms of (4.26e) (without ensuring the tightness of (4.29)) is guaranteed by Assumption 4.4.2. Let

$$\varepsilon_2(:|k+1) \triangleq \bar{\delta}_i(:|k+1) - \delta_i^a(:|k+1).$$

Then, by following the same steps carried out for $\varepsilon_1(:|k+1)$, it can be shown that for all $j \in \{0,1,...,N_p-1\}$, it holds that

$$\varepsilon_2(j+1|k+1) = a_{i,1}\varepsilon_2(j|k+1) + (\bar{\zeta}_i(j|k+1) - \zeta_i^a(j|k+1))\Delta s.$$

As $a_{i,1} = A_{i[1,1]} = 1$, it holds that

$$\begin{aligned}|\varepsilon_2(j+1|k+1)| &\leq a_{i,1}^{j+1}(\bar{w}_i + \bar{d}_i) + \sum_{i=0}^{j} a_{i,1}^{i}\kappa_i(\bar{w}_i + \bar{d}_i)\Delta s \\ &= (\bar{w}_i + \bar{d}_i) + (j+1)\kappa_i(\bar{w}_i + \bar{d}_i)\Delta s \\ &\leq (\bar{w}_i + \bar{d}_i) + N_p\kappa_i(\bar{w}_i + \bar{d}_i)\Delta s\end{aligned} \tag{4.33}$$

In view of (4.32) and (4.33), provided that the $k$th step solution is inside the feasible region $\bar{\mathbb{X}}_i \ominus \mathbb{H}_i(k)$, $\bar{x}_i(:|k+1)$ must be bounded by the enlarged set $\bar{\mathbb{X}}_i \ominus \mathbb{H}_i(k+1)$ with $\mathbb{H}_i(k)$ defined in (4.28), as required by (4.26c). Moreover, considering (4.25), the terminal constraint (4.26g) of $\bar{x}_i(N_p|k+1)$ is also fulfilled. Therefore, the $(k+1)$

step solution (driven by $\mathscr{T}_i^a(:|k+1)$) is feasible.

The analysis can be applied to all steps $k > k_1 + N$. Hence, it can be concluded by induction that if Assumption 4.4.1 holds, the proposed algorithm is recursively feasible, and it applies to any vehicle $i \in \mathscr{N}$.

**Remark 4.4.1** *The enlarged set $\mathbb{H}_i$ (see (4.28)) parameterized by $\bar{k}$ may be too conservative in practice. To reduce the conservativeness, one may set $\mathbb{H}_i(k) = (z-k)\bar{\mathbb{H}}_i$ with $z = k+1, k+2 \ldots, \bar{k}-1$ and reset the algorithm when the set $\bar{\mathbb{X}}_i \ominus \mathbb{H}_i(k)$ can not be enlarged any more when $\mathbb{H}_i(k) = \emptyset$. The reset can be performed with reinitialized $\mathbb{H}_i(k) = (z-k)\bar{\mathbb{H}}_i$, $z > k$ from the vehicle where the infeasibility occurs towards the Nth vehicle in a sequential manner.*

Theorem 4.4.1 demonstrates the existence of a feasible and legitimate solution, except for the last step, where the tightness of (4.29) cannot be guaranteed. However, this does not affect the validity of the closed-loop control solution unless a valid MPC solution (with a guaranteed equality condition of (4.29)) cannot be found for consecutive $N_p$ steps. In such a case, a sequential reset of the DMPC algorithm will be invoked as with 4.4.1. Next, we show that the optimal solution of the finite-horizon optimization problem $\mathscr{P}_i(k)$ tends to find the equality condition of (4.29).

Given the $(k-1)$th step optimal solution $(x_i^*(:|k-1), u_i^*(:|k-1))$ of $\mathscr{P}_i(k-1)$ and the measurement $y_i(k)$ (which determines the initial condition of $\mathscr{P}_i(k)$), first consider a feasible solutions of $\mathscr{P}_i(k)$, denoted by $(\delta_i^c(:|k), \mathscr{E}_i^c(:|k), \zeta_i^c(:|k), \mathscr{T}_i^c(:|k))$ by which the equality condition $\zeta_i^c(j|k) = f_i(\mathscr{E}_i^c(j|k))$, $\forall j \in \{0,1,...,N_p-1\}$ in (4.29) holds. Then under the same $(x_i^*(:|k-1), u_i^*(:|k-1))$ and $y_i(k)$, it is possible to construct an alternative solution $\left(\breve{\delta}_i(:|k), \breve{\mathscr{E}}_i(:|k), \breve{\zeta}_i(:|k), \breve{\mathscr{T}}_i(:|k)\right)$ with $\breve{\delta}_i(0|k) = \delta_i^c(0|k)$, $\breve{\mathscr{T}}_i(:|k) = \mathscr{T}_i^c(:|k)$ and $\breve{\mathscr{E}}_i(:|k) = \mathscr{E}_i^c(:|k)$ whereas the tightness of (4.29) does not hold

$$\breve{\zeta}_i(j|k) = f_i(\breve{\mathscr{E}}_i(j|k)) + \Delta\zeta_i(j|k),\ \Delta\zeta_i(j|k) \in \mathbb{R}_{>0}$$

which implies

$$\Delta\zeta_i(j|k) = \breve{\zeta}_i(j|k) - \zeta_i^c(j|k),\ \forall j \in \{0,1,...,N_p-2\}. \tag{4.34}$$

In view of (4.11) and (4.34), the dynamics of $\delta_i$ in both scenarios follow

$$\delta_i^c(j+1|k) = \delta_i^c(j|k) + \Big(\zeta_i^c(j|k) - f_i\big(\hat{\mathscr{E}}_{i-1}\big)\Big)\Delta s \tag{4.35a}$$

$$\breve{\delta}_i(j+1|k) = \breve{\delta}_i(j|k) + \Big(\zeta_i^c(j|k) + \Delta\zeta_i(j|k) - f_i\big(\hat{\mathscr{E}}_{i-1}\big)\Big)\Delta s \tag{4.35b}$$

The main result is characterized by the following proposition.

**Proposition 1** *Given the two feasible solutions* $(\delta_i^c(:|k), \mathscr{E}_i^c(:|k), \zeta_i^c(:|k), \mathscr{T}_i^c(:|k))$ *and* $\big(\breve{\delta}_i(:|k), \breve{\mathscr{E}}_i(:|k), \breve{\zeta}_i(:|k), \breve{\mathscr{T}}_i(:|k)\big)$ *defined above, if the weights of the DMPC objective function* (4.31) *are chosen such that*

$$W_{i,5} \geq (N_p-1)\Delta s(W_{i,1} + W_{i,3}) \tag{4.36}$$

*the optimal solution of* $\mathscr{P}_i(k), \forall k \in \{0,1,...,\bar{k}\}$ *always finds* $(\delta_i^c(:|k), \mathscr{E}_i^c(:|k), \zeta_i^c(:|k), \mathscr{T}_i^c(:|k))$ *with guaranteed equality condition of* (4.29).

**Proof:** Let $J_i^c(k)$ and $\breve{J}_i(k)$ denote the cost in both solution cases. Their difference follows

$$\begin{aligned} J_i^c(k) - \breve{J}_i(k) = &\sum_{j=0}^{N_p-1} l_i\big(x_i^c(j|k), u_i^c(j|k), x_i^a(j|k), x_{i,des}(j|k)\big) \\ &+ \sum_{j=0}^{N_p-2} W_{i,5}|\zeta_i^c(j|k) - f_i(\mathscr{E}_i^c(j|k))| \\ &- \Big(\sum_{j=0}^{N_p-1} l_i\big(\breve{x}_i(j|k), \breve{u}_i(j|k), x_i^a(j|k), x_{i,des}(j|k)\big) \\ &+ \sum_{j=0}^{N_p-2} W_{i,5}|\breve{\zeta}_i(j|k) - f_i(\breve{\mathscr{E}}_i(j|k))|\Big) \end{aligned} \tag{4.37}$$

After some rearrangements, we obtain

$$\begin{aligned} J_i^c(k) - \breve{J}_i(k) = \sum_{j=0}^{N_p-1} \Big( & W_{i,1}\big(|\delta_i^c(j|k) - \delta_i^a(j|k)| - |\breve{\delta}_i(j|k) \\ & - \delta_i^a(j|k)|\big) + W_{i,3}\big(|\delta_i^c(j|k) - \delta_0| - |\breve{\delta}_i(j|k) - \delta_0|\big)\Big) \\ & - \sum_{j=0}^{N_p-2} W_{i,5}\Delta\zeta_i(j|k) \end{aligned} \tag{4.38}$$

where the assumed and desired trajectories are identical in both scenarios as they are predefined based on the $(k-1)$th step solution. By the triangle inequality and the identity $\breve{\delta}_i(0|k) = \delta_i^c(0|k)$, it holds that

$$\begin{aligned} J_i^c(k) - \breve{J}_i(k) \leq \sum_{j=1}^{N_p-1} \Big( & W_{i,1}\big(|\breve{\delta}_i(j|k) - \delta_i^c(j|k)|\big) \\ & + W_{i,3}\big(|\breve{\delta}_i(j|k) - \delta_i^c(j|k)|\big)\Big) - \sum_{j=0}^{N_p-2} W_{i,5}\Delta\zeta_i(j|k) \end{aligned} \tag{4.39}$$

By subtracting (4.35a) from (4.35b), we obtain

$$\begin{aligned} & \breve{\delta}_i(j+1|k) - \delta_i^c(j+1|k) \\ & \qquad = \big(\breve{\delta}_i(j|k) - \delta_i^c(j|k)\big) + \Delta\zeta_i(j|k)\Delta s \end{aligned} \tag{4.40}$$

which, by induction, leads to

$$\breve{\delta}_i(j+1|k) - \delta_i^c(j+1|k) = \sum_{n=0}^{j} \Delta\zeta_i(n|k)\Delta s. \tag{4.41}$$

Substituting (4.41) into (4.39), it yields

$$\begin{aligned} J_i^c(k) - \breve{J}_i(k) \leq & \sum_{j=1}^{N_p-1} \Big( W_{i,1} \sum_{n=0}^{j-1} \Delta\zeta_i(n|k)\Delta s \\ & + W_{i,3} \sum_{n=0}^{j-1} \Delta\zeta_i(n|k)\Delta s \Big) - W_{i,5} \sum_{j=0}^{N_p-2} \Delta\zeta_i(j|k) \\ = & \Delta s(W_{i,1}+W_{i,3}) \sum_{j=1}^{N_p-1} \sum_{n=0}^{j-1} \Delta\zeta_i(n|k) - W_{i,5} \sum_{j=0}^{N_p-2} \Delta\zeta_i(j|k) \\ \leq & (N_p-1)\Delta s(W_{i,1}+W_{i,3}) \sum_{j=0}^{N_p-2} \Delta\zeta_i(j|k) - W_{i,5} \sum_{j=0}^{N_p-2} \Delta\zeta_i(j|k) \end{aligned} \tag{4.42}$$

Given the condition (4.36), (4.42) further implies that $J_i^c(k) - \breve{J}_i(k) \leq 0$, thus ending the proof.

**Remark 4.4.2** *Note that 1 does not ensure a legitimate solution to be found. The proposed algorithm may still find a solution where the equality condition of* (4.29) *is not satisfied within a finite horizon due to the non-strict convexity. In such a case, a legitimate solution (except the last step) can be constructed a posteriori by following the analysis given in 4.4.1.*

### 4.4.2 Robustness Analysis

Based on Theorem 4.4.1, this subsection will focus on the Lyapunov stability of the proposed DMPC scheme.

**Theorem 4.4.2** *Under Assumptions 4.3.1, 4.4.1 and 4.4.2, given the Algorithm 3 for $\mathscr{P}_i(k)$, if the weighting parameters are designed such that*

$$W_{i,2} \geq W_{i+1,4}\overline{m}_{i+1,i}, \tag{4.43}$$

*the tracking error $x_i(k) - x_{i,des}^*$ of the perturbed system* (4.11) *is ISS with respect to the disturbances $d_i(k)$ and $w_i(k)$.*

**Proof:** Without considering the uncertainties $d_i(k)$ and $w_i(k)$, the terminal constraint (4.26g) of $\mathscr{P}_i(k)$ turns out to $\bar{x}_i(N_p|k) = x_{i,des}(N_p|k)$, which ensures

$x_i^*(N_p|k) = x_{i,des}^*, \forall k \geq k_1 + N$, $i \in \mathscr{N}$. Given $u_i^a(:|k+1)$ and $x_i^a(:|k+1)$ constructed by (4.23) - (4.25), it is straightforward to show they are feasible for $\mathscr{P}_i(k+1)$. In particular, (4.25) is achieved by employing

$$\begin{aligned}
&\mathscr{T}_i^a(N_p-1|k+1) = \frac{r_i}{\eta_{t,i}}\left(\frac{2C_{d,i}}{m_i}(\mathscr{E}_i^a(N_p-1|k+1) + m_i g C_{s,i}\right) \\
&\zeta_i^a(N_p-1|k+1) = f_i(\mathscr{E}_i^a(N_p-1|k+1))
\end{aligned}$$

which yields $x_i^a(N_p|k+1) = x_i^a(N_p-1|k+1) = x_i^*(N_p|k) = x_{i,des}^*$. From 4.4.1 and 4.4.2, $\zeta_i^a(j|k+1) = f_i(\mathscr{E}_i^a(j|k+1))$ holds for all $j \in \{0,1,...,N_p-2\}$. By substituting the optimal solution $(x_i^*(:|k+1), u_i^*(:|k+1))$, the corresponding cost function $J_i^*(k+1)$ can be rewritten as

$$\begin{aligned}
J_i^*(k+1) = &\sum_{j=0}^{N_p-1}\Big(W_{i,1}|\delta_i^*(j|k+1) - \delta_i^a(j|k+1)| \\
&+W_{i,2}|\mathscr{E}_i^*(j|k+1) - \mathscr{E}_i^a(j|k+1)| + W_{i,3}|\delta_i^*(j|k+1) - \delta_0| \\
&+W_{i,4}|\mathscr{E}_i^*(j|k+1) - \overline{m}_{i,i-1}\mathscr{E}_{i-1}^a(j|k+1)|\Big) \\
\leq &\sum_{j=0}^{N_p-1}\Big(W_{i,1}|\delta_i^a(j|k+1) - \delta_i^a(j|k+1)| \\
&+W_{i,2}|\mathscr{E}_i^a(j|k+1) - \mathscr{E}_i^a(j|k+1)| + W_{i,3}|\delta_i^a(j|k+1) - \delta_0| \\
&+W_{i,4}|\mathscr{E}_i^a(j|k+1) - \overline{m}_{i,i-1}\mathscr{E}_{i-1}^a(j|k+1)|\Big)
\end{aligned} \tag{4.44}$$

which can be reduced to

$$\begin{aligned}
J_i^*(k+1) \leq \sum_{j=0}^{N_p-1}\Big(&W_{i,3}|\delta_i^a(j|k+1) - \delta_0| \\
&+ W_{i,4}|\mathscr{E}_i^a(j|k+1) - \overline{m}_{i,i-1}\mathscr{E}_{i-1}^a(j|k+1)|\Big)
\end{aligned} \tag{4.45}$$

For the sake of further analysis, let us rewrite (4.45) as

$$\begin{aligned} J_i^*(k+1) &\leq \sum_{j=1}^{N_p} \Big( W_{i,3}|\delta_i^*(j|k) - \delta_0| \\ &\quad + W_{i,4}|\mathscr{E}_i^*(j|k) - \overline{m}_{i,i-1}\mathscr{E}_{i-1}^*(j|k)| \Big) \\ &= \sum_{j=1}^{N_p-1} \Big( W_{i,3}|\delta_i^*(j|k) - \delta_0| \\ &\quad + W_{i,4}|\mathscr{E}_i^*(j|k) - \overline{m}_{i,i-1}\mathscr{E}_{i-1}^*(j|k)| \Big) \end{aligned} \tag{4.46}$$

Subtracting $J_i^*(k)$ from $J_i^*(k+1)$,

$$\begin{aligned} &J_i^*(k+1) - J_i^*(k) \leq \\ &- \Big( W_{i,1}|\delta_i^*(0|k) - \delta_i^a(0|k)| + W_{i,2}|\mathscr{E}_i^*(0|k) - \mathscr{E}_i^a(0|k)| \\ &+ W_{i,3}|\delta_i^*(0|k) - \delta_0| + W_{i,4}|\mathscr{E}_i^*(0|k) - \overline{m}_{i,i-1}\mathscr{E}_{i-1}^a(0|k)| \Big) \\ &+ \sum_{j=1}^{N_p-1} \Big( W_{i,3}|\delta_i^*(j|k) - \delta_0| + W_{i,4}|\mathscr{E}_i^*(j|k) - \overline{m}_{i,i-1}\mathscr{E}_{i-1}^*(j|k)| \Big) \\ &- \sum_{j=1}^{N_p-1} \Big( W_{i,1}|\delta_i^*(j|k) - \delta_i^a(j|k)| + W_{i,2}|\mathscr{E}_i^*(j|k) - \mathscr{E}_i^a(j|k)| \\ &\quad + W_{i,3}|\delta_i^*(j|k) - \delta_0| + W_{i,4}|\mathscr{E}_i^*(j|k) - \overline{m}_{i,i-1}\mathscr{E}_{i-1}^a(j|k)| \Big) \end{aligned} \tag{4.47}$$

By applying the triangle inequality, (4.47) can be reduced to

$$\begin{aligned} &J_i^*(k+1) - J_i^*(k) \leq \\ &- \Big( W_{i,1}|\delta_i^*(0|k) - \delta_i^a(0|k)| + W_{i,2}|\mathscr{E}_i^*(0|k) - \mathscr{E}_i^a(0|k)| \\ &+ W_{i,3}|\delta_i^*(0|k) - \delta_0| + W_{i,4}|\mathscr{E}_i^*(0|k) - \overline{m}_{i,i-1}\mathscr{E}_{i-1}^a(0|k)| \Big) \\ &- \sum_{j=1}^{N_p-1} \Big( W_{i,1}|\delta_i^*(j|k) - \delta_i^a(j|k)| + W_{i,2}|\mathscr{E}_i^*(j|k) - \mathscr{E}_i^a(j|k)| \\ &\quad - W_{i,4}\overline{m}_{i,i-1}|\mathscr{E}_{i-1}^*(j|k) - \mathscr{E}_{i-1}^a(j|k)| \Big) \end{aligned} \tag{4.48}$$

Let us consider the sum of all local cost functions $J_i^*(k), \forall i \in \mathscr{N}$ as a candidate

Lyapunov function: $J_\Sigma^*(k) = \sum_{i=1}^N J_i^*(k)$ In view of (4.48), it can be shown that

$$\begin{aligned}
&J_\Sigma^*(k+1) - J_\Sigma^*(k) = \sum_{i=1}^{N} \Big( J_i^*(k+1) - J_i^*(k) \Big) \\
&\leq -\sum_{i=1}^{N} \Big( W_{i,1} |\delta_i^*(0|k) - \delta_i^a(0|k)| + W_{i,2} |\mathscr{E}_i^*(0|k) - \mathscr{E}_i^a(0|k)| \\
&+ W_{i,3} |\delta_i^*(0|k) - \delta_0| + W_{i,4} |\mathscr{E}_i^*(0|k) - \overline{m}_{i,i-1} \mathscr{E}_{i-1}^a(0|k)| \Big) \\
&- \sum_{i=1}^{N} \sum_{j=1}^{N_p-1} \Big( W_{i,1} |\delta_i^*(j|k) - \delta_i^a(j|k)| + W_{i,2} |\mathscr{E}_i^*(j|k) - \mathscr{E}_i^a(j|k)| \\
&- W_{i,4} \overline{m}_{i,i-1} |\mathscr{E}_{i-1}^*(j|k) - \mathscr{E}_{i-1}^a(j|k)| \Big)
\end{aligned} \tag{4.49}$$

Due to the fact that $W_{1,4}\overline{m}_{1,0}|\mathscr{E}_0^*(j|k) - \mathscr{E}_0^a(j|k)| = 0$, we have

$$\begin{aligned}
&J_\Sigma^*(k+1) - J_\Sigma^*(k) \\
&\leq -\sum_{i=1}^{N} \Big( W_{i,1} |\delta_i^*(0|k) - \delta_i^a(0|k)| + W_{i,2} |\mathscr{E}_i^*(0|k) - \mathscr{E}_i^a(0|k)| \\
&+ W_{i,3} |\delta_i^*(0|k) - \delta_0| + W_{i,4} |\mathscr{E}_i^*(0|k) - \overline{m}_{i,i-1} \mathscr{E}_{i-1}^a(0|k)| \Big) \\
&- \sum_{i=1}^{N} \sum_{j=1}^{N_p-1} W_{i,1} |\delta_i^*(j|k) - \delta_i^a(j|k)| - \sum_{j=1}^{N_p} \phi_{N,2} |\mathscr{E}_N^*(j|k) - \mathscr{E}_N^a(j|k)| \\
&- \sum_{i=1}^{N-1} \sum_{j=1}^{N_p-1} (W_{i,2} - W_{i,4}\overline{m}_{i,i-1}) |\mathscr{E}_i^*(j|k) - \mathscr{E}_i^a(j|k)|
\end{aligned} \tag{4.50}$$

According to (4.43), $J_\Sigma^*(k+1) - J_\Sigma^*(k) \leq 0$, which further implies the asymptotic convergence of tracking error of each vehicle $\bar{x}_i(k) - x_{i,des}(k), \forall i \in \mathscr{N}$. As the leader information is accessible to Vehicle 1, that is $x_{1,des} = [\delta_0 \ \overline{m}_{1,0}\mathscr{E}_0(k)]^\top$, it further implies that

$$\bar{x}_i(k) - x_{i,des}^* \to 0, k \to \infty, \ \forall i \in \mathscr{N}.$$

As $x_i(k) - \bar{x}_i(k) = \tilde{x}_i(k) + e_i(k)$ and $\tilde{x}_i(k)$ and $e_i(k)$ are ISS (see (4.16)-(4.20)), it is immediate to show that the tracking error $x_i(k) - x_{i,des}^*$ in the presence of disturbances and measurement noise is also ISS and it will converge to a robust invariable set $\tilde{\mathbb{S}}_i \oplus \overline{\mathbb{S}}_i$.

**Remark 4.4.3** *The proposed method is based on unidirectional PF topology, which demands less communication compared to other topologies, such as PLF, two predecessor-leader following (TPLF) topologies and other bidirectional counterparts. The proposed control solution can be extended to cope with those graphs [10, 176]. If the leader information is immediately available to all followers (e.g., PLF and TPLF), it is usually more straightforward to design a DMPC algorithm by replacing the desired state of the preceding vehicle* $\overline{m}_{i,i-1}\mathscr{E}^a_{i-1}(j|k)$ *in the local MPC problem* (4.26) *with the state* $\overline{m}_{i,0}\mathscr{E}_0$ *of the leading vehicle.*

## 4.5 Simulation

Two case studies are carried out in this section. In the first case study, a numerical example will first be investigated to show the effectiveness of the proposed algorithm, and then the significance of tube-based DMPC in dealing with system uncertainties by comparing it with the nominal DMPC algorithm. Finally, the proposed method is benchmarked against an existing nominal DMPC-based platooning method [10] in terms of computational efficiency. Case study 2 focuses on a more realistic scenario, where the leader is requested to follow an experimental speed profile. The proposed method demonstrates its ability to maintain platoon formation in this scenario, highlighting its applicability to more practical time-varying velocity scenarios.

In both examples, we consider a vehicle platoon that contains one leading vehicle and four following vehicles. Each individual vehicle exchanges information with its neighbors through a PF communication topology. In Table 4.1, the parameters of platoon vehicles are given, which reflect the heterogeneity entailed in vehicle mass $m_i$, air drag coefficient $C_{d,i}$, wheel radius $r_i$ and the driving/braking torque limits $T_{i,\min}$, $T_{i,\max}$. Other common parameters of the vehicle and the DMPC algorithm are included in Table 4.2. Note that a constant tyre rolling resistance coefficient, $C_{f_i}$, is employed as a simple example. This tube-based DMPC problem is solved by Yalmip [177] with the convex solver Mosek [178] in Matlab environment. The specifications of the PC are Intel Core i5 2.3GHz CPU with 8GB of RAM.

Table 4.1: Heterogeneous vehicle parameters

| Vehicle Index | $m_i$ [kg] | $C_{d,i}$ [$\mathrm{N \cdot s^2 \cdot m^{-2}}$] | $r_i$ [m] | $T_{i,\min}$ [$\mathrm{N \cdot m}$] | $T_{i,\max}$ [$\mathrm{N \cdot m}$] |
|---|---|---|---|---|---|
| 0 | 1035.7 | 0.35 | 0.30 | -350 | 350 |
| 1 | 1178.7 | 0.37 | 0.33 | -410 | 410 |
| 2 | 1257.6 | 0.37 | 0.33 | -450 | 450 |
| 3 | 1349.1 | 0.39 | 0.35 | -480 | 480 |
| 4 | 1434.0 | 0.41 | 0.38 | -510 | 510 |

Table 4.2: Rest of the parameters

| Description | Symbols | Values |
|---|---|---|
| Tyre rolling resistance coefficient | $C_{f_i}$ | 0.01 |
| Final drive ratio | $\eta_{t,i}$ | 3 |
| Gravity constant | g | 9.8 N/kg |
| Predictive Horizon Length | $N_p$ | 20 |
| Sampling distance interval | $\Delta s$ | 2 m |
| Desired time headway | $\delta_0$ | 1 s |
| Minimum time headway | $\Delta t_{\min}$ | 0.5s |
| Maximum time headway | $\Delta t_{\max}$ | 1.5s |

### 4.5.1 Step Function-type Leader Speed

Consider the velocity trajectory of the leading vehicle, as shown in Fig. 4.2. Assuming the speed limits are set to $v_{\min} = 20$ m/s and $v_{\max} = 40$ m/s. In addition, the process and measurement disturbances added to the dynamic equations of all followers are subject to $|d_i| \leq 0.035$ and $|w_i| \leq 0.02$, $\forall i \in \mathscr{N}$. Then, the uncertainty bounds $\bar{d}_i = 0.035$ and $\bar{w}_i = 0.02, \forall i \in \mathscr{N}$ are exploited for the design of the tube-based DMPC. Finally, the platoon is initialized by the conditions given in Table 4.3.

The results are shown in Figs. 4.2-4.4, which verify the effectiveness of the proposed control solution. More specifically, the velocity profiles and the resulting tracking error signals are shown in Fig. 4.2, demonstrated in the time domain for illustrative purposes. Since our control objective (4.13) is to maintain a constant time headway in the spatial domain, the resulting plots differ from other time domain control methods [10, 110] after spatial domain to time domain transformation. The simulation shows that the control signals of all follower vehicles exhibit similar

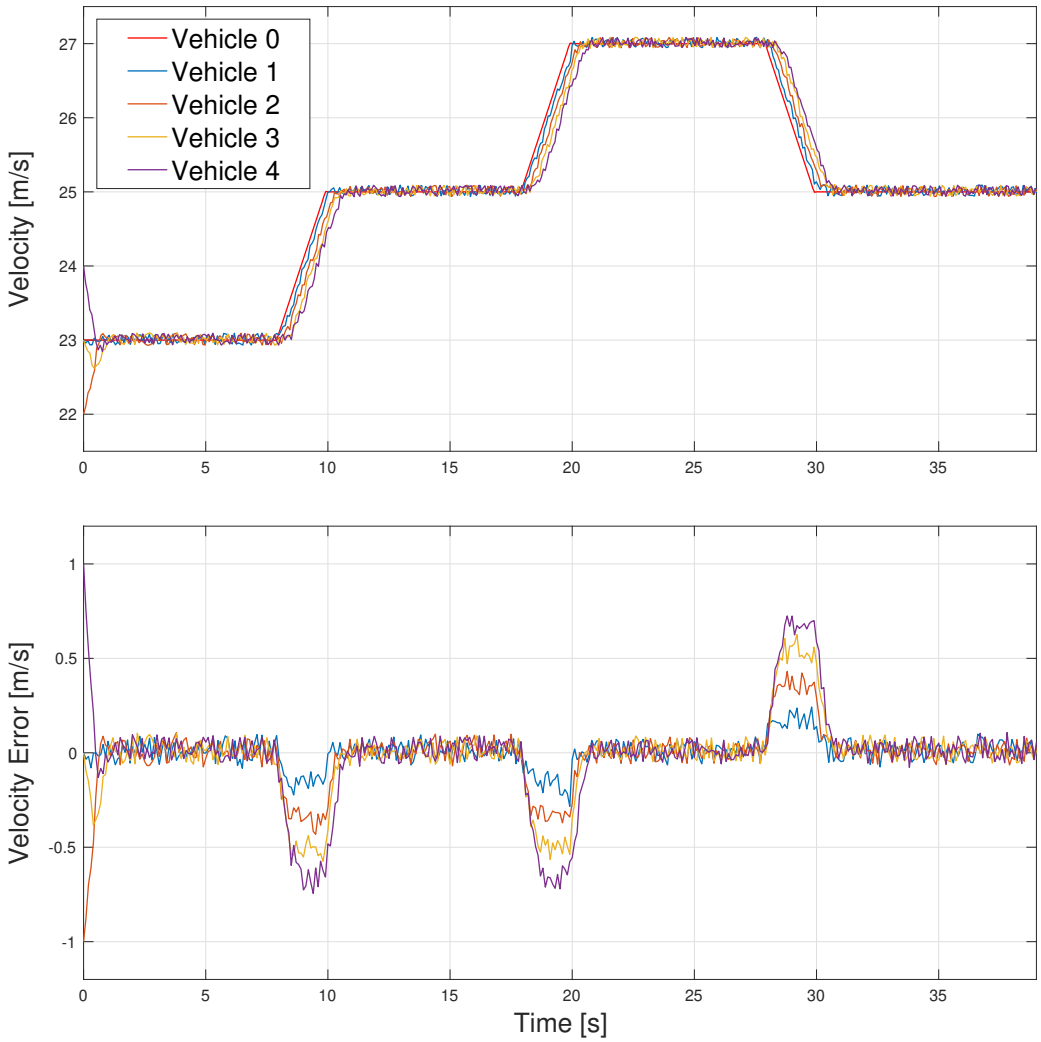


Figure 4.2: Top: The velocity performance of all vehicles. Bottom: The velocity tracking performance of all followers.

behavior, and therefore for clarity of the figure, only the input torque and the tube of Vehicle 1 are presented in Figs. 4.3. The chattering behavior primarily results from the uncertainties and may be attenuated by including the dynamics of the torque in the vehicle system model (4.11). Finally, it can be observed from Fig. 4.4 that the time headway tracking errors are robustly bounded around the desired values (with no validation against the safety limits) in the presence of the uncertainties.

Then, the proposed tube-based DMPC algorithm is compared with the nominal DMPC in the form of (4.26) but without the tightening of the feasibility sets (4.26c) (4.26d) and the terminal constraint (4.26g). From Fig. 4.5, it can be observed that

Table 4.3: Vehicle initial conditions in Case study 1

| Vehicle Index | Initial time $t_i(0)$ [s] | Initial Time Headway $\Delta t_i(0)$ [s] | Initial speed $v_i(0)$ [m/s] |
|---|---|---|---|
| 0 | 0 | - | 23 |
| 1 | 1.1 | 1.1 | 23 |
| 2 | 2 | 0.9 | 22 |
| 3 | 3.1 | 1.1 | 23 |
| 4 | 4 | 0.9 | 24 |

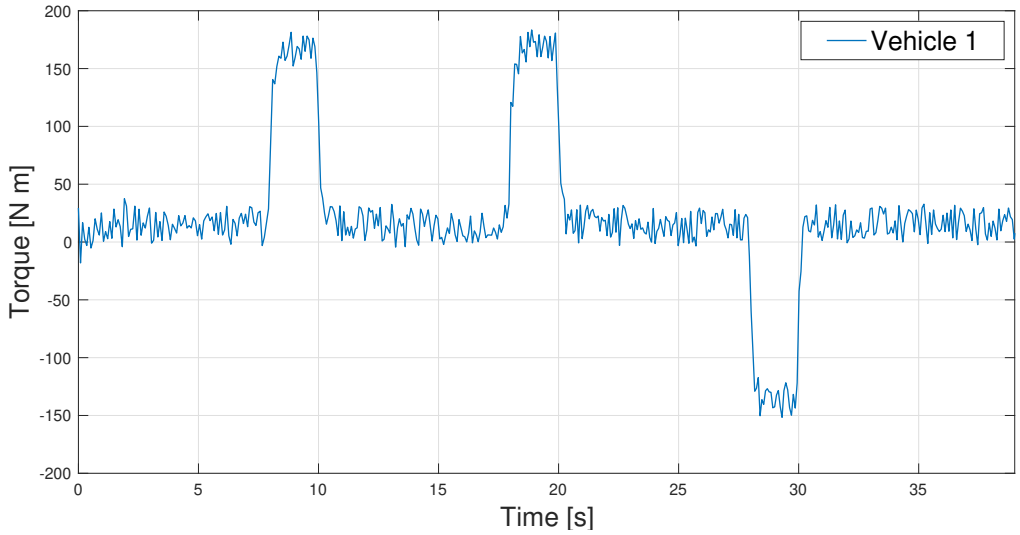


Figure 4.3: The input torque of Vehicle 1 in the platoon.

under the same simulation condition shown in Figs. 4.2 to 4.4, the time headway trajectory of the Vehicle 4 violates the state constraint at the position $s = 342$m, which may cause rear-end collisions in practice. It is noteworthy that the tightening of the feasibility entailed in the tube-based MPC inevitably introduces conservativeness, and may eventually become infeasible when the bound of uncertainty increases. In this context, we also take Vehicle 4 as an example to study the maximum uncertainty that can be tolerant. It is found that the proposed algorithm can tolerate normalized uncertainties up to $\bar{d}_i = 0.07$ or $\bar{w}_i = 0.07$, which corresponds to a velocity uncertainty of $\pm 2.8$ m/s and a distance headway uncertainty of $\pm 8.4$ m after converting to time domain.

Further simulation is performed to show the computational efficiency of the proposed convex and robust DMPC as compared to [10], which proposes a non-

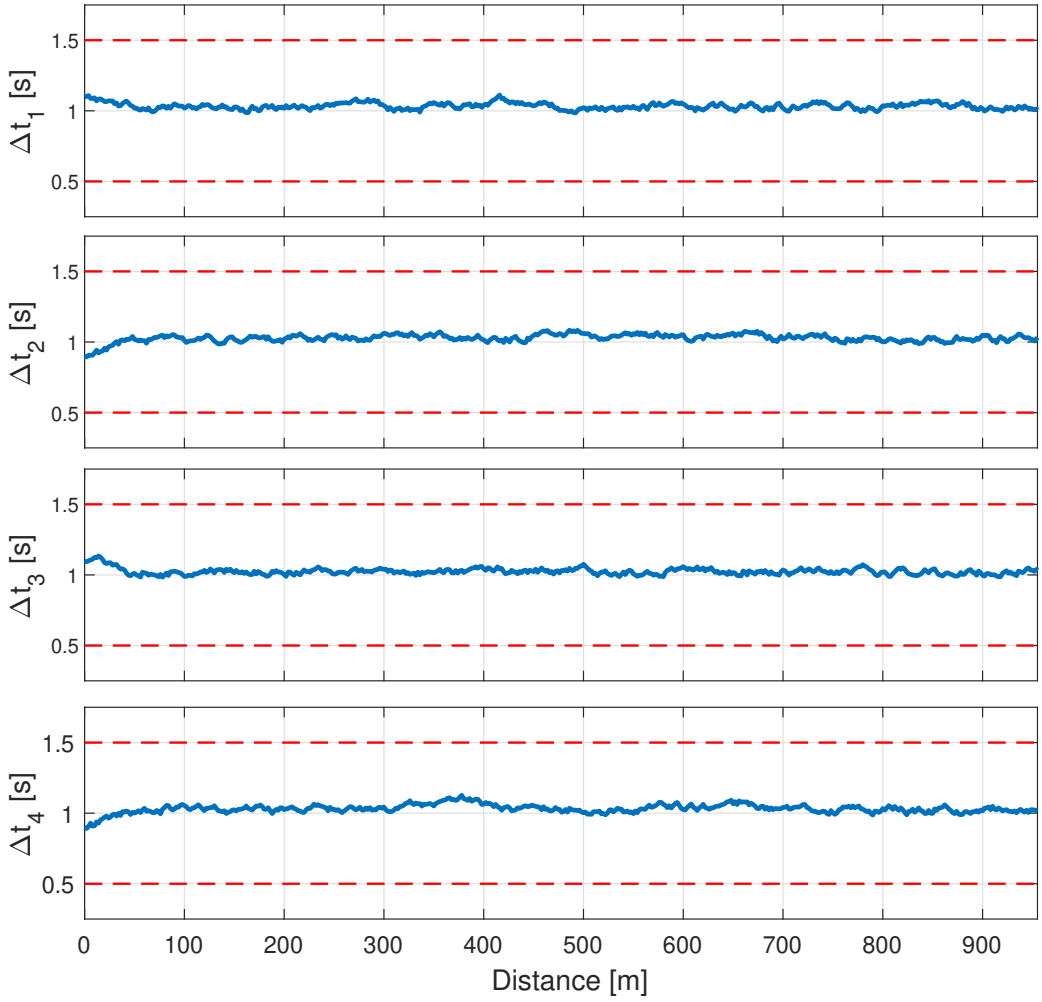


Figure 4.4: The time headway profiles of all followers.

convex DMPC algorithm. In order to conduct a fair comparison, we set identical parameters from Table 4.1 and Table 4.2. Additionally, the same cost function and weighting coefficients utilized in [10] are employed. The computational efficiency of the proposed method is evaluated in Fig. 4.6 by comparing to a traditional non-linear DMPC-based method [10] that is solved by IPOPT. As it can be seen, the individual DMPC average running time of each step is $8.5 \times 10^{-3}$ s. Considering the distance step size and $v_{\max} = 40$ m/s, the minimum time duration over a distance step $\Delta s$ is 0.05 s, which is greater than the computation time and therefore reflects the real-time applicability of the proposed algorithm. In contrast, when the non-convex DMPC algorithm is implemented, the average time consumption of all

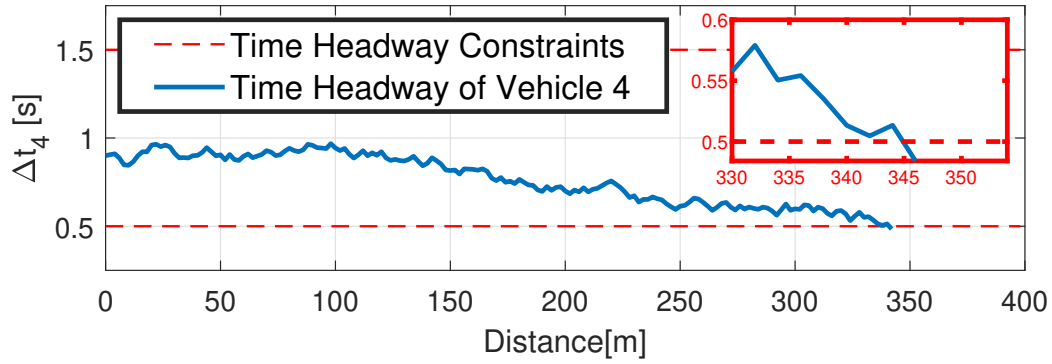


Figure 4.5: The time headway of Vehicle 4 obtained by a nominal MPC.

vehicles is above 0.4 s, considerably more time-consuming compared to the proposed method (approximately 50 times slower on average). The results show the merit of the convex modeling framework.

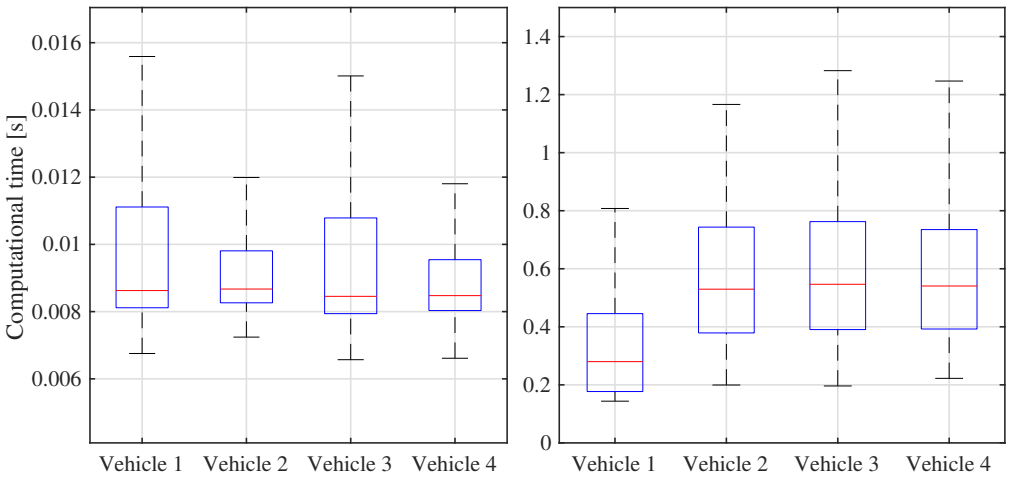


Figure 4.6: Left: Computation time of the proposed convex and robust DMPC algorithm. Right: Computation time of the nonlinear DMPC algorithm in [10].

### 4.5.2 Time-varying Leader Speed

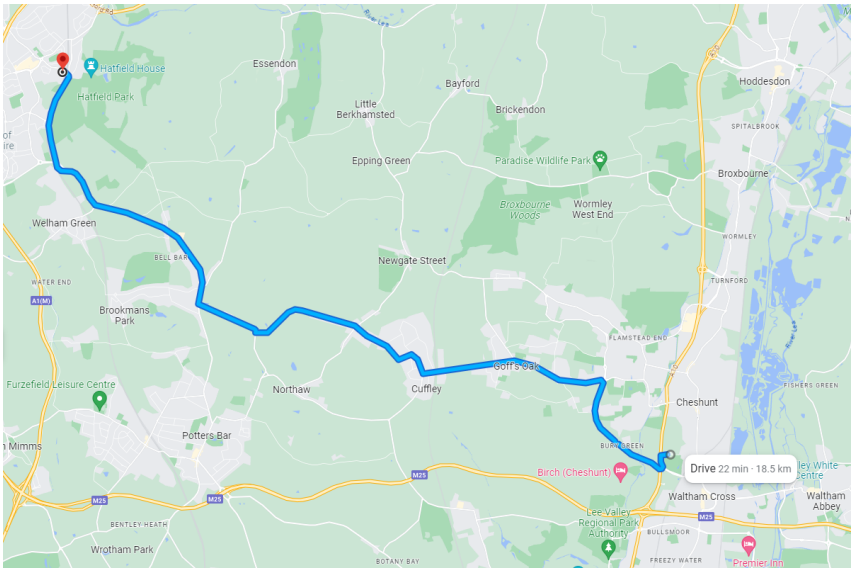


Figure 4.7: A 18.5km rural route in the UK.

In this subsection, we further examine the performance of the proposed method under the condition of continuously changing leader speed, which is taken from an experimental speed profile collected on a rural route in the UK (18.5 km in total, see Fig. 4.7). The road slope angle $\theta_i(s)$ is collected from Google Maps. The initial conditions of all vehicles are set uniformly as $\Delta t_i(0) = 1$ s and $v_i(0) = 0.91$ m/s for all $i \in \mathcal{N}$.

The velocity tracking performance is illustrated in Fig. 4.8. The proposed algorithm exhibits highly accurate tracking performance with a maximum error of $\pm 4.7$ m/s throughout the mission. As an example, the torque of Vehicle 1 is plotted in Fig. 4.9. Similar to Case Study 1, the profile remains noisy despite the respect of the control constraints. Furthermore, the time headway tracking performance of followers is shown in Fig. 4.10. Despite the increased complexity of the realistic driving cycle compared to the reference speed profile in Case Study 1, all followers can still maintain their time headway within the safe region with minimal tracking error attributed to system uncertainties.

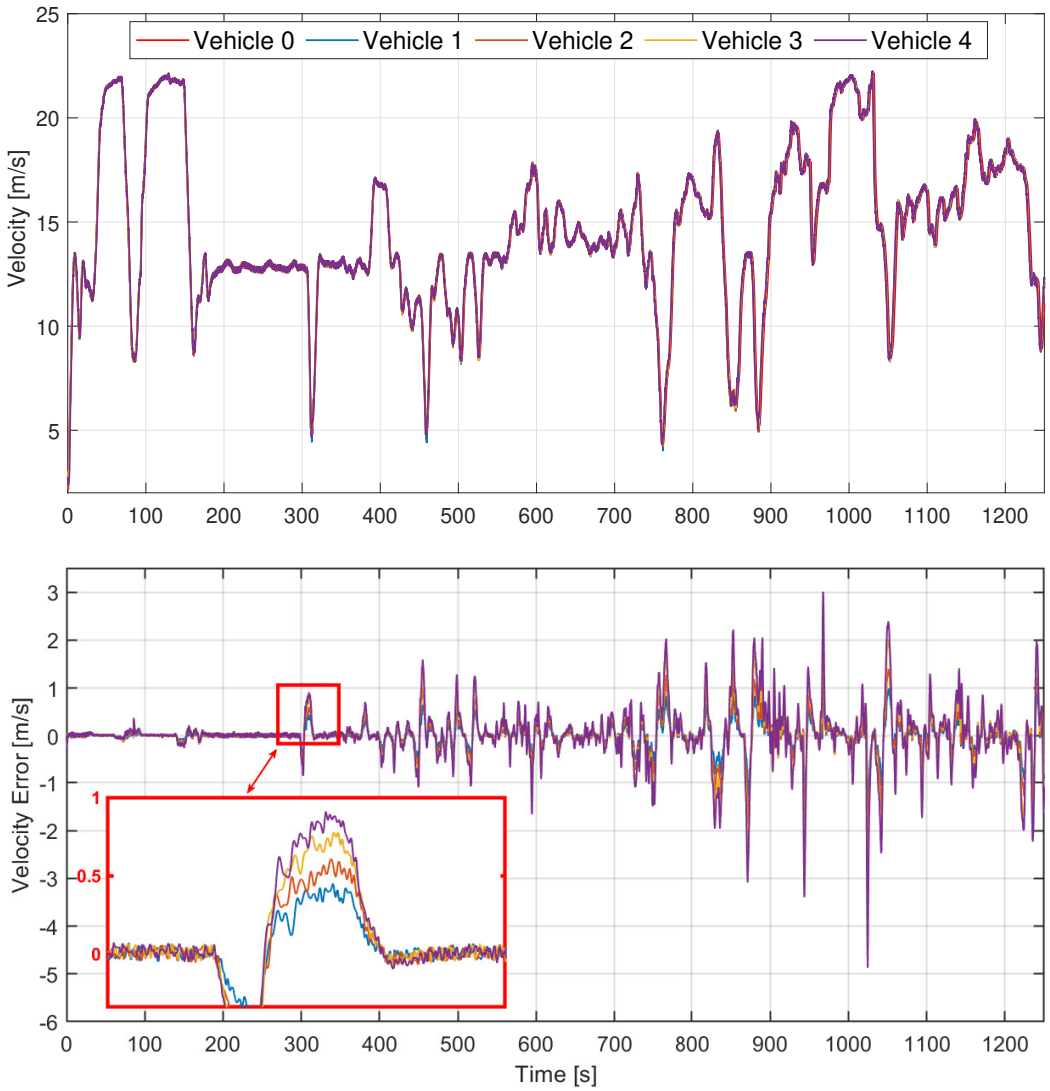


Figure 4.8: Top: The velocity performance of all vehicles during rural driving cycles. Bottom: The velocity tracking performance of all followers during the experimental driving profile.

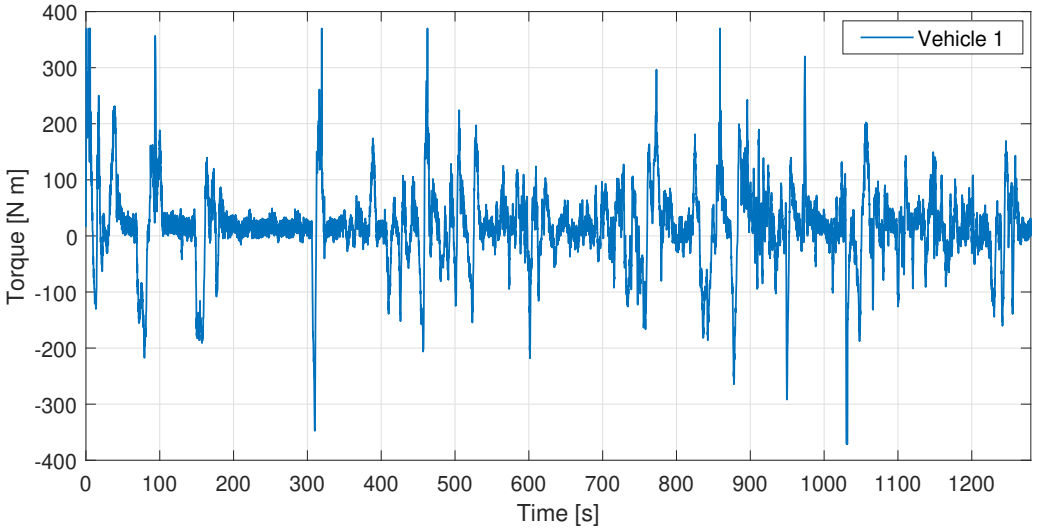


Figure 4.9: The input torque of Vehicle 1 during the experimental driving profile.

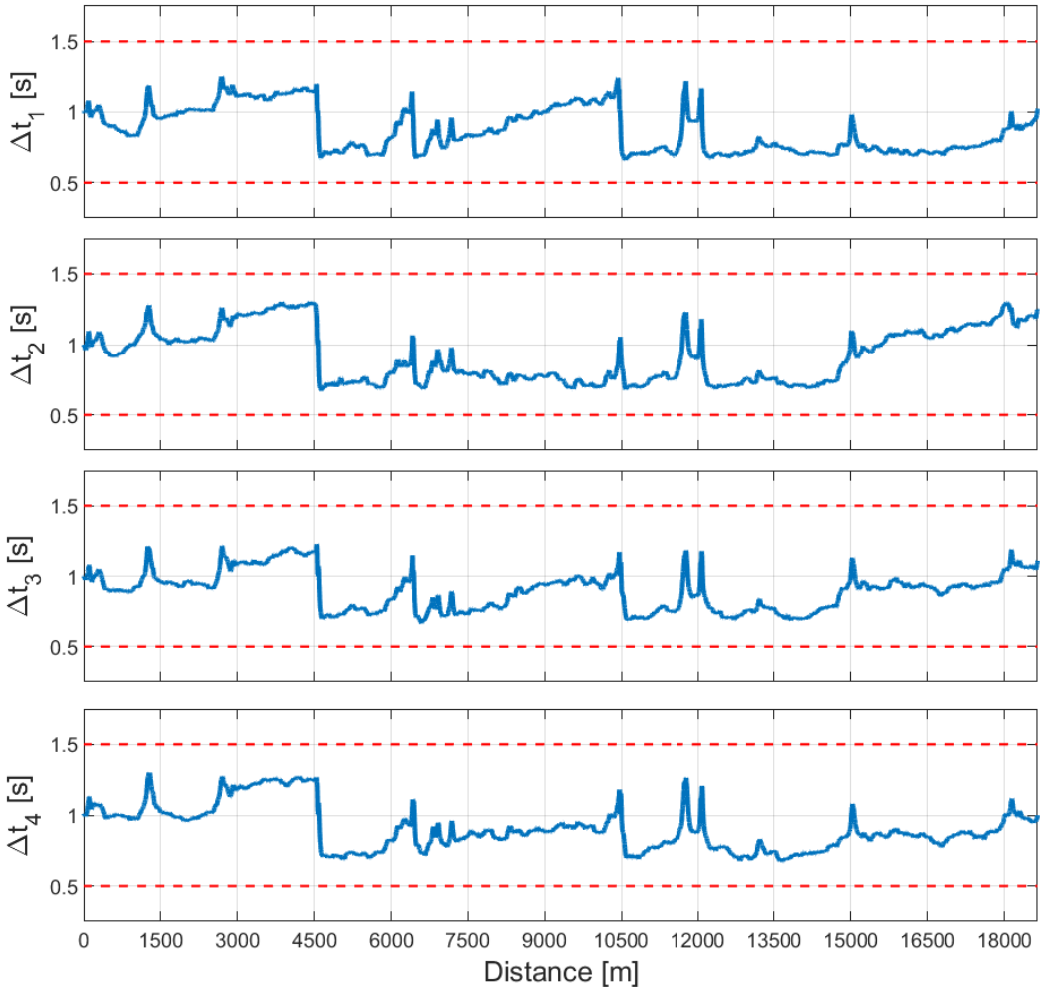


Figure 4.10: The time headway profiles during the experimental driving profile.

## 4.6 Experiment

For the purpose of practical application, more optimization objectives, such as energy consumption and driver comfort, should be taken into account on the basis of (4.31). The updated stage cost function $l_i(\bar{x}_i(j|s), \bar{u}_i(j|s), x^a_{i-1}(j|s))$ is specified as follows:

$$l_i \triangleq W_{i,1}|\Delta\bar{l}_i(j|s) - \Delta| + W_{i,2}|\bar{E}_i(j|s) - \overline{m}_{i,i-1}E^a_{i-1}(j|s)| + W_{i,3}|T_i(j|s) - h_i(j|s)| + W_{i,4}P_i(j|s) + W_{i,5}\xi_i(j|s) \quad (4.51)$$

$W_{i,1}|\Delta\bar{l}_i(j|s) - \Delta|$ and $W_{i,2}|\bar{E}_i(j|s) - \overline{m}_{i,i-1}E^a_{i-1}(j|s)|$ are set to maintain the platoon formation, where $\overline{m}_{i,j} \triangleq m_i/m_j, j \neq i.$ ; $W_{i,3}|T_i(j|s) - h_i(j|s)|$ is utilized to improve passenger comfort, where $h_i(j|s) = \frac{r_i}{\eta_{t,i}}(\frac{2C_{d,i}}{m_i}E^a_i(j|s) + m_i g C_{s,i}(s+j))$. The expression of $h_i(j|s)$ represents the torque required to counterbalance the external aerodynamic drag and tire friction forces; $W_{i,4}P_i(j|s)$ penalizes energy consumption, where $P_i(j|s)$ represents motor power; and $W_{i,5}\xi_i(j|s)$ guarantees the convexification of the problem. In this subsection, the proposed algorithm is denoted as an ecological adaptive tube-based distributed model predictive control (AT-DMPC).

### 4.6.1 Energy Consumption

This section investigates the energy consumption of the proposed method against the IDM strategy [168], the CACC method [167] and the ISMC algorithm [179]. First, simulation is conducted for the electric vehicle platoon utilizing the ecological AT-DMPC approach, operating on a real-world 18.5 km rural road in the UK. Fig. 4.11(a) demonstrates the motor power of each CAV throughout the entire route. Next, we investigate the energy consumption about CAVs with benchmarked CACC controllers. In order to track the preceding vehicle, the feedback mechanism in the benchmark method leads to drastic perturbations in the input torque, resulting in the significant energy wastes. Further comparisons are made against an ISMC algorithm, which maintains platoon formation and handles system uncertainties via introducing a sliding mode surface. However, the chattering problem caused by sliding mode control results in additional energy consumption. Following this,

comparisons are made to the IDM-based strategy, which favors gentle acceleration changes similar to those of human drivers. Nevertheless, the energy efficiency is still worse than the proposed AT-DMPC. Among the aforementioned four methods, the ecological AT-DMPC approach exhibits the best energy efficiency. The reason is that we penalize the motor power as much as possible in the objective function, as long as it satisfies the requirements of platoon formation control and driving comfort. The power profiles of AT-DMPC, IDM, ISMC and CACC discussed above are respectively presented in Figs. 4.11(a), 4.11(b), 4.11(c) and 4.11(d), while the total energy consumption is depicted in Fig. 4.12. In summary, provided similar tracking performance of all methods, the AT-DMPC demonstrates a 9.5% energy savings compared to the IDM strategy, a 11.3% energy savings compared to the ISMC algorithm and a 16.5% energy savings compared to the CACC benchmark.

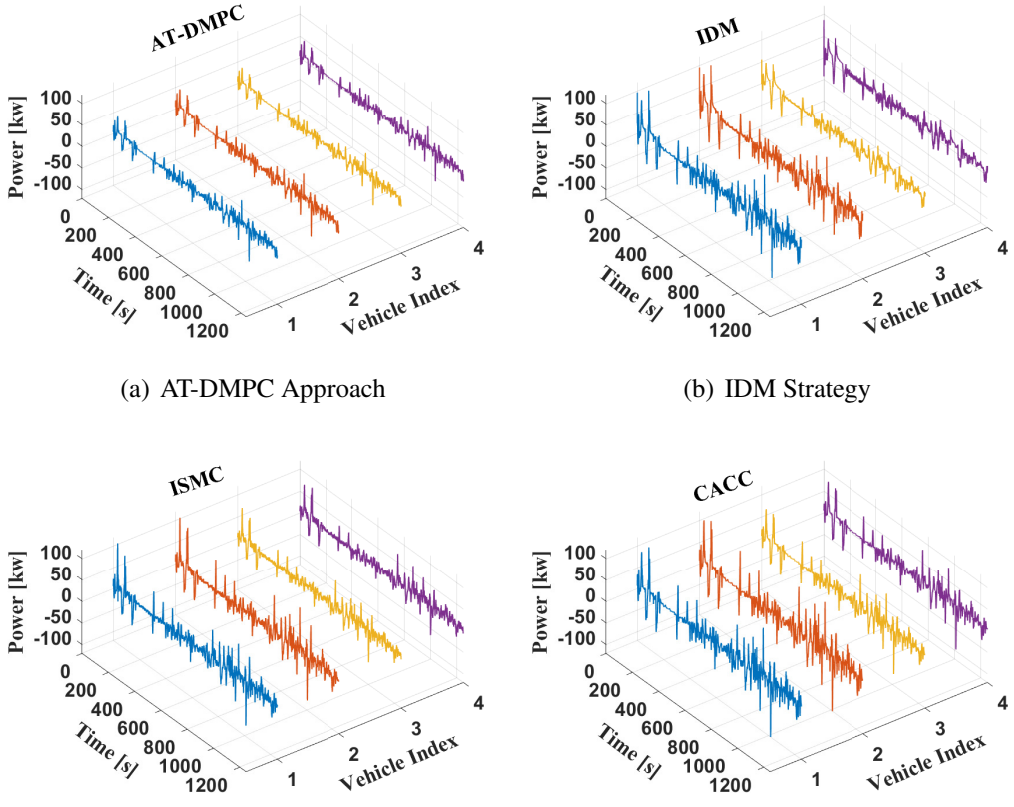


(a) AT-DMPC Approach

(b) IDM Strategy

(c) ISMC Algorithm

(d) CACC Method

Figure 4.11: Motor power requested by different methods.

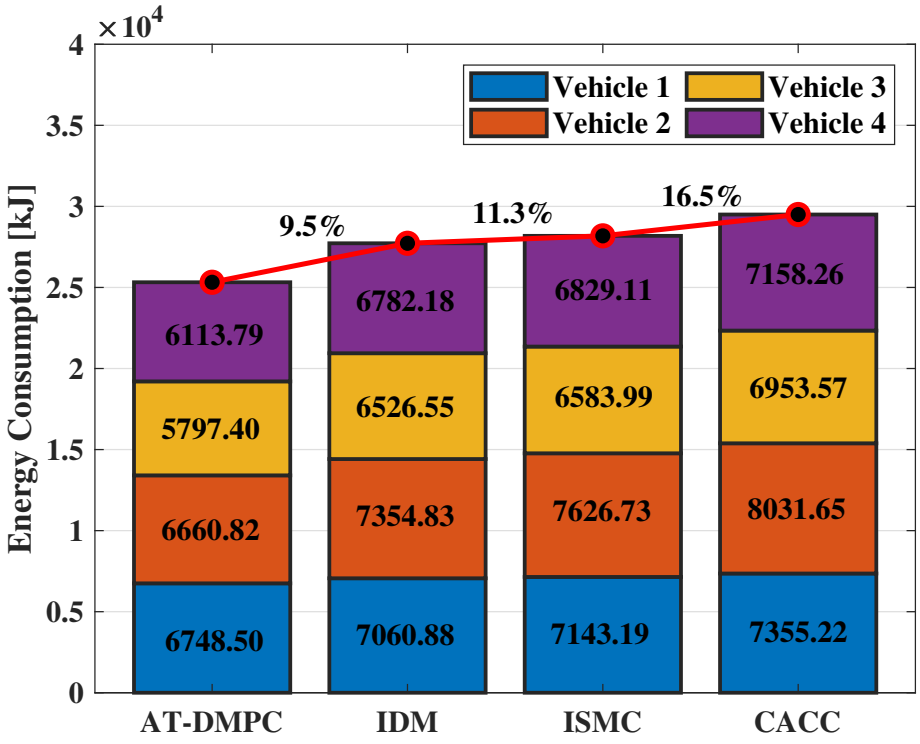


Figure 4.12: The energy consumption comparison among four algorithms.

### 4.6.2 Driver Comfort

Due to the control objective $W_{i,3}|T_i(j|s) - h_i(j|s)|$ in (4.51), the acceleration remains smooth and within $\pm 1.1\ m/s^2$ in 4.13, which meets the commonly acknowledged comfort acceleration limits [169]. Furthermore, other formation maintenance performance are also demonstrated in Figs. 4.14(a),4.14(b),4.14(c),4.14(d).

### 4.6.3 Hardware-in-Loop Experiment

This case verifies the effectiveness of the ecological AT-DMPC approach through a HIL experiment conducted at Tsinghua University, China. In a predetermined highway scenario, a virtual leading vehicle is generated to exhibit notable variations in speed prior to the 30-second mark, maintaining a constant velocity thereafter. Specifically, the speed profile is modeled as:

$$v_0(t) = \begin{cases} 30 + 5\sin(\frac{\pi t}{10}), & 0\ s \leq t < 30\ s \\ 30, & 30\ s \leq t < 40\ s \end{cases} \tag{4.52}$$

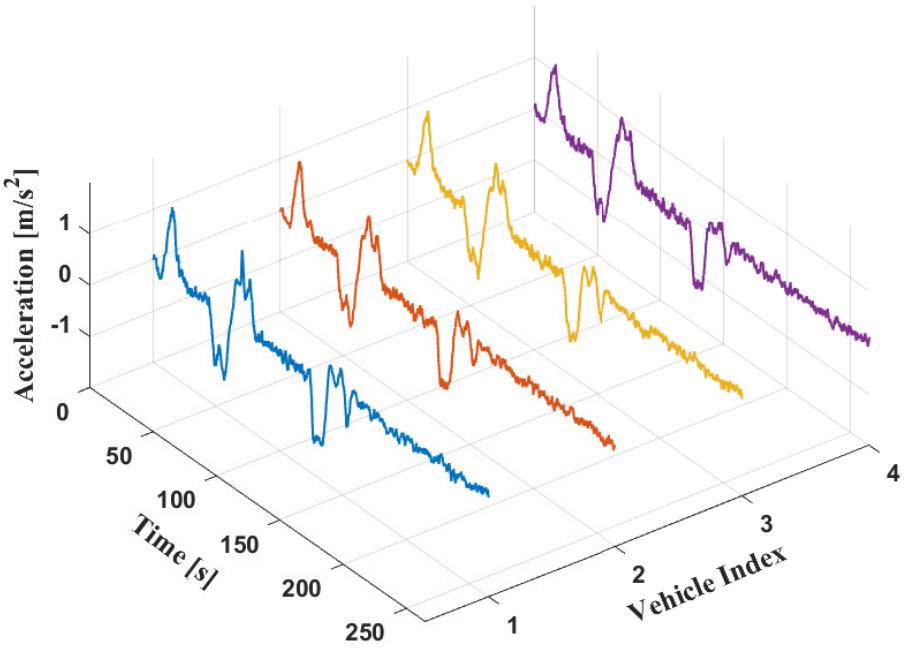


Figure 4.13: The acceleration of all followers during the experimental driving profile.

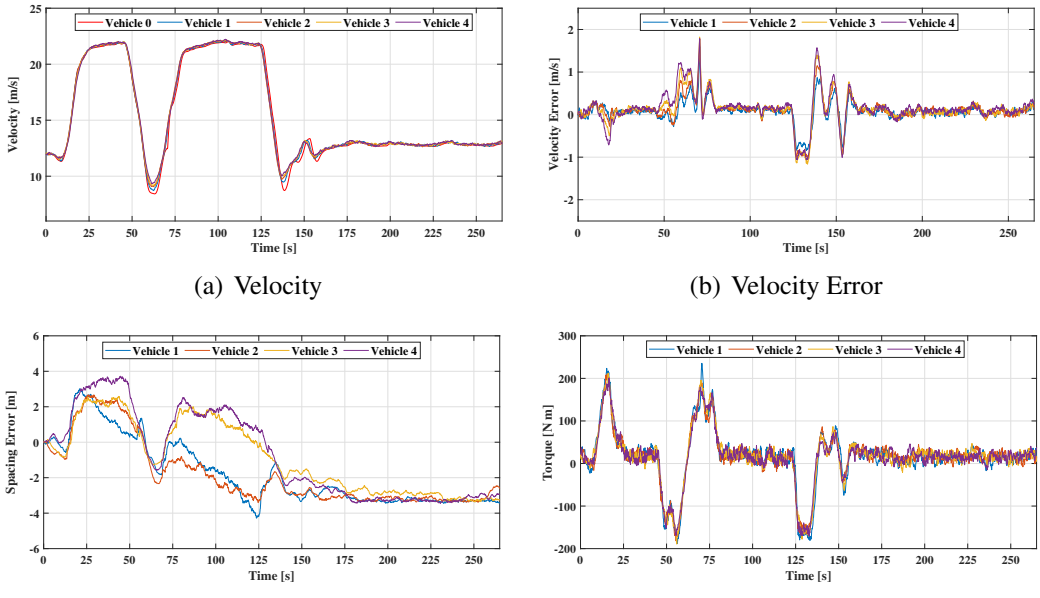


(a) Velocity (b) Velocity Error

(c) Spacing Error (d) Input Torque

Figure 4.14: The tracking performance of the proposed ecological AT-DMPC approach.

The HIL testing platform is composed of the NI real-time computer (RTPC),

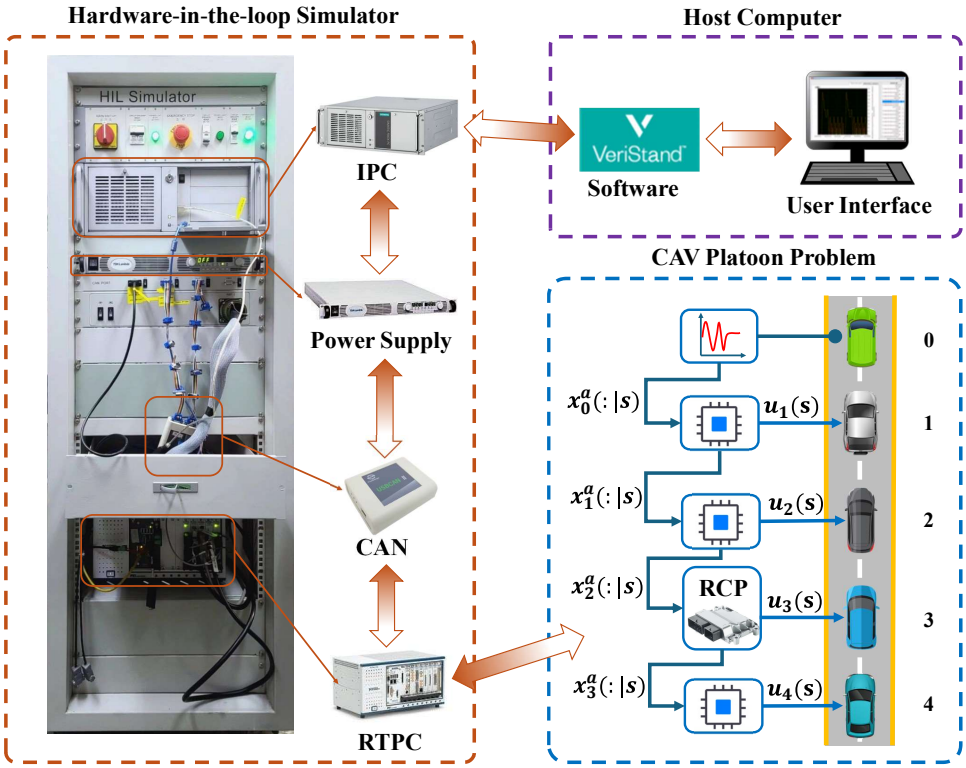


Figure 4.15: Hardware-in-the-loop experiment.

the rapid control prototype (RCP), the controller area network (CAN) bus, the power supply and the HIL host computer. The host computer is installed with NI VeriStand software which manages input and output signals from RTPC, RCP and CAN in real-time. The experimental setup is illustrated in Fig. 4.15, which demonstrates that, with the exception of the controller for Vehicle 3 stored in the RCP, all other environmental aspects are simulated in real-time by the RTPC. The results are presented in Figs. 4.16(a) and 4.16(b), indicating that the ecological AT-DMPC approach can function in real-time for practical applications.

## 4.7 Conclusion

This paper deals with robust vehicle platooning control of heterogeneous CAVs by a convex and tube-based DMPC algorithm, which is able to cope with measurement and modeling uncertainties under PF communication topology. The overall problem is formulated in the space domain rather than using the conventional time

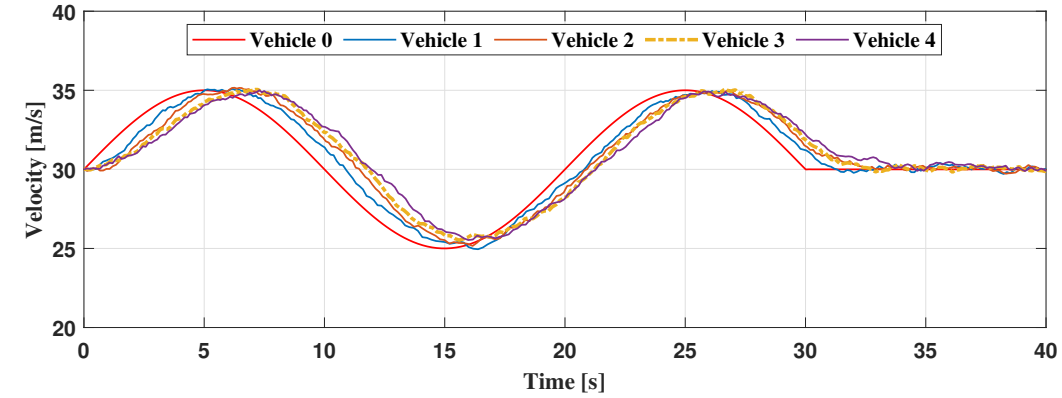


(a) Velocity

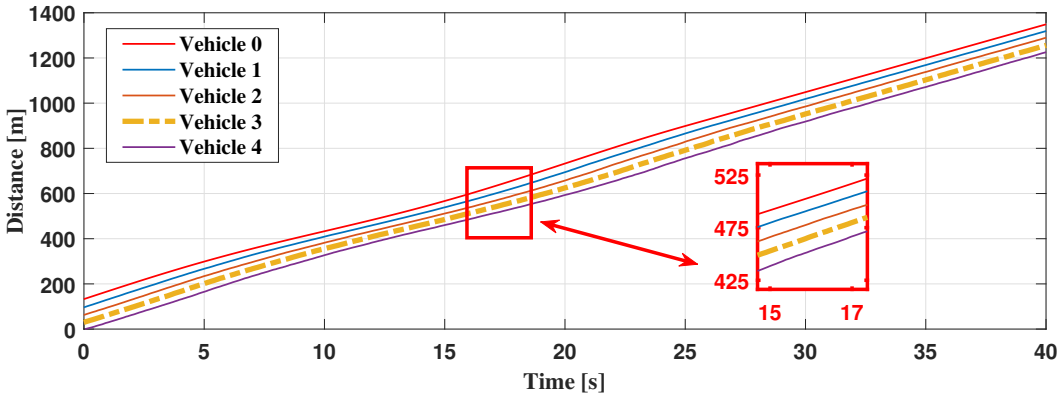


(b) Position

Figure 4.16: Vehicle state profiles in HIL experiment.

domain models, and in this context, the resulting receding horizon optimal control problems can be suitably relaxed as a convex problem, which enables a rapid optimal solution search, which is the key to practical implementation. The relaxation is proved to be valid and non-conservative. The proposed framework also enables coupled state constraints for collision avoidance to be taken into consideration for safety guarantees. Both the recursive feasibility and Lyapunov stability are addressed at the steady state velocity of the leader vehicle.

The performance of the proposed method is simulated on a rural route in the UK, where the road slope and friction coefficient are incorporated accurately. Energy consumption is investigated, which achieves 9.5%, 11.3% and 16.5% savings against the IDM strategy, the ISMC algorithm and the CACC method, respectively. Additional simulations focus on assessing computational efficiency, which is com-

pared with a benchmark non-convex method and another state-of-the-art REACC algorithm. HIL experiments are also conducted in order to confirm that the ecological AT-DMPC approach has the capability for practical applications.

# Chapter 5

# Two-dimensional Multi-CAV Coordination

## 5.1 Introduction

Connected and autonomous vehicle (CAV) control approaches proposed in Chapters 3 and 4 focus on one-dimensional vehicle control subject to longitudinal dynamics only, which falls short in many complex and realistic scenarios. For example, to account for platoon reconfiguration and collision avoidance, vehicles have to be properly controlled over a two-dimensional space. To handle this, a common approach is to employ a two-layer solution respectively for trajectory planning and control/tracking [132, 154, 180]. While the control layer can simply follow the DMPC algorithm proposed in previous chapters, this chapter focuses specifically on path planning. A novel motion planning algorithm based on Artificial Potential Field (APF) is designed with capability of flexible reconfigurable formation of mobile agents. This feature turns out to useful for multi-CAV coordination in practice, especially when dealing with obstacles. Contributions of this motion planning strategy are summarized as follows:

- A novel APF-based path planning algorithm is designed with capability of flexible reconfigurable formation. As such, CAVs may be split into several sub-groups to accomplish complex tasks. Specifically, topology reconfiguration is reactivated in the event of newly detected obstacles, and thus the

overall scheme offers great flexibility in tackling unknown obstacles.

- Following the last point, the proposed APF algorithm ensures the boundedness of the resulting velocity trajectory, which can be beneficial for lower layer trajectory tracking. The convergence of the algorithm is analyzed under the framework of the Lyapunov-like theory.

## 5.2 Problem Statement

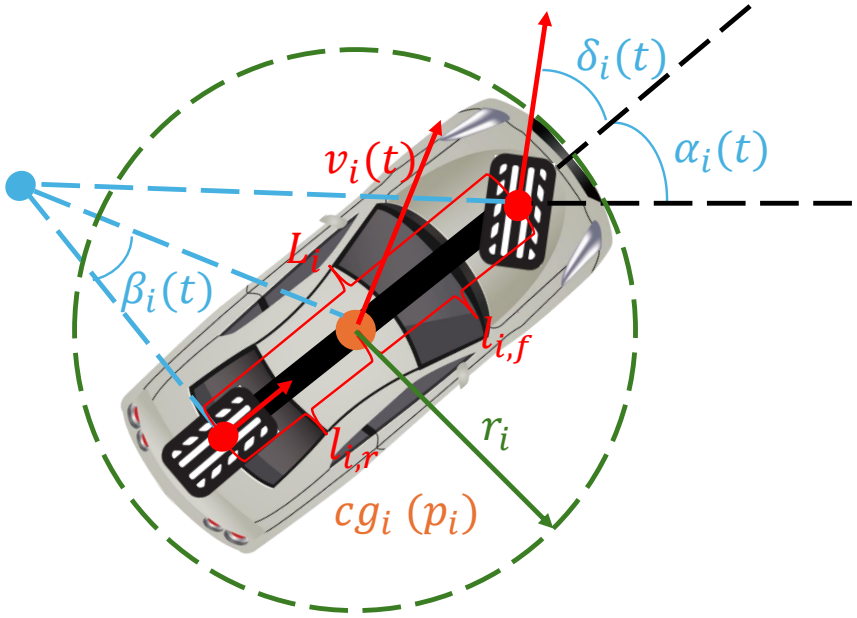


Figure 5.1: Vehicle kinematic bicycle model.

Consider a group of $N$ CAVs in a two-dimensional space which are initially confined in a swarm with the radius of $R_c$, and are requested to travel from their initial positions to the predefined target positions without crashing into each other or the obstacles. In Fig 5.1, the motion of each agent is governed by the vehicle

kinematic bicycle model [181]:

$$\begin{aligned}
\dot{s}_{i,x}(t) &= v_i(t)\cos\big(\alpha_i(t)+\beta_i(t)\big),\\
\dot{s}_{i,y}(t) &= v_i(t)\sin\big(\alpha_i(t)+\beta_i(t)\big),\\
\dot{\alpha}_i(t) &= \frac{v_i(t)\tan\delta_i(t)\cos\beta_i(t)}{L_i},\\
\dot{v}_i(t) &= a_i(t),\\
\dot{\delta}_i(t) &= \omega_i(t),\ \forall i\in\mathbb{A}
\end{aligned} \tag{5.1}$$

where $s_i(t)=[s_{i,x}(t)\ s_{i,y}(t)]^\top$ denotes the center of gravity position ($cg$) of $i$-th CAV, $\mathbb{A}\triangleq\{1,2,\ldots,N\}$. As shown in Fig 5.1, $L_i=l_{r,i}+l_{f,i}$, where $l_{f,i}$ is the distance between the front wheel and $cg$ and $l_{r,i}$ is the distance between the rear wheel and $cg$. $\alpha_i(t)$ represents the heading angle, and $v_i(t)$ and $\omega_i(t)$ are the velocity and the angular velocity, respectively. $\beta_i(t)=\arctan\big(\frac{l_{r,i}\tan(\delta_i(t))}{L_i}\big)$ is the slip angle, where $\delta_i(t)$ denotes the steering angle. Finally, $a_i(t)$ is the CAV acceleration. For each CAV $i$, a collision avoidance range $\mathscr{B}(p_i(t),r_i)$ is constructed, where $p_i(t)$ always coincides with $cg_i$ and $r_i$ is the maximum distance between the CAV profile and $cg_i$.

There are $M$ static obstacles in the environment, which are unknown until they are visible to the CAVs. As shown in Fig. 5.2, let $R_v>0$ be the radius of the visual range (based on all onboard radars or cameras of the CAV $i$). The sensing range can be expressed as $\mathscr{B}(p_i(t),R_v)$. Furthermore, the following assumption is introduced to address the collision avoidance against the obstacles in the unknown environment [155, 182].

**Assumption 5.2.1** *All obstacles are convex polygons with a sequence of detected obstacle contour points* $\{p_l^o(1),p_l^o(2),...,p_l^o(n)\}$*, which are denoted by the red crosses in Fig. 5.2.*

The objective of the proposed approach is to regulate all CAVs so that they can safely converge to a pre-set structure in the steady state by reconfigurable CAV

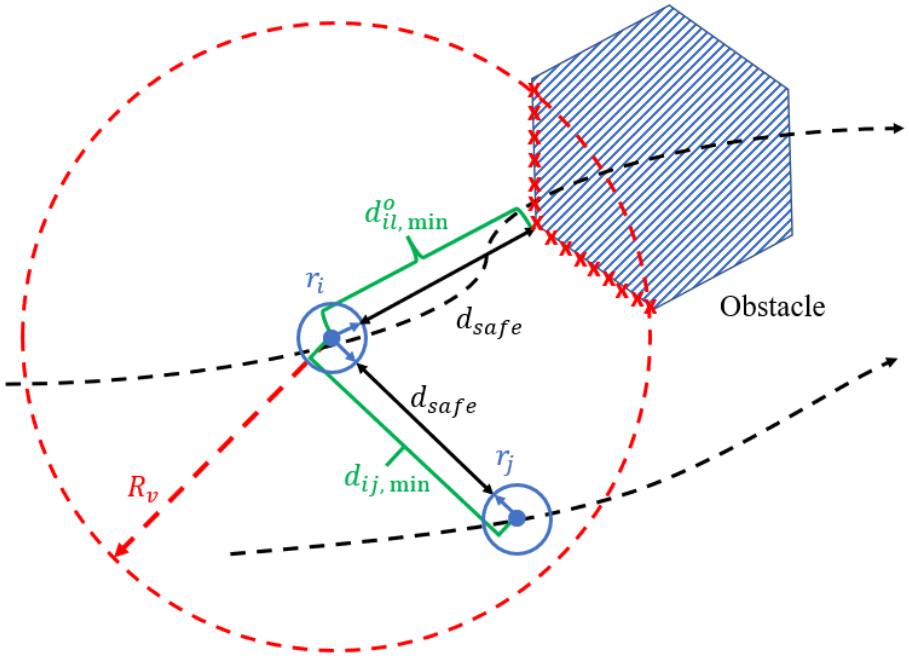


Figure 5.2: A demonstration of the collision avoidance constraints.

formations, such that

$$\lim_{t\to\infty} ||s_i(t) - (p^* + \Delta_i)|| = 0, \quad \forall i \in \mathbb{A} \tag{5.2}$$

$$||s_i(t) - p_j(t)|| \geq d_{ij,\min}, \quad \forall j \in \mathbb{N}_i(t), \quad \forall t \geq 0 \tag{5.3}$$

$$||s_i(t) - p^o_l(n)|| \geq d^o_{il,\min}, \quad \forall l \in \mathbb{O}_i(t), \quad \forall t \geq 0 \tag{5.4}$$

where $p^*$ denotes the center of the target swarm $\mathscr{B}(p^*, R_c)$ whose radius is also $R_c$. $\mathbb{D} = \{\Delta_i \mid i = 1, 2, ..., N\}$ is a set related to the target formation, where $\Delta_i$ represents a vector indicating a fixed offset from $p^*$. During the initialization stage, $p^*$ and $\Delta_i$ are given to corresponding agent $i$, respectively. $d_{ij,\min} = r_i + r_j + d_{safe}$ is the minimal distance between neighboring CAVs (see Fig. 5.2), where $r_i, r_j \in \mathbb{R}_{>0}$ are the radii of CAVs $i$ and $j$, respectively, and $d_{safe} \in \mathbb{R}_{>0}$ is the collision avoidance distance between CAVs. Similarly, the minimum distance between an agent and an obstacle, $d^o_{il,\min} \in \mathbb{R}_{>0}$, follows $d^o_{il,\min} = r_i + d_{safe}$. In addition, $\mathbb{N}_i(t)$ denotes the time-varying neighboring set of agent $i$ with $\mathbb{N}_i(0) = \mathbb{A}\backslash\{i\}$, and $\mathbb{O}_i(t) \subseteq \mathbb{O}$ collects the indices of all obstacles detected by agent $i$ at time $t$ (the set $\mathbb{O}$ includes all obstacles).

## 5.3 Methodology

To solve the problem proposed in Section 5.2, a hierarchical strategy for planning and control is designed. The upper layer employs a two-dimensional single integrator model to generate collision-avoidance trajectories, while the control layer implements an DMPC-based controller that tracks the trajectory, considering the vehicle bicycle model (5.1).

### 5.3.1 Path Planning Approach with Reconfigurable Topology

In this section, an APF-based path planning algorithm is designed to find the trajectories of all CAVs subject to collision avoidance. The trajectory can be formulated based on the following two-dimensional single integrator model:

$$\dot{p}_i(t) = \begin{bmatrix} \dot{p}_{i,x}(t) \\ \dot{p}_{i,y}(t) \end{bmatrix} = \vartheta_i(t) \tag{5.5}$$

In line with the nominal APF algorithm, we propose the control law $\vartheta_i(t)$ for the state $p_i(t)$ as

$$\vartheta_i(t) = \nabla U_{i,att}\big(p_i(t)\big) + \nabla U^a_{i,rep}\big(p_i(t)\big) + \nabla U^o_{i,rep}\big(p_i(t)\big) \tag{5.6}$$

where $U_{i,att}\big(p_i(t)\big) : \mathbb{R}^2 \to \mathbb{R}$ is the attractive potential field, $U^a_{i,rep}\big(p_i(t)\big) : \mathbb{R}^2 \to \mathbb{R}$ and $U^o_{i,rep}\big(p_i(t)\big) : \mathbb{R}^2 \to \mathbb{R}$ are the repulsive potential field against neighbouring CAVs and obstacles, respectively. $\nabla U_{i,att}\big(p_i(t)\big)$, $\nabla U^a_{i,rep}\big(p_i(t)\big)$ and $\nabla U^o_{i,rep}\big(p_i(t)\big)$ are the gradients with respect to $p_i(t)$. More specifically, the attractive potential field follows

$$U_{i,att}(p_i(t)) = \begin{cases} \dfrac{1}{2}k_{att}||p_i(t) - (p^* + \Delta_i)||^2 \Big(\dfrac{R_c}{R^*_i(t)}\Big) & \\ & : p_i(t) \in \mathscr{B}(p^*, R_c) \\ R_c k_{att}||p_i(t) - p^*|| - \dfrac{1}{2}k_{att}R_c R^*_i(t) & \\ & : p_i(t) \notin \mathscr{B}(p^*, R_c) \end{cases} \tag{5.7}$$

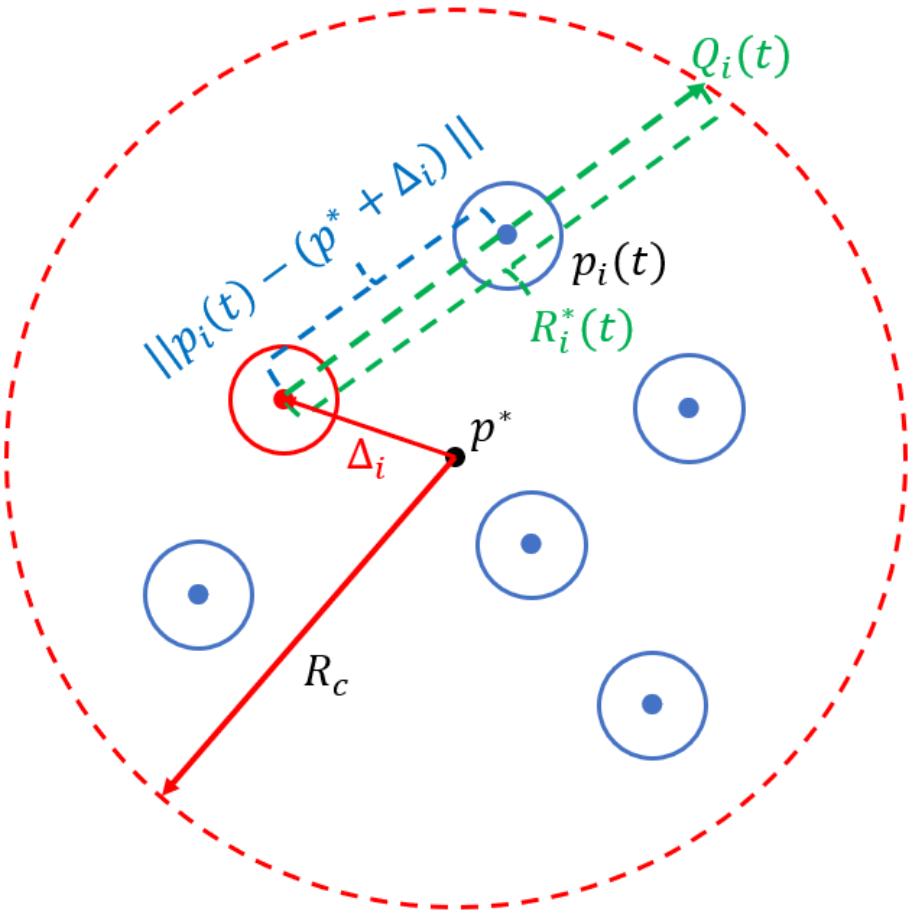


Figure 5.3: Schematic diagram about normalized radius $R_i^*(t)$ design.

where $k_{att} > 0$ is an adjustable intensity parameter of the attractive potential field. Furthermore, $R_i^*(t) \in \mathbb{R}_{>0}$ is a normalizing distance introduced to ensure convergence of an agent at the target position after entering the target range $\mathscr{B}(p^*, R_c)$. As shown in Fig. 5.3, it is defined as $R_i^*(t) = ||p^* - Q_i(t)||$, where $Q_i(t)$ is the intersection with the circumscribed circle of $\mathscr{B}(p^*, R_c)$ and the directed line segment $\overrightarrow{p^* p_i(t)}$. The gradient of $U_{i,att}(p_i(t))$ follows

$$\nabla U_{i,att}\big(p_i(t)\big) = \begin{cases} k_{att}\big(p_i(t) - (p^* + \Delta_i)\big)\left(\dfrac{R_c}{R_i^*(t)}\right) & : p_i(t) \in \mathscr{B}(p^*, R_c) \\ \dfrac{R_c k_{att}\big(p_i(t) - p^*\big)}{||p_i(t) - p^*||} & : p_i(t) \notin \mathscr{B}(p^*, R_c) \end{cases} \tag{5.8}$$

As it can be noticed, when $p_i(t)$ is outside the target range $\mathscr{B}(p^*, R_c)$, $\nabla U_{i,att}$ introduces a constant attractive control that drives $p_i(t)$ towards $p^*$. In case that $p_i(t)$ is inside the circle, it holds that $\nabla U_{i,att}\big(p_i(t)\big) = 0$ when $||p_i(t) - \big(p^* + \Delta_i\big)|| = 0$. Furthermore, it can be verified that $U_{i,att}\big(p_i(t)\big)$ and $\nabla U_{i,att}\big(p_i(t)\big)$ are continuous at the switching boundary, i.e., the two segments of the piece-wise function are identical when $||p_i(t) - p^*|| = R_i^*(t)$. As illustrated in Figure. 5.3, when the agent $i$ is located on the boundary of $\mathscr{B}(p^*, R_c)$, it holds that $p_i(t) - (p^* + \Delta_i) = R_i^*(t)$ and $p_i(t) - p^* = R_c$. These conditions ensure the continuity of $\nabla U_{i,att}(p_i(t))$.

Next, the two repulsive potential functions are designed as follows to avoid collisions against other CAVs and obstacles during the mission

$$
\begin{aligned}
&U^a_{i,rep}(p_i(t)) = \\
&\begin{cases}
\sum\limits_{j\in\mathbb{N}_i(t)} \Big( \dfrac{\Psi}{2(d_{ij,\min} - d_{ij,\max})} d_{ij}^2(t) - \dfrac{\Psi d_{ij,\max}}{d_{ij,\min} - d_{ij,\max}} d_{ij}(t) \\
\qquad\qquad + \dfrac{\Psi d_{ij,\max}^2}{2(d_{ij,\min} - d_{ij,\max})} \Big) & : d_{ij}(t) \le d_{ij,\max} \\
0 & : d_{ij}(t) > d_{ij,\max}
\end{cases}
\end{aligned}
\tag{5.9}
$$

where $d_{ij}(t) = ||p_i(t) - p_j(t)||$ denotes the distance between agent $i$ and agent $j$. $\Psi$ is the pre-set threshold for the repulsive field and $d_{ij,\max} = r_i + r_j + d_{\max}$ with $d_{\max}$ the designed maximum distance interval to activate the repulsive field.

$$
\begin{aligned}
&\nabla U^a_{i,rep}(p_i(t)) = \\
&\begin{cases}
\sum\limits_{j\in\mathbb{N}_i(t)} \Big( \dfrac{\Psi}{d_{ij,\min} - d_{ij,\max}} d_{ij}(t) - \dfrac{\Psi d_{ij,\max}}{d_{ij,\min} - d_{ij,\max}} \Big) \nabla d_{ij}(t) \\
\qquad\qquad\qquad\qquad\qquad\qquad : d_{ij}(t) \le d_{ij,\max} \\
0 \qquad\qquad\qquad\qquad\qquad\qquad : d_{ij}(t) > d_{ij,\max}
\end{cases}
\end{aligned}
\tag{5.10}
$$

where $\nabla d_{ij}(t) = \frac{p_i(t) - p_j(t)}{||p_i(t) - p_j(t)||}$. The repulsive potential function (5.9) is continuous and linearly dependent on the interval between CAVs. The motivation is to circumvent unbounded gradient as with the existing APF algorithms where the repulsive force is proportional to the reciprocal of the interval. By analogy, $\nabla U^o_{i,rep}\big(p_i(t)\big)$

with respect to obstacles can be constructed following the same form of (5.10), but replacing the index $j \in \mathbb{N}_i$ with $l \in \mathbb{O}_i(t)$. It is worth noting that $\mathbb{O}_i(t)$ can be shared with all neighboring CAVs to avoid mutual occlusion. As obstacles are not available at the beginning, generation of the trajectory $p_i(t)$ by reproducing $u_i(t)$ using the proposed APF algorithm will be necessary during the mission.

Furthermore, the maximum magnitude of the repulsive control is achieved when $d_{ij}(t) = d_{ij,\min}$, which yields $\max\{||\nabla U_{i,rep}(p_i(t))||\} = ||\Psi||$ in view of (5.10). Combining with the bounded attractive input (5.8), the resulting control law (5.6) can be bounded by design, which greatly facilitates tracking of the generated trajectories [157]. On the other hand, $d_{ij,\max}$ is the maximum distance to activate the repulsive field (5.9), therefore, agent $i$ only connects with CAVs with $d_{ij}(t) \leq d_{ij,\max}$. As illustrated in Fig. 5.4, there is no connection between agent 2 and agent 4 due to the distance $d_{24}(t)$ being longer than $d_{24,\max}$. At the next time instant, positions of CAVs shift, resulting in an evolution in the topology change which is shown in the figure.

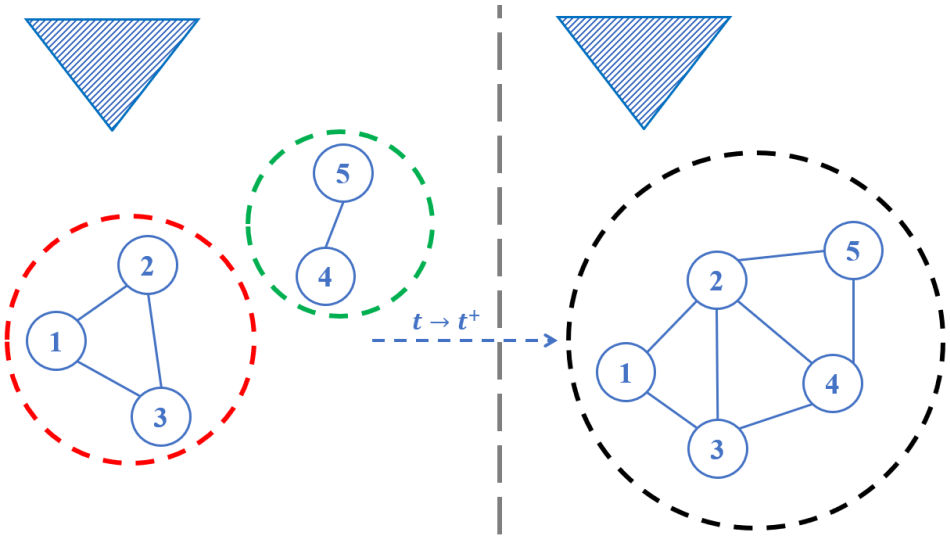


Figure 5.4: Schematic diagram about topology changes of the connected CAVs.

**Remark 5.3.1** *To prevent CAVs from falling into a deadlock, a small perturbation can be introduced to the APF control law* (5.6) *to enforce CAVs escaping from deadlock [183].*

### 5.3.2 Distributed Model Predictive Control for Each CAV

To track the trajectory generated by the proposed path planning Algorithm (5.1), a DMPC controller is introduced in this section, which can be defined as follows:

**OCP 5**

$$\min_{s_i(t)} J_i(t) = \sum_{k=0}^{N_p-1} ||s_i(k|t) - p_i(k|t)|| \tag{5.11a}$$

***s.t.*** *for* $k = 1,2,\ldots,N_p-1$

$$s_i(k+1|t) = s_i(k|t) + f_i\big(x_i(k|t), u_i(k|t)\big)\Delta t \tag{5.11b}$$

$$s_i(k|t) \in \mathscr{C}_{ij}\big(s_i(t), s_j(t)\big) \tag{5.11c}$$

$$x_{i,np}(k|t) \in \mathbb{X}_i \tag{5.11d}$$

$$u_i(k|t) \in \mathbb{U}_i \tag{5.11e}$$

$$x_i(0|t) = x_i(t) \tag{5.11f}$$

$$s_i(N_p|t) \in \mathscr{B}\big(p_i(N_p|t), d_{i,ter}\big) \tag{5.11g}$$

where $x_i(t) = [s_i(t), v_i(t), \alpha_i(t), \delta_i(t)]^\top$ denotes the system state, $x_{i,np}(t) = [v_i(t), \alpha_i(t), \delta_i(t)]^\top$ denotes the non-position state and $u_i(t) = [a_i(t), \omega_i(t)]^\top$ denotes the system control input. Moreover, (5.11a) represents the vehicle kinematic bicycle model (5.1) after discretization. (5.11b) is a coupled position constraint which is utilized for collision avoidance. Other non-position constraints are introduced in (5.11d). (5.11e) denotes the system input constraint including acceleration and angular velocity of CAV. The initial and terminal constraints of the MPC are specified by (5.11f) and (5.11g). Overall, the proposed algorithm is summarized in Algorithm 4 below.

**Algorithm 4** The planning-and-control CAV coordination strategy

**Online:**

Measure the current state $x_i(t)$;
**if** $s_i(t) = p^* + \Delta_i$ **then**
    CAV $i$ stops;
**else if** $s_i(t) \neq p^* + \Delta_i$ **then**
    Set the initial condition (5.11f) of the MPC problem (5.11) based on the measured value $x_i(t)$
    Measure the positions of all neighboring CAVs and obstacles;
    Generate reference trajectory $p_i(:|t)$ based on the proposed path planning algorithm 5.3.1
    Solve OCP 5 and obtain optimal solution $u_i^*(:|t)$;
    Apply the control action $u_i(t) = u_i^*(0|t)$ to the actual system (5.1);
**end if**
$t \leftarrow t + \Delta t$;
Back to **step 1**;

**Assumption 5.3.1** *Each coupled state constraint* $\mathscr{C}_{ij}\big(s_i(t), s_j(t)\big)$ *for collision avoidance can be converted into corresponding consistency constraint:*

$$\mathscr{C}_{ij}\big(s_i(t), s_j(t)\big) \Rightarrow \mathscr{B}\big(p_i(t), d_{i,safe}\big) \ \& \ \mathscr{B}\big(p_j(t), d_{j,safe}\big)$$

*where related concepts can be found in [184, 185].*

**Remark 5.3.2** *Considering the circular boundary of CAVs shown in Figure 5.1, the control strategy proposed in this chapter exhibits limitations in scenarios where the road is narrow and the size of the CAV is comparatively large.*

## 5.4 Theoretical Analysis

To ensure the effectiveness of the proposed algorithm, this section provides a mathematical analysis to show that all agents can be driven toward the target trajectory by the proposed APF-based algorithm. The following assumption is needed to proceed with the analysis.

**Assumption 5.4.1** *The individual target formation* $p_i^* + \Delta_i$ *is set such that the condition* $||\Delta_i - \Delta_j|| \geq d_{ij,\max}, \forall i, j \in \mathbb{A}$ *is satisfied.*

**Assumption 5.4.2** *There exists a time $T$ such that for all $t > T$, the environment is free of obstacles, and thus, the repulsive forces are no longer considered.*

The purpose of Assumption 5.4.1 is to ensure that the repulsive potential function is inactive when all CAVs form the desired formation. This can be achieved by a proper design of $d_{\max}$. Assumption 5.4.2 implies that obstacles are separated from target range $\mathscr{B}(p^*, R_c)$ in steady state so that targets can be reached without activating the repulsive potential function imposed by obstacles.

**Theorem 5.4.1** *Under Assumptions 5.2.1, 5.4.1 and 5.4.2, given the agent kinematic model* (5.1) *and the APF-based control law* (5.6)*, CAVs can form the predefined desired formation, $p_i(t) \to p^* + \Delta_i, \forall i \in \mathbb{A}$ when $t \to \infty$.*

**Proof:** Define the tracking error of an agent $i$

$$e_i(t) = p_i(t) - (p^* + \Delta_i),\ \forall i \in \mathbb{A} \tag{5.12}$$

By applying (5.12) to (5.7)-(5.10), $U_{i,att}$, $U^a_{i,rep}$ , $\nabla U_{i,att}$ and $\nabla U^a_{i,rep}$ can be represented as functions of $e_i(t)$ rather than $p_i(t)$. Then, in view of (5.6), it can be shown that

$$\begin{aligned} \dot{e}_i(t) &= \dot{p}_i(t) - (\dot{p}^* + \dot{\Delta}_i) \\ &= \nabla U_{i,att}\big(p_i(t)\big) + \nabla U^a_{i,rep}\big(p_i(t)\big). \end{aligned} \tag{5.13}$$

It is noted that the repulsive potential functions introduced are ignored according to Assumption 5.4.2.

Consider the Lyapunov candidate with respect to $\mathbf{e}(t) = [e_1(t)^\top, e_2(t)^\top, \ldots, e_N(t)^\top]^\top$

$$V(\mathbf{e}(t)) = \sum_{i \in \mathbb{A}} \frac{1}{2} e_i(t)^\top e_i(t) \tag{5.14}$$

where $V(\mathbf{e}(t))$ as shown above is always positive definite. In addition, $V(0) = 0$ as $U_{i,att} = 0$ when $e_i = 0$ and $U^a_{i,rep} = 0$ when $e_i = e_j = 0$ (due to the fact that both CAVs are at the target positions provided $d_{ij}(t) > d_{ij,\max}$). The derivative of $V$ along

the system trajectory is

$$\begin{aligned}\dot{V}(\mathbf{e}(t)) &= \sum_{i\in\mathbb{A}} \Big( e_i(t)^\top \dot{e}_i(t) \Big) \\ &= \sum_{i\in\mathbb{A}} e_i(t)^\top \Big( \nabla U_{i,att}\big(p_i(t)\big) + \nabla U^a_{i,rep}\big(p_i(t)\big) \Big)\end{aligned} \tag{5.15}$$

The summation of the repulsive field gradients equals zero, and the gradient of attractive field always opposes the direction of $e_i(t)$. Therefore, $\dot{V}(\mathbf{e}(t)) < 0$, indicating that the proposed MAS is asymptotically stable and $p_i(t) \rightarrow\ p^* + \Delta_i, t \rightarrow \infty, i \in \mathbb{A}$.

## 5.5 Simulation

The numerical example is carried out in this section to verify the effectiveness of the proposed algorithm. Consider a MAS of ten CAVs, which are randomly placed within the swarm $\mathscr{B}([0,0], R_c)$ at the initial step. The final target is to achieve a desired triangular formation at the steady state. Table 5.1 summarizes the initial positions and dimensions of all CAVs, while the chosen parameters for swarm dimension and the parameters of the APF algorithm are provided in Table 5.2. Simulation results are shown in Fig. 5.5. The CAVs can be driven to form the desired formation within $\mathscr{B}(p^*, R_c)$ and avoid all three obstacles in the environments during the mission by topology reconfiguration - splitting into multiple swarms and merging back when necessary.

Table 5.1: Initial Positions and Agent Radii

| Agent | 1 | 2 | 3 | 4 | 5 | 6 | 7 | 8 | 9 | 10 |
|---|---|---|---|---|---|---|---|---|---|---|
| $p_{i,x}(0)$ | 13.6 | 54.3 | -53.0 | 41.4 | -25.9 | 7.7 | -44.9 | -51.3 | -15.6 | -0.2 |
| $p_{i,y}(0)$ | -49.3 | -41.0 | -12.1 | 8.5 | -30.7 | 51.4 | 22.6 | -50.1 | 31.5 | 2.8 |
| $r_i[m]$ | 2.60 | 4.25 | 3.58 | 4.91 | 3.61 | 2.38 | 2.12 | 4.52 | 3.84 | 3.81 |

Moreover, in order to highlight the advantages of the proposed algorithm, a state-of-the-art swarm-based APF control algorithm [186] is set as benchmark in the same simulation environment. In contrast to the proposed method, the method in [186] requests all CAVs to remain in a swarm by following a predefined virtual

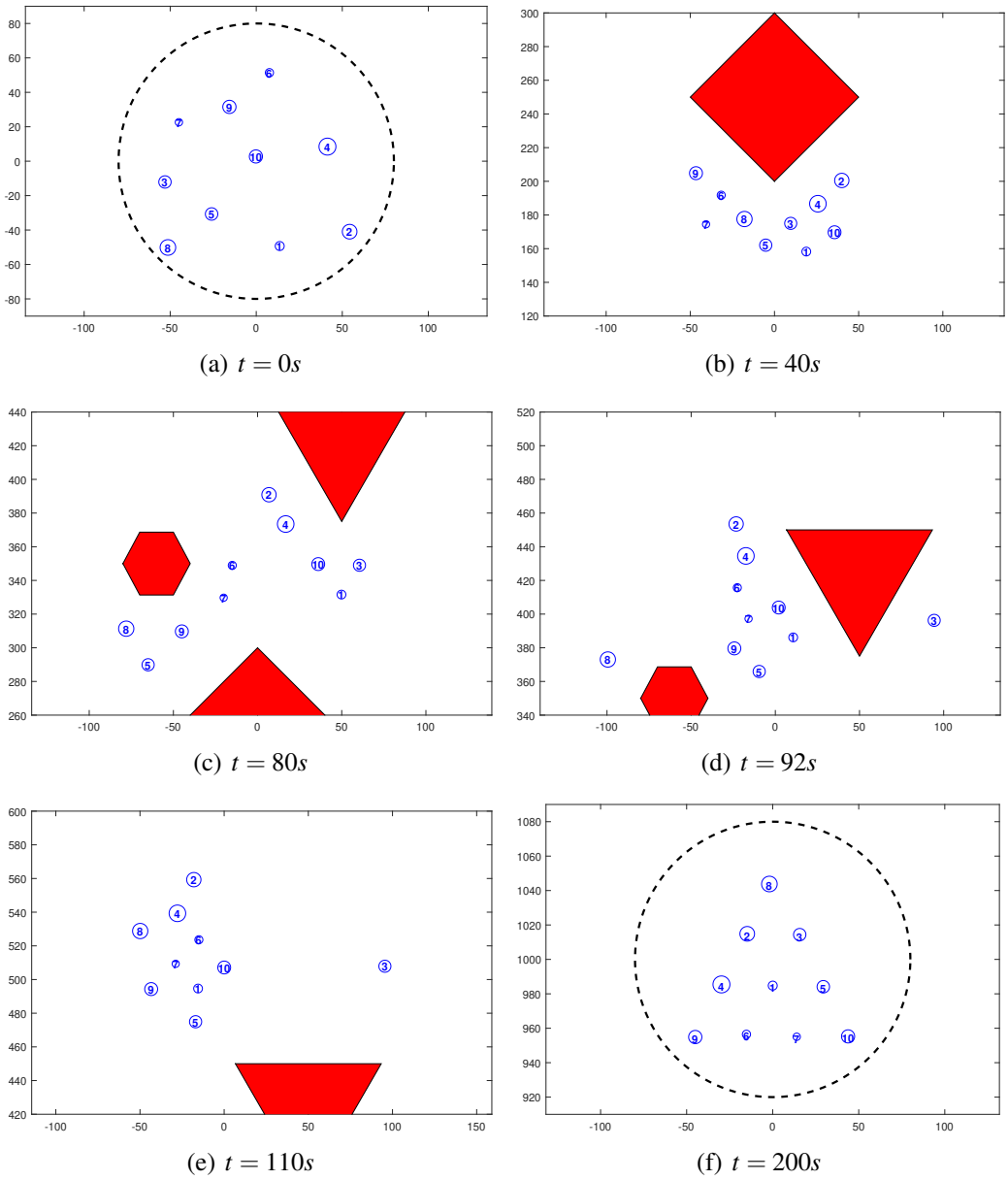

(a) $t = 0s$ (b) $t = 40s$

(c) $t = 80s$ (d) $t = 92s$

(e) $t = 110s$ (f) $t = 200s$

Figure 5.5: Episodes of the generated trajectories by the proposed method, where the coordinate unit is 'meter'. (a) CAVs' initial positions are randomly generated in the initial range $\mathscr{B}([0,0],R_c)$. (b) $t = 40$s, the diamond obstacle appears and enforces the CAVs to re-generate the trajectories. (c) $t = 80$s, CAVs pass over the first obstacle and start to tackle the hexagonal obstacle and the triangle obstacle via topology reconfiguration. (d) $t = 92$s, the proposed strategy enables all CAVs to make use of the small space between obstacles. (e) $t = 110$s, CAVs completely pass all obstacles. (f) $t = 200s$, CAVs reach the target swarm range $\mathscr{B}(p^*,R_c)$ and form the pre-defined formation. It is worth noting that the obstacles in the figure can be regarded as buildings in the real world.

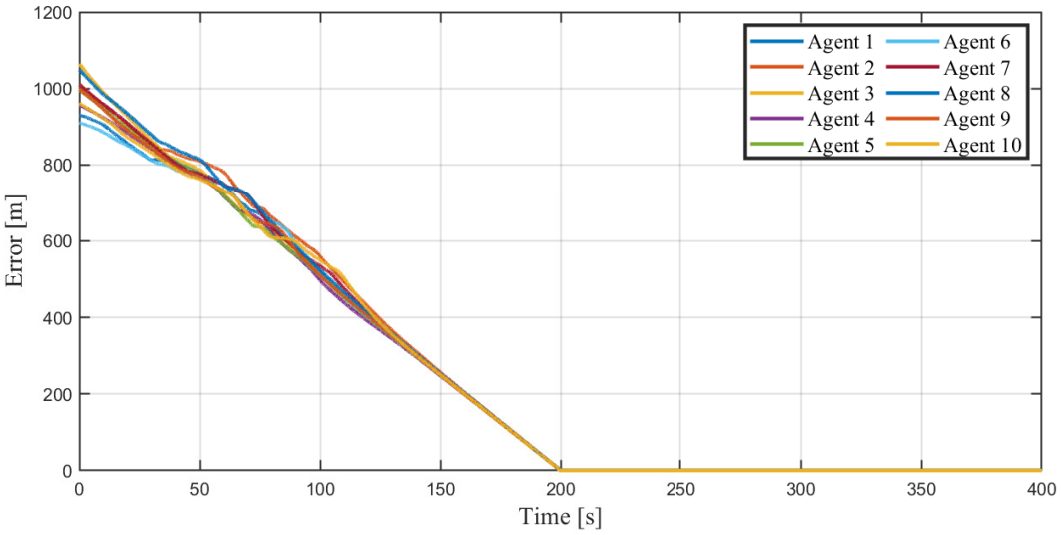


(a) Tracking error $||p_i(t) - (p^* + \Delta_i)||$ of the proposed algorithm.

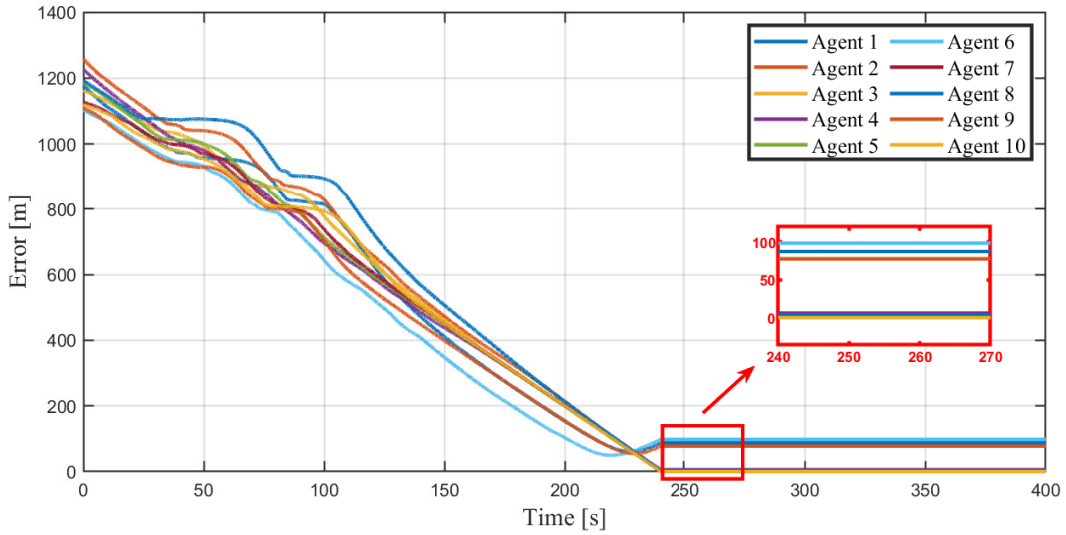


(b) Tracking error $||p_i(t) - p^*||$ of the benchmark.

Figure 5.6: The Sub-figure (a) illustrates the tracking error $||p_i(t) - (p^* + \Delta_i)||$ of the proposed algorithm; The Sub-figure (b) shows the tracking error $||p_i(t) - p^*||$ of the benchmark.

Table 5.2: Parameters about APF model and swarm size

| Description | Symbols | Values |
|---|---|---|
| Intensity parameter | $k_{att}$ | 0.08 |
| External circle radius of swarm | $R_c$ | $80m$ |
| Max repulsive field gradient | $\Psi$ | $-65m/s$ |
| Safe distance | $d_{safe}$ | $2m$ |
| Max distance for repulsion activation | $d_{\max}$ | $10m$ |

leader (illustrated by the red circle labeled as "v"). The comparison results are shown in Fig. 5.6(a). In details, Fig. 5.6(a) demonstrates how the tracking errors converge under the control of the proposed algorithm. As it can be noticed, CAVs form the pre-determined structure in $\mathscr{B}(p^*, R_c)$, taking 200 seconds. Meanwhile, the result of the benchmark method is illustrated in Fig. 5.6 (b). Due to the CAVs being confined to a fixed area, they are unable to pass through the obstacles from both sides, resulting in a longer convergence time of 241 seconds. Additionally, as shown in Fig. 5.7, agent 1, agent 6 and agent 9 are forced to leave the swarm to avoid collisions owing to limited space. Due to the repulsive force applied at the outer edge of the swarm by the benchmark, once an agent leaves, it cannot rejoin the swarm. Such an issue might be addressed by refining the reference, which, however, is challenging in the presence of initially unknown obstacles, and the flexibility introduced by the proposed algorithm can circumvent the challenge.

## 5.6 Conclusion

This paper investigates a two-dimensional space coordination problem for multiple CAVs in a constrained environment. A reconfigurable distributed path planning approach is designed using the concept of the artificial potential field. Instead of confining all CAVs within a swarm, the proposed algorithm allows the swarm of CAVs to split into multiple groups or merge into a single swarm to cope with the emerging obstacles for enhanced flexibility during the task. The convergence of the algorithm is proved by using the Lyapunov theory. Numerical results verify the effectiveness of the proposed method and the benefit of enabling topology reconfiguration.

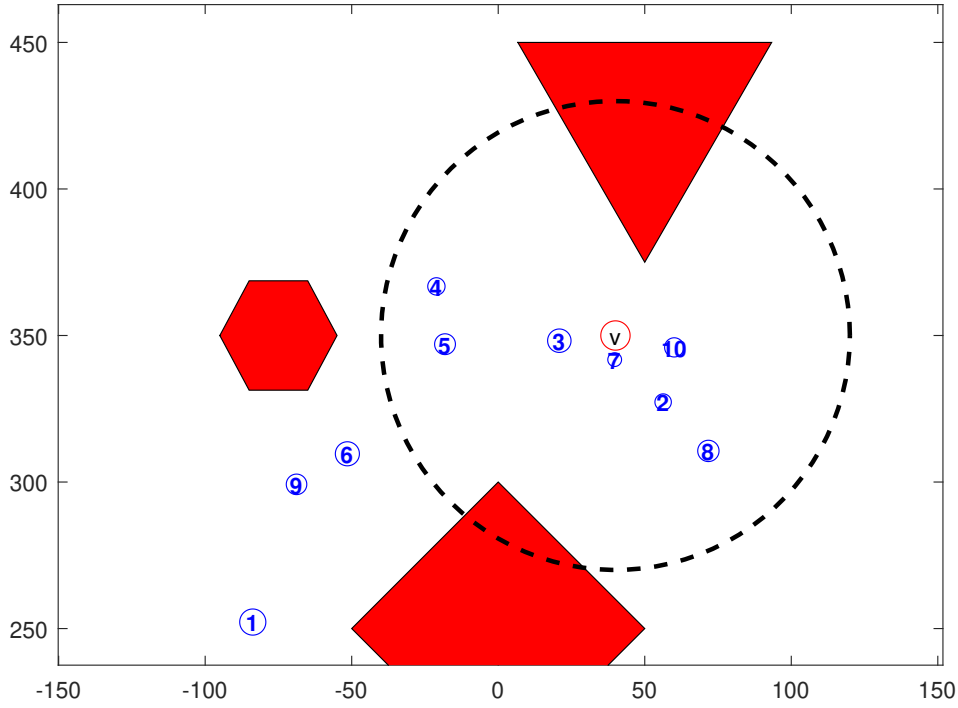


Figure 5.7: Path planning following a fixed swarm configuration subject to the given virtual leader denoted by 'v'. CAVs are pushed out of the swarm in event of a large obstacle.

# Chapter 6

# Conclusion and Future Works

## 6.1 Conclusion

With the increasing number of vehicles, it is important for humans to address and mitigate issues related to energy consumption, environmental pollution, and traffic accidents, where advanced CAV technologies are widely considered as a promising solution to improve traffic conditions in the near future. In this thesis, MPC-based CAV controllers are designed with consideration of safety, robustness, energy consumption, and computational efficiency in different scenarios, such as the car-following case, the vehicles platooning case, and the multiple vehicles coordination case. Moreover, numerical simulations, Hardware-in-the-loop experiments, and vehicle on-road experiments are employed to validate effectiveness of the proposed strategies.

**Single CAV car-following scenario:** In Chapter 3, a learning-based ecological car-following strategy for CAVs is designed. Leveraging advanced vehicle-to-vehicle and vehicle-to-infrastructure technologies, CAVs on roads can receive updated traffic flow information and predict the speed profile of the preceding vehicle using a macro-micro fused spatial-temporal transformer. To handle the discrepancies between the predicted and actual speeds of the preceding vehicle and achieve less conservative results, a robust learning-in-the-loop model predictive control algorithm has been developed. Furthermore, to enable real-time computation for practical applications, the system models are transformed from the time domain to the

spatial domain, integrating a fictitious control input design for system convexification. Finally, a comprehensive assessment of the proposed strategy is conducted through numerical simulations and on-road vehicle experiments.

**Heterogeneous CAVs platooning scenario:** Chapter 4 addresses the platooning problem of heterogeneous CAVs with consideration of a time-varying leader speed and multi-dimensional uncertainties that include modeling uncertainties and local measurement disturbances. Then, a convex and tube-based distributed model predictive control algorithm (DMPC) utilizing a predecessor-following communication topology is designed with certified theoretical properties, which can be boiled down to DMPC parameter tuning criteria. Finally, numerical simulations and hardware-in-the-loop experiments are conducted to assess the performance of the proposed method relative to several state-of-the-art algorithms.

**Two-dimensional multi-CAV coordination:** A two-dimensional space planning-and-control strategy is proposed in Chapter 5, which can achieve safety-guaranteed motion in an unknown constrained environment. By considering the sensing range and CAV dimension, a group of artificial potential field functions are designed aiming at enabling CAVs reconfiguration (e.g., split and merge) for reinforced flexibility. A distributed MPC algorithm is then developed to achieve formation tracking while avoiding any potential collisions. Theoretical analysis using the Lyapunov theory is given to guarantee the performance of the system. Finally, numerical simulations are carried out to verify the effectiveness of the proposed algorithm and its superiority against conventional methods.

## 6.2 Future Works

In the future, some details not discussed in this thesis will be further expanded upon. In terms of problem setup, traffic lights will be integrated into the urban scenario. Additionally, the steering and overtaking behaviors of vehicles will also be considered. Regarding communication, a switching topology framework and the associated information transmission delays will be explored. As for safety-critical control used for collision avoidance among CAVs, additional methods such

as control barrier functions and Hamilton-Jacobi reachability analysis theories will be studied.

# Bibliography


[1] Statistics on vehicles in use. *https://www.oica.net/statistics/* [Online], 2024. International Organization of Motor Vehicle Manufacturers.

[2] Global statistical data regarding on-road vehicles. *https://www.oyez.org/cases/* [Online], 2024. World motor vehicle data from Motor Vehicle Manufacturers Association of the United States.

[3] Michelle Birdsall. Google and ITE: The road ahead for self-driving cars. *Institute of Transportation Engineers. ITE Journal*, 84(5):36, 2014.

[4] Product innovation: Autonomous driving. *https://group.mercedes-benz.com/innovation/autonomous-driving/*[Online], 2024. Mercedes-Benz Group.

[5] Mobility goes smart and individual: Audi at ces 2020. *https://www.audi-mediacenter.com/en/press-releases/mobility-goes-smart-and-individualaudi-at-ces-2020-12455*[Online], 2020. Audi Media Center.

[6] Heather Somerville, Paul Lienert, and Alexandria Sage. Uber's use of fewer safety sensors prompts questions after arizona crash. *Business news, Reuters*, 2018.

[7] Grant Shapps and Kwasi Kwarteng. *Connected and automated mobility 2025: realising the benefits of self-driving vehicles*. Centre for Connected and Autonomous Vehicles, 2022.

[8] The uk connected and automated mobility roadmap to 2035. *https://zenzic.io/insights/roadmap/[Online]*, 2024. Zenzic.

[9] Liangkai Liu, Sidi Lu, Ren Zhong, Baofu Wu, Yongtao Yao, Qingyang Zhang, and Weisong Shi. Computing systems for autonomous driving: State of the art and challenges. *IEEE Internet of Things Journal*, 8(8):6469–6486, 2020.

[10] Yang Zheng, Shengbo Eben Li, Keqiang Li, Francesco Borrelli, and J Karl Hedrick. Distributed model predictive control for heterogeneous vehicle platoons under unidirectional topologies. *IEEE Transactions on Control Systems Technology*, 25(3):899–910, 2016.

[11] Steven E Shladover, Charles A Desoer, J Karl Hedrick, Masayoshi Tomizuka, Jean Walrand, W-B Zhang, Donn H McMahon, Huei Peng, Shahab Sheikholeslam, and Nick McKeown. Automated vehicle control developments in the path program. *IEEE Transactions on vehicular technology*, 40(1):114–130, 1991.

[12] Jeffrey D Rupp and Anthony G King. Autonomous driving-a practical roadmap. *SAE International*, 2010.

[13] Fabian Kröger. *From Automated to Autonomous Driving: A Transnational Research History on Pioneers, Artifacts and Technological Change (1950-2000)*, volume 70. Springer Nature, 2024.

[14] Zifei Su and Pingen Chen. Cooperative eco-driving controller for battery electric vehicle platooning. *IFAC-PapersOnLine*, 55(37):205–210, 2022.

[15] Chao Yang, Siyu Du, Liang Li, Sixong You, Yiyong Yang, and Yue Zhao. Adaptive real-time optimal energy management strategy based on equivalent factors optimization for plug-in hybrid electric vehicle. *Applied Energy*, 203:883–896, 2017.

[16] Mattias Hovgard, Oscar Jonsson, Nikolce Murgovski, Martin Sanfridson, and Jonas Fredriksson. Cooperative energy management of electrified vehicles on hilly roads. *Control Engineering Practice*, 73:66–78, 2018.

[17] Ziqi Ye, Kailai Li, Michael Stapelbroek, Rene Savelsberg, Marco Günther, and Stefan Pischinger. Variable step-size discrete dynamic programming for vehicle speed trajectory optimization. *IEEE Transactions on Intelligent Transportation Systems*, 20(2):476–484, 2018.

[18] Jinghua Guo, Jingyao Wang, Qing Xu, Ban Wang, and Keqiang Li. Deep reinforcement learning-based hierarchical energy control strategy of a platoon of connected hybrid electric vehicles through cloud platform. *IEEE Transactions on Transportation Electrification*, 2023.

[19] Meng Li, Zehong Cao, and Zhibin Li. A reinforcement learning-based vehicle platoon control strategy for reducing energy consumption in traffic oscillations. *IEEE Transactions on Neural Networks and Learning Systems*, 32(12):5309–5322, 2021.

[20] Mengcheng Tang, Weichao Zhuang, Bingbing Li, Haoji Liu, Ziyou Song, and Guodong Yin. Energy-optimal routing for electric vehicles using deep reinforcement learning with transformer. *Applied Energy*, 350:121711, 2023.

[21] Hailong Zhang, Jiankun Peng, Hanxuan Dong, Fan Ding, and Huachun Tan. Integrated velocity optimization and energy management strategy for hybrid electric vehicle platoon: A multi-agent reinforcement learning approach. *IEEE Transactions on Transportation Electrification*, 2023.

[22] Xi Luo, Zhenghao Xu, Jinlong Hong, Jia Hu, Bingzhao Gao, and Hong Chen. Eco-driving for truck platoon velocity planning based on v2x communication considering road geometry. *IFAC-PapersOnLine*, 56(2):4971–4977, 2023.

[23] Kaijiang Yu, Haizhu Yang, Xingguo Tan, Taketoshi Kawabe, Yanan Guo, Qing Liang, Ziyi Fu, and Zheng Zheng. Model predictive control for hybrid electric vehicle platooning using slope information. *IEEE Transactions on Intelligent Transportation Systems*, 17(7):1894–1909, 2016.

[24] Dawei Pi, Pengyu Xue, Boyuan Xie, Hongliang Wang, Xiaolin Tang, and Xiaosong Hu. A platoon control method based on dmpc for connected energy-

saving electric vehicles. *IEEE Transactions on Transportation Electrification*, 8(3):3219–3235, 2022.

[25] Chunjie Zhai, Chuqiao Chen, Xinlei Zheng, Zhimin Han, Yuhan Gao, Chenggang Yan, Fei Luo, and Jianmin Xu. Ecological cooperative adaptive cruise control for heterogenous vehicle platoons subject to time delays and input saturations. *IEEE Transactions on Intelligent Transportation Systems*, 24(3):2862–2873, 2022.

[26] Sebastian Van De Hoef, Karl Henrik Johansson, and Dimos V Dimarogonas. Fuel-efficient en route formation of truck platoons. *IEEE Transactions on Intelligent Transportation Systems*, 19(1):102–112, 2017.

[27] Anuradha M Annaswamy, Karl H Johansson, George J Pappas, et al. Control for societal-scale challenges: Road map 2030. *IEEE Control Systems Society*, 2023.

[28] Decarbonising uk transport: technology roadmaps. *https://www.gov.uk/government/publications/decarbonising-uk-transport-technology-roadmaps* [Online], 2021. GOV.UK.

[29] Electric vehicles: What's next vii: Confronting greenflation. *https://www.goldmansachs.com/intelligence/pages/electric-vehicles-whats-next-vii-confronting-greenflation.html* [Online], 2022. GOLDMAN SACHS RESEARCH.

[30] Lloyd Peppard. String stability of relative-motion pid vehicle control systems. *IEEE Transactions on Automatic Control*, 19(5):579–581, 1974.

[31] Tsai-Jiun Ren, Tien-Chi Chen, and Chun-Jung Chen. Motion control for a two-wheeled vehicle using a self-tuning pid controller. *Control engineering practice*, 16(3):365–375, 2008.

[32] Lydie Nouveliere et al. Experimental vehicle longitudinal control using a second order sliding mode technique. *Control Engineering Practice*, 15(8):943–954, 2007.

[33] Jiancheng Chen, Zhibin Shuai, Hui Zhang, and Wanzhong Zhao. Path following control of autonomous four-wheel-independent-drive electric vehicles via second-order sliding mode and nonlinear disturbance observer techniques. *IEEE Transactions on Industrial Electronics*, 68(3):2460–2469, 2020.

[34] Yue-Jiao Gong, Jun Zhang, Ou Liu, Rui-Zhang Huang, Henry Shu-Hung Chung, and Yu-Hui Shi. Optimizing the vehicle routing problem with time windows: A discrete particle swarm optimization approach. *IEEE Transactions on Systems, Man, and Cybernetics, Part C (Applications and Reviews)*, 42(2):254–267, 2011.

[35] Zeyu Chen, Rui Xiong, Xue Cai, Zhen Wang, and Ruixin Yang. Regenerative braking control strategy for distributed drive electric vehicles based on slope and mass co-estimation. *IEEE Transactions on Intelligent Transportation Systems*, 2023.

[36] Yougang Bian, Changkun Du, Manjiang Hu, Shengbo Eben Li, Haikuo Liu, and Chongkang Li. Fuel economy optimization for platooning vehicle swarms via distributed economic model predictive control. *IEEE Transactions on Automation Science and Engineering*, 19(4):2711–2723, 2021.

[37] Manjiang Hu, Chongkang Li, Yougang Bian, Hui Zhang, Zhaobo Qin, and Biao Xu. Fuel economy-oriented vehicle platoon control using economic model predictive control. *IEEE Transactions on Intelligent Transportation Systems*, 23(11):20836–20849, 2022.

[38] Saleh Albeaik, Alexandre Bayen, Maria Teresa Chiri, Xiaoqian Gong, Amaury Hayat, Nicolas Kardous, Alexander Keimer, Sean T McQuade, Benedetto Piccoli, and Yiling You. Limitations and improvements of the in-

telligent driver model (idm). *SIAM Journal on Applied Dynamical Systems*, 21(3):1862–1892, 2022.

[39] Mofan Zhou, Xiaobo Qu, and Sheng Jin. On the impact of cooperative autonomous vehicles in improving freeway merging: a modified intelligent driver model-based approach. *IEEE Transactions on Intelligent Transportation Systems*, 18(6):1422–1428, 2016.

[40] Anil Alan, Andrew J Taylor, Chaozhe R He, Aaron D Ames, and Gábor Orosz. Control barrier functions and input-to-state safety with application to automated vehicles. *IEEE Transactions on Control Systems Technology*, 31(6):2744–2759, 2023.

[41] Mo Chen, Jennifer C Shih, and Claire J Tomlin. Multi-vehicle collision avoidance via hamilton-jacobi reachability and mixed integer programming. In *2016 IEEE 55th Conference on Decision and Control (CDC)*, pages 1695–1700. IEEE, 2016.

[42] Matheus Koengkan, José Alberto Fuinhas, Matheus Belucio, Nooshin Karimi Alavijeh, Nasrin Salehnia, Daniel Machado, Vinícius Silva, and Fatemeh Dehdar. The impact of battery-electric vehicles on energy consumption: A macroeconomic evidence from 29 european countries. *World Electric Vehicle Journal*, 13(2):36, 2022.

[43] Kenan Zhang and Yu Marco Nie. Mitigating traffic congestion induced by transportation network companies: A policy analysis. *Transportation Research Part A: Policy and Practice*, 159:96–118, 2022.

[44] David Q Mayne, James B Rawlings, Christopher V Rao, and Pierre OM Scokaert. Constrained model predictive control: Stability and optimality. *Automatica*, 36(6):789–814, 2000.

[45] Alberto Bemporad, Manfred Morari, Vivek Dua, and Efstratios N Pistikopoulos. The explicit linear quadratic regulator for constrained systems. *Automatica*, 38(1):3–20, 2002.

[46] David Q Mayne, María M Seron, and Saša V Raković. Robust model predictive control of constrained linear systems with bounded disturbances. *Automatica*, 41(2):219–224, 2005.

[47] Paul J Goulart, Eric C Kerrigan, and Jan M Maciejowski. Optimization over state feedback policies for robust control with constraints. *Automatica*, 42(4):523–533, 2006.

[48] Mark Brackstone and Mike McDonald. Car-following: a historical review. *Transportation Research Part F: Traffic Psychology and Behaviour*, 2(4):181–196, 1999.

[49] Carl Bergenhem, Steven Shladover, Erik Coelingh, Christoffer Englund, and Sadayuki Tsugawa. Overview of platooning systems. In *Proceedings of the 19th ITS World Congress, Oct 22-26, Vienna, Austria (2012)*, 2012.

[50] Duanfeng Chu, Haoran Li, Chenyang Zhao, and Tuqiang Zhou. Trajectory tracking of autonomous vehicle based on model predictive control with pid feedback. *IEEE Transactions on Intelligent Transportation Systems*, 24(2):2239–2250, 2022.

[51] Steven Parissien. *The Life of the Automobile: A New History of the Motor Car*. Atlantic Books, 2013.

[52] John Heitmann. *The automobile and American life*. McFarland, 2018.

[53] Wolfgang Sachs. *For love of the automobile: Looking back into the history of our desires*. Univ of California Press, 2023.

[54] Heinz Heisler. *Advanced engine technology*. Society of Automotive Engineers, Warrendale, PA (United States), 1995.

[55] Kichiro Kato, Kohei Igarashi, Michihiko Masuda, Katsuji Otsubo, Akio Yasuda, Keiso Takeda, and Toru Sato. Development of engine for natural gas vehicle. *SAE transactions*, pages 939–947, 1999.

[56] Lino Guzzella and Christopher Onder. *Introduction to modeling and control of internal combustion engine systems*. Springer Science & Business Media, 2009.

[57] Timothy Johnson and Ameya Joshi. Review of vehicle engine efficiency and emissions. *SAE International Journal of Engines*, 11(6):1307–1330, 2018.

[58] Ritchie Hannah, Roser Max, and Rosado Pablo. Co2 and greenhouse gas emissions. *Our world in data*, 2020.

[59] Xingyu Liang, Yuesen Wang, Yu Chen, and Sili Deng. Advances in emission regulations and emission control technologies for internal combustion engines. *SAE International Journal of Sustainable Transportation, Energy, Environment, & Policy*, 2(13-02-02-0007):101–119, 2021.

[60] Wei Liu. *Introduction to hybrid vehicle system modeling and control*. John Wiley & Sons, 2013.

[61] Karan C Prajapati, Ravi Patel, and Rachit Sagar. Hybrid vehicle: A study on technology. *Power (kW)*, 2:10–20, 2014.

[62] Damiano Lanzarotto, M Marchesoni, M Passalacqua, A Pini Prato, and M Repetto. Overview of different hybrid vehicle architectures. *IFAC-PapersOnLine*, 51(9):218–222, 2018.

[63] Georgios Fontaras, Panayotis Pistikopoulos, and Zissis Samaras. Experimental evaluation of hybrid vehicle fuel economy and pollutant emissions over real-world simulation driving cycles. *Atmospheric environment*, 42(18):4023–4035, 2008.

[64] Imdat Taymaz and Merthan Benli. Emissions and fuel economy for a hybrid vehicle. *Fuel*, 115:812–817, 2014.

[65] Rajit Johri and Zoran Filipi. Optimal energy management of a series hybrid vehicle with combined fuel economy and low-emission objectives. *Proceed-*

*ings of the Institution of Mechanical Engineers, Part D: Journal of Automobile Engineering*, 228(12):1424–1439, 2014.

[66] Shima Nazari, Jason Siegel, and Anna Stefanopoulou. Optimal energy management for a mild hybrid vehicle with electric and hybrid engine boosting systems. *IEEE Transactions on Vehicular Technology*, 68(4):3386–3399, 2019.

[67] JS Hsu, CW Ayers, CL Coomer, et al. *Report on Toyota/Prius motor design and manufacturing assessment*. United States. Department of Energy, 2004.

[68] Timothy A Burress, Steven L Campbell, Chester Coomer, Curtis William Ayers, Andrew A Wereszczak, Joseph Philip Cunningham, Laura D Marlino, Larry Eugene Seiber, and Hua-Tay Lin. Evaluation of the 2010 toyota prius hybrid synergy drive system. Technical report, Oak Ridge National Lab.(ORNL), Oak Ridge, TN (United States). Power . . . , 2011.

[69] Ning Ding, Krishnamachar Prasad, and Tek Tjing Lie. The electric vehicle: a review. *International Journal of Electric and Hybrid Vehicles*, 9(1):49–66, 2017.

[70] Shrey Verma, Gaurav Dwivedi, and Puneet Verma. Life cycle assessment of electric vehicles in comparison to combustion engine vehicles: A review. *Materials Today: Proceedings*, 49:217–222, 2022.

[71] Shantanu Ingle and Madhuri Phute. Tesla autopilot: semi autonomous driving, an uptick for future autonomy. *International Research Journal of Engineering and Technology*, 3(9):369–372, 2016.

[72] Zoe Long, Jonn Axsen, Inger Miller, and Christine Kormos. What does tesla mean to car buyers? exploring the role of automotive brand in perceptions of battery electric vehicles. *Transportation research part A: Policy and Practice*, 129:185–204, 2019.

[73] Satoshi Murata. Innovation by in-wheel-motor drive unit. *Vehicle System Dynamics*, 50(6):807–830, 2012.

[74] Yutao Luo and Di Tan. Study on the dynamics of the in-wheel motor system. *IEEE transactions on vehicular technology*, 61(8):3510–3518, 2012.

[75] Kazim Cakir and A Sabanovic. In-wheel motor design for electric vehicles. In *9th IEEE International Workshop on Advanced Motion Control, 2006.*, pages 613–618. IEEE, 2006.

[76] Ying Fan, Li Zhang, Jin Huang, and Xuedong Han. Design, analysis, and sensorless control of a self-decelerating permanent-magnet in-wheel motor. *IEEE transactions on industrial electronics*, 61(10):5788–5797, 2014.

[77] Jia-Sheng Hu, Yafei Wang, Hiroshi Fujimoto, and Yoichi Hori. Robust yaw stability control for in-wheel motor electric vehicles. *IEEE/ASME Transactions On Mechatronics*, 22(3):1360–1370, 2017.

[78] Ze Zhao, Hamid Taghavifar, Haiping Du, Yechen Qin, Mingming Dong, and Liang Gu. In-wheel motor vibration control for distributed-driven electric vehicles: A review. *IEEE Transactions on Transportation Electrification*, 7(4):2864–2880, 2021.

[79] M Hadi Amini, Amin Kargarian, and Orkun Karabasoglu. Arima-based decoupled time series forecasting of electric vehicle charging demand for stochastic power system operation. *Electric Power Systems Research*, 140:378–390, 2016.

[80] Jinquan Guo, Hongwen He, and Chao Sun. Arima-based road gradient and vehicle velocity prediction for hybrid electric vehicle energy management. *IEEE Transactions on Vehicular Technology*, 68(6):5309–5320, 2019.

[81] Bingnan Jiang and Yunsi Fei. Vehicle speed prediction by two-level data driven models in vehicular networks. *IEEE Transactions on Intelligent Transportation Systems*, 18(7):1793–1801, 2016.

[82] Jaewook Shin and Myoungho Sunwoo. Vehicle speed prediction using a markov chain with speed constraints. *IEEE Transactions on Intelligent Transportation Systems*, 20(9):3201–3211, 2018.

[83] Chao Sun, Xiaosong Hu, Scott J Moura, and Fengchun Sun. Velocity predictors for predictive energy management in hybrid electric vehicles. *IEEE Transactions on Control Systems Technology*, 23(3):1197–1204, 2014.

[84] Fei Ye, Peng Hao, Xuewei Qi, Guoyuan Wu, Kanok Boriboonsomsin, and Matthew J Barth. Prediction-based eco-approach and departure at signalized intersections with speed forecasting on preceding vehicles. *IEEE Transactions on Intelligent Transportation Systems*, 20(4):1378–1389, 2018.

[85] Chao Sun, Fengchun Sun, and Hongwen He. Investigating adaptive-ecms with velocity forecast ability for hybrid electric vehicles. *Applied energy*, 185:1644–1653, 2017.

[86] Jichao Liu, Yangzhou Chen, Jingyuan Zhan, and Fei Shang. An on-line energy management strategy based on trip condition prediction for commuter plug-in hybrid electric vehicles. *IEEE Transactions on Vehicular Technology*, 67(5):3767–3781, 2018.

[87] Xinyou Lin, Zhaorui Wang, and Jiayun Wu. Energy management strategy based on velocity prediction using back propagation neural network for a plug-in fuel cell electric vehicle. *International Journal of Energy Research*, 45(2):2629–2643, 2021.

[88] Mei Yan, Menglin Li, Hongwen He, and Jiankun Peng. Deep learning for vehicle speed prediction. *Energy Procedia*, 152:618–623, 2018.

[89] Zheyuan Cheng, Mo-Yuen Chow, Daebong Jung, and Jinyong Jeon. A big data based deep learning approach for vehicle speed prediction. In *2017 IEEE 26th International Symposium on Industrial Electronics (ISIE)*, pages 389–394. IEEE, 2017.

[90] Zhendong Zhang, Hongwen He, Jinquan Guo, and Ruoyan Han. Velocity prediction and profile optimization based real-time energy management strategy for plug-in hybrid electric buses. *Applied Energy*, 280:116001, 2020.

[91] Shaojian Han, Fengqi Zhang, Junqiang Xi, Yanfei Ren, and Shaohang Xu. Short-term vehicle speed prediction based on convolutional bidirectional lstm networks. In *2019 IEEE intelligent transportation systems conference (ITSC)*, pages 4055–4060. IEEE, 2019.

[92] Chao Sun, Jianghao Leng, and Fengchun Sun. A fast optimal speed planning system in arterial roads for intelligent and connected vehicles. *IEEE Internet of Things Journal*, 9(20):20295–20307, 2022.

[93] Bolin Gao, Keke Wan, Qien Chen, Zhou Wang, Rui Li, Yu Jiang, Run Mei, Yinghui Luo, and Keqiang Li. A review and outlook on predictive cruise control of vehicles and typical applications under cloud control system. *Machine Intelligence Research*, 20(5):614–639, 2023.

[94] Cong-Zhi Liu, Liang Li, Xiang Chen, Jia-Wang Yong, Shuo Cheng, and Hong-Lei Dong. An innovative adaptive cruise control method based on mixed $\mathscr{H}_2/\mathscr{H}_\infty$ out-of-sequence measurement observer. *IEEE Transactions on Intelligent Transportation Systems*, 23(6):5602–5614, 2021.

[95] Roman Schmied and Patrizio Colaneri. Mixed $\mathscr{H}_2 - \mathscr{H}_\infty$ control for automated highway driving. *Mechatronics*, 57:63–72, 2019.

[96] Hafiz Muhammad Yasir Naeem, Aamer Iqbal Bhatti, and Ahmad Mahmood. Longitudinal cruise control of a car using sliding mode approach. In *2019 International Conference on Electrical, Communication, and Computer Engineering (ICECCE)*, pages 1–5. IEEE, 2019.

[97] D Ren, J Zhang, and Jiye Zhang. Sliding mode control for vehicle following with parametric uncertainty. *Electr. Mach. Control*, 14(1):73–78, 2010.

[98] Yuanjian Zhang, Yanjun Huang, Zheng Chen, Guang Li, and Yonggang Liu. A novel learning-based model predictive control strategy for plug-in hybrid electric vehicle. *IEEE Transactions on Transportation Electrification*, 8(1):23–35, 2021.

[99] Zhuoran Hou, Liang Chu, Zhiqi Guo, Jincheng Hu, Jingjing Jiang, Jun Yang, Zheng Chen, and Yuanjian Zhang. A learning-and-tube-based robust model predictive control strategy for plug-in hybrid electric vehicle. *IEEE Transactions on Intelligent Vehicles*, 2023.

[100] Hao Sun, Li Dai, and Boli Chen. Tube-based distributed model predictive control for heterogeneous vehicle platoons via convex optimization. In *2022 IEEE 25th International Conference on Intelligent Transportation Systems (ITSC)*, pages 1122–1127. IEEE, 2022.

[101] Yang Liu, Deyin Yao, Lijie Wang, and Shejie Lu. Distributed adaptive fixed-time robust platoon control for fully heterogeneous vehicles. *IEEE Transactions on Systems, Man, and Cybernetics: Systems*, 53(1):264–274, 2022.

[102] Jianshan Zhou, Daxin Tian, Zhengguo Sheng, Xuting Duan, Guixian Qu, Dongpu Cao, and Xuemin Shen. Decentralized robust control for vehicle platooning subject to uncertain disturbances via super-twisting second-order sliding-mode observer technique. *IEEE Transactions on Vehicular Technology*, 71(7):7186–7201, 2022.

[103] Hao Sun, Bingbing Li, Hao Zhang, Li Dai, Giuseppe Fedele, Weichao Zhuang, and Boli Chen. Ecological electric vehicle platooning: An adaptive tube-based distributed model predictive control approach. *IEEE Transactions on Transportation Electrification*, 2024.

[104] Miguel A Vaquero-Serrano and Jesus Felez. A control algorithm for a coordinated stop of a convoy at stations in a virtual coupling system based on a predecessor-leader following communication topology. In *2023 IEEE*

*26th International Conference on Intelligent Transportation Systems (ITSC)*, pages 1152–1157. IEEE, 2023.

[105] William B Dunbar and Derek S Caveney. Distributed receding horizon control of vehicle platoons: Stability and string stability. *IEEE Transactions on Automatic Control*, 57(3):620–633, 2011.

[106] Jianglin Lan, Dezong Zhao, and Daxin Tian. Data-driven robust predictive control for mixed vehicle platoons using noisy measurement. *IEEE Transactions on Intelligent Transportation Systems*, 24(6):6586–6596, 2021.

[107] Jingzheng Guo, Hongyan Guo, Jun Liu, Dongpu Cao, and Hong Chen. Distributed data-driven predictive control for hybrid connected vehicle platoons with guaranteed robustness and string stability. *IEEE Internet of Things Journal*, 9(17):16308–16321, 2022.

[108] Liwei Xu, Xianjian Jin, Yan Wang, Ying Liu, Weichao Zhuang, and Guodong Yin. Stochastic stable control of vehicular platoon time-delay system subject to random switching topologies and disturbances. *IEEE Transactions on Vehicular Technology*, 71(6):5755–5769, 2022.

[109] Hong Wang, Li-Ming Peng, Zichun Wei, Kai Yang, Luo Jiang, Ehsan Hashemi, et al. A holistic robust motion control framework for autonomous platooning. *IEEE Transactions on Vehicular Technology*, 72(12):15213–15226, 2023.

[110] Zhiwen Qiang, Li Dai, Boli Chen, and Yuanqing Xia. Distributed model predictive control for heterogeneous vehicle platoon with inter-vehicular spacing constraints. *IEEE Transactions on Intelligent Transportation Systems*, 24(3):3339–3351, 2022.

[111] Jianglin Lan and Dezong Zhao. Min-max model predictive vehicle platooning with communication delay. *IEEE Transactions on Vehicular Technology*, 69(11):12570–12584, 2020.

[112] Osman Erman Gungor and Imad L Al-Qadi. All for one: Centralized optimization of truck platoons to improve roadway infrastructure sustainability. *Transportation Research Part C: Emerging Technologies*, 114:84–98, 2020.

[113] Pangwei Wang, Hui Deng, Juan Zhang, Li Wang, Mingfang Zhang, and Yongfu Li. Model predictive control for connected vehicle platoon under switching communication topology. *IEEE Transactions on Intelligent Transportation Systems*, 23(7):7817–7830, 2021.

[114] Keqiang Li, Yougang Bian, Shengbo Eben Li, Biao Xu, and Jianqiang Wang. Distributed model predictive control of multi-vehicle systems with switching communication topologies. *Transportation Research Part C: Emerging Technologies*, 118:102717, 2020.

[115] Shuo Feng, Yi Zhang, Shengbo Eben Li, Zhong Cao, Henry X Liu, and Li Li. String stability for vehicular platoon control: Definitions and analysis methods. *Annual Reviews in Control*, 47:81–97, 2019.

[116] Srdjan S Stankovic, Milorad J Stanojevic, and Dragoslav D Siljak. Decentralized overlapping control of a platoon of vehicles. *IEEE Transactions on Control Systems Technology*, 8(5):816–832, 2000.

[117] Shengbo Li, Keqiang Li, Rajesh Rajamani, and Jianqiang Wang. Model predictive multi-objective vehicular adaptive cruise control. *IEEE Transactions on control systems technology*, 19(3):556–566, 2010.

[118] Junyan Hu, Parijat Bhowmick, Farshad Arvin, Alexander Lanzon, and Barry Lennox. Cooperative control of heterogeneous connected vehicle platoons: An adaptive leader-following approach. *IEEE Robotics and Automation Letters*, 5(2):977–984, 2020.

[119] Xinle Gong, Sheng Liang, Bowen Wang, and Wei Zhang. Game theory-based decision-making and iterative predictive lateral control for cooperative obstacle avoidance of guided vehicle platoon. *IEEE Transactions on Vehicular Technology*, 2023.

[120] Yulin Ma, Zhixiong Li, Reza Malekian, Sifa Zheng, and Miguel Angel Sotelo. A novel multimode hybrid control method for cooperative driving of an automated vehicle platoon. *IEEE Internet of Things Journal*, 8(7):5822–5838, 2020.

[121] Jose E Naranjo, Carlos Gonzalez, Ricardo Garcia, and Teresa De Pedro. Lane-change fuzzy control in autonomous vehicles for the overtaking maneuver. *IEEE Transactions on Intelligent Transportation Systems*, 9(3):438–450, 2008.

[122] Marcin Stryszowski, Stefano Longo, Dario D'Alessandro, Efstathios Velenis, Gregory Forostovsky, and Sabato Manfredi. A framework for self-enforced optimal interaction between connected vehicles. *IEEE Transactions on Intelligent Transportation Systems*, 22(10):6152–6161, 2020.

[123] Liwei Xu, Weichao Zhuang, Guodong Yin, Chentong Bian, and Huawei Wu. Modeling and robust control of heterogeneous vehicle platoons on curved roads subject to disturbances and delays. *IEEE Transactions on Vehicular Technology*, 68(12):11551–11564, 2019.

[124] Meng Qiu, Di Liu, Simone Baldi, Guodong Yin, Wenwu Yu, and Ming Cao. Vehicular platooning on curved paths considering collision avoidance and string stability. *IEEE Transactions on Network Science and Engineering*, 2023.

[125] Jingkai Wu, Yafei Wang, and Chengliang Yin. Curvilinear multilane merging and platooning with bounded control in curved road coordinates. *IEEE Transactions on Vehicular Technology*, 71(2):1237–1252, 2021.

[126] Hang Zhao, Dihua Sun, Min Zhao, Qiankun Pu, and Chuancong Tang. Combined longitudinal and lateral control for heterogeneous nodes in mixed vehicle platoon under v2i communication. *IEEE Transactions on Intelligent Transportation Systems*, 23(7):6751–6765, 2021.

[127] Hao Liu, Xiao-Yun Lu, and Steven E Shladover. Traffic signal control by leveraging cooperative adaptive cruise control (cacc) vehicle platooning capabilities. *Transportation research part C: emerging technologies*, 104:390–407, 2019.

[128] Zifei Nie and Hooman Farzaneh. Real-time dynamic predictive cruise control for enhancing eco-driving of electric vehicles, considering traffic constraints and signal phase and timing (spat) information, using artificial-neural-network-based energy consumption model. *Energy*, 241:122888, 2022.

[129] Mingyang Chen, Bingbing Li, Yougang Bian, Weichao Zhuang, Simos A Evangelou, Xiao Pan, and Boli Chen. Intersection signal-vehicle coupled coordination with mixed autonomy vehicles. *IEEE Transactions on Transportation Electrification*, 2024.

[130] Tingting Xiao, Chen Chen, Qingqi Pei, and Houbing Herbert Song. Consortium blockchain-based computation offloading using mobile edge platoon cloud in internet of vehicles. *IEEE Transactions on Intelligent Transportation Systems*, 23(10):17769–17783, 2022.

[131] Junxiao Zhao, Yaling Ma, Li Dai, Zhongqi Sun, and Yuanqing Xia. Cloud-edge cooperative distributed mpc with event-triggered switching strategy for heterogeneous vehicle platoon. *IEEE Transactions on Vehicular Technology*, 2024.

[132] Brian Paden, Michal Čáp, Sze Zheng Yong, Dmitry Yershov, and Emilio Frazzoli. A survey of motion planning and control techniques for self-driving urban vehicles. *IEEE Transactions on intelligent vehicles*, 1(1):33–55, 2016.

[133] Yue Zhou, Michael E Cholette, Ashish Bhaskar, and Edward Chung. Optimal vehicle trajectory planning with control constraints and recursive implementation for automated on-ramp merging. *IEEE Transactions on Intelligent Transportation Systems*, 20(9):3409–3420, 2018.

[134] Songtao Xie, Junyan Hu, Parijat Bhowmick, Zhengtao Ding, and Farshad Arvin. Distributed motion planning for safe autonomous vehicle overtaking via artificial potential field. *IEEE Transactions on Intelligent Transportation Systems*, 23(11):21531–21547, 2022.

[135] Jie Fan, Xudong Zhang, Kun Zheng, Yuan Zou, and Nana Zhou. Hierarchical path planner combining probabilistic roadmap and deep deterministic policy gradient for unmanned ground vehicles with non-holonomic constraints. *Journal of the Franklin Institute*, 361(8):106821, 2024.

[136] Zhi Lin, Kang Wu, Rulin Shen, Xin Yu, and Shiquan Huang. An efficient and accurate a-star algorithm for autonomous vehicle path planning. *IEEE Transactions on Vehicular Technology*, 2023.

[137] Dan-Dan Zhu and Jun-Qing Sun. A new algorithm based on dijkstra for vehicle path planning considering intersection attribute. *IEEE Access*, 9:19761–19775, 2021.

[138] Yonggang Liu, Bobo Zhou, Xiao Wang, Liang Li, Shuo Cheng, Zheng Chen, Guang Li, and Lu Zhang. Dynamic lane-changing trajectory planning for autonomous vehicles based on discrete global trajectory. *IEEE Transactions on Intelligent Transportation Systems*, 23(7):8513–8527, 2021.

[139] Hongcai Li, Wenjie Liu, Chao Yang, Weida Wang, Tianqi Qie, and Changle Xiang. An optimization-based path planning approach for autonomous vehicles using the dynefwa-artificial potential field. *IEEE Transactions on Intelligent Vehicles*, 7(2):263–272, 2021.

[140] Qinglu Ma, Meiqiang Li, GuangHao Huang, and Saleem Ullah. Overtaking path planning for cav based on improved artificial potential field. *IEEE Transactions on Vehicular Technology*, 2023.

[141] Yonghwan Jeong and Kyongsu Yi. Target vehicle motion prediction-based motion planning framework for autonomous driving in uncontrolled intersec-

tions. *IEEE Transactions on Intelligent Transportation Systems*, 22(1):168–177, 2019.

[142] Dae Jung Kim, Yong Woo Jeong, and Chung Choo Chung. Lateral vehicle trajectory planning using a model predictive control scheme for an automated perpendicular parking system. *IEEE Transactions on Industrial Electronics*, 70(2):1820–1829, 2022.

[143] Szilárd Aradi. Survey of deep reinforcement learning for motion planning of autonomous vehicles. *IEEE Transactions on Intelligent Transportation Systems*, 23(2):740–759, 2020.

[144] Xinglong Zhang, Yan Jiang, Yang Lu, and Xin Xu. Receding-horizon reinforcement learning approach for kinodynamic motion planning of autonomous vehicles. *IEEE Transactions on Intelligent Vehicles*, 7(3):556–568, 2022.

[145] Sreenatha G Anavatti, Sobers LX Francis, and Matthew Garratt. Path-planning modules for autonomous vehicles: Current status and challenges. In *2015 International Conference on Advanced Mechatronics, Intelligent Manufacture, and Industrial Automation (ICAMIMIA)*, pages 205–214. IEEE, 2015.

[146] Bai Li, Hong Liu, Duo Xiao, Guizhen Yu, and Youmin Zhang. Centralized and optimal motion planning for large-scale agv systems: A generic approach. *Advances in Engineering Software*, 106:33–46, 2017.

[147] Christopher M Clark. Probabilistic road map sampling strategies for multi-robot motion planning. *Robotics and Autonomous Systems*, 53(3-4):244–264, 2005.

[148] Henrik Andreasson, Abdelbaki Bouguerra, Marcello Cirillo, Dimitar Nikolaev Dimitrov, Dimiter Driankov, Lars Karlsson, Achim J Lilienthal, Federico Pecora, Jari Pekka Saarinen, Aleksander Sherikov, et al. Autonomous

transport vehicles: Where we are and what is missing. *IEEE Robotics & Automation Magazine*, 22(1):64–75, 2015.

[149] Alon Tuchner and Jack Haddad. Vehicle platoon formation using interpolating control: A laboratory experimental analysis. *Transportation Research Part C: Emerging Technologies*, 84:21–47, 2017.

[150] Yongfu Li, Wenbo Chen, Srinivas Peeta, and Yibing Wang. Platoon control of connected multi-vehicle systems under v2x communications: Design and experiments. *IEEE Transactions on Intelligent Transportation Systems*, 21(5):1891–1902, 2019.

[151] Alexander Schwab, Lisa-Marie Reichelt, Philipp Welz, and Jan Lunze. Experimental evaluation of an adaptive cruise control and cooperative merging concept. In *2020 IEEE Conference on Control Technology and Applications (CCTA)*, pages 318–325. IEEE, 2020.

[152] América Morales and Henk Nijmeijer. Merging strategy for vehicles by applying cooperative tracking control. *IEEE Transactions on Intelligent Transportation Systems*, 17(12):3423–3433, 2016.

[153] Qinqin Sun, Xiuye Wang, Guolai Yang, Ye-Hwa Chen, and Fai Ma. Adaptive robust formation control of connected and autonomous vehicle swarm system based on constraint following. *IEEE transactions on cybernetics*, 2022.

[154] Zichao Huang, Duanfeng Chu, Chaozhong Wu, and Yi He. Path planning and cooperative control for automated vehicle platoon using hybrid automata. *IEEE Transactions on Intelligent Transportation Systems*, 20(3):959–974, 2018.

[155] Antonio Bono, Giuseppe Fedele, and Giuseppe Franze. A swarm-based distributed model predictive control scheme for autonomous vehicle formations in uncertain environments. *IEEE Transactions on Cybernetics*, 52(9):8876–8886, 2021.

[156] Hongjiu Yang, Yongqi He, Yang Xu, and Hai Zhao. Collision avoidance for autonomous vehicles based on mpc with adaptive apf. *IEEE Transactions on Intelligent Vehicles*, 2023.

[157] Shiyu Zhao, Dimos V Dimarogonas, Zhiyong Sun, and Dario Bauso. A general approach to coordination control of mobile agents with motion constraints. *IEEE Transactions on Automatic Control*, 63(5):1509–1516, 2017.

[158] Shiyu Zhao and Zhiyong Sun. Defend the practicality of single-integrator models in multi-robot coordination control. In *2017 13th IEEE International Conference on Control & Automation (ICCA)*, pages 666–671. IEEE, 2017.

[159] David Q Mayne, Saša V Raković, Rolf Findeisen, and Frank Allgöwer. Robust output feedback model predictive control of constrained linear systems. *Automatica*, 42(7):1217–1222, 2006.

[160] Joan Bruna, Wojciech Zaremba, Arthur Szlam, and Yann LeCun. Spectral networks and locally connected networks on graphs. *arXiv preprint arXiv:1312.6203*, 2013.

[161] Mingxing Xu, Wenrui Dai, Chunmiao Liu, Xing Gao, Weiyao Lin, Guo-Jun Qi, and Hongkai Xiong. Spatial-temporal transformer networks for traffic flow forecasting. *arXiv preprint arXiv:2001.02908*, 2020.

[162] Sepp Hochreiter and Jürgen Schmidhuber. Long short-term memory. *Neural computation*, 9(8):1735–1780, 1997.

[163] Kyunghyun Cho, Bart Van Merriënboer, Caglar Gulcehre, Dzmitry Bahdanau, Fethi Bougares, Holger Schwenk, and Yoshua Bengio. Learning phrase representations using rnn encoder-decoder for statistical machine translation. *arXiv preprint arXiv:1406.1078*, 2014.

[164] Bing Yu, Haoteng Yin, and Zhanxing Zhu. Spatio-temporal graph convolutional networks: A deep learning framework for traffic forecasting. *arXiv preprint arXiv:1709.04875*, 2017.

[165] Didier Rodrigues Lopes and Simos A Evangelou. Energy savings from an eco-cooperative adaptive cruise control: a bev platoon investigation. In *2019 18th European Control Conference (ECC)*, pages 4160–4167. IEEE, 2019.

[166] Sheng Yu, Xiao Pan, Anastasis Georgiou, Boli Chen, Imad M Jaimoukha, and Simos A Evangelou. A real-time robust ecological-adaptive cruise control strategy for battery electric vehicles. *IEEE Transactions on Transportation Electrification*, 2023.

[167] Bingbing Li, Weichao Zhuang, Mengcheng Tang, and Jinhui Li. Hierarchical optimal control of a group of electric vehicles for maximizing energy efficiency and battery life. In *2022 6th CAA International Conference on Vehicular Control and Intelligence (CVCI)*, pages 1–6. IEEE, 2022.

[168] Martin Treiber, Ansgar Hennecke, and Dirk Helbing. Congested traffic states in empirical observations and microscopic simulations. *Physical review E*, 62(2):1805, 2000.

[169] Ksander N de Winkel, Tugrul Irmak, Riender Happee, and Barys Shyrokau. Standards for passenger comfort in automated vehicles: Acceleration and jerk. *Applied Ergonomics*, 106:103881, 2023.

[170] Bingbing Li, Weichao Zhuang, Hao Zhang, Hao Sun, Haoji Liu, Jianrun Zhang, Guodong Yin, and Boli Chen. Traffic-aware ecological cruising control for connected electric vehicle. *IEEE Transactions on Transportation Electrification*, 2023.

[171] Qianyue Luo, Anh-Tu Nguyen, James Fleming, and Hui Zhang. Unknown input observer based approach for distributed tube-based model predictive control of heterogeneous vehicle platoons. *IEEE Transactions on Vehicular Technology*, 70(4):2930–2944, 2021.

[172] Jan Lunze. Adaptive cruise control with guaranteed collision avoidance. *IEEE Transactions on Intelligent Transportation Systems*, 20(5):1897–1907, 2018.

[173] Iasson Karafyllis, Dionysios Theodosis, and Markos Papageorgiou. Nonlinear adaptive cruise control of vehicular platoons. *International Journal of Control*, 96(1):147–169, 2023.

[174] Withawin Vilaivannaporn, Suthida Boonsith, Warangkana Pornputtapitak, and Pornchai Bumroongsri. Robust output feedback predictive controller with adaptive invariant tubes and observer gains. *International Journal of Dynamics and Control*, 9:755–765, 2021.

[175] Marcello Farina and Riccardo Scattolini. Distributed predictive control: A non-cooperative algorithm with neighbor-to-neighbor communication for linear systems. *Automatica*, 48(6):1088–1096, 2012.

[176] Yang Zheng, Shengbo Eben Li, Jianqiang Wang, Dongpu Cao, and Keqiang Li. Stability and scalability of homogeneous vehicular platoon: Study on the influence of information flow topologies. *IEEE Transactions on intelligent transportation systems*, 17(1):14–26, 2015.

[177] Johan Lofberg. Yalmip: A toolbox for modeling and optimization in matlab. In *2004 IEEE international conference on robotics and automation (IEEE Cat. No. 04CH37508)*, pages 284–289. IEEE, 2004.

[178] Mosek Aps. The mosek optimization toolbox for matlab manual. version 9.0., 2019.

[179] Junseok Boo and Dongkyoung Chwa. Integral sliding mode control-based robust bidirectional platoon control of vehicles with the unknown acceleration and mismatched disturbance. *IEEE Transactions on Intelligent Transportation Systems*, 2023.

[180] Chaoyong Zhang, Duanfeng Chu, Shidong Liu, Zejian Deng, Chaozhong Wu, and Xiaocong Su. Trajectory planning and tracking for autonomous vehicle based on state lattice and model predictive control. *IEEE Intelligent Transportation systems magazine*, 11(2):29–40, 2019.

[181] Jason Kong, Mark Pfeiffer, Georg Schildbach, and Francesco Borrelli. Kinematic and dynamic vehicle models for autonomous driving control design. In *2015 IEEE intelligent vehicles symposium (IV)*, pages 1094–1099. IEEE, 2015.

[182] Dibyendu Roy, Arijit Chowdhury, Madhubanti Maitra, and Samar Bhattacharya. Geometric region-based swarm robotics path planning in an unknown occluded environment. *IEEE Transactions on Industrial Electronics*, 68(7):6053–6063, 2020.

[183] Jérôme Barraquand and J-C Latombe. A monte-carlo algorithm for path planning with many degrees of freedom. In *Proceedings., IEEE International Conference on Robotics and Automation*, pages 1712–1717. IEEE, 1990.

[184] Adrian Wiltz, Fei Chen, and Dimos V Dimarogonas. A consistency constraint-based approach to coupled state constraints in distributed model predictive control. In *2022 IEEE 61st Conference on Decision and Control (CDC)*, pages 3959–3964. IEEE, 2022.

[185] Adrian Wiltz, Fei Chen, and Dimos V Dimarogonas. Parallelized robust distributed model predictive control in the presence of coupled state constraints. *arXiv preprint arXiv:2112.05965*, 2021.

[186] Giuseppe Franzè, Giuseppe Fedele, Antonio Bono, and Luigi D'Alfonso. Reference tracking for multiagent systems using model predictive control. *IEEE Transactions on Control Systems Technology*, 31(4):1884–1891, 2022.